On surface spin detection and doping of metallocenes

Nicolas Bachellier

To cite this version:

Nicolas Bachellier. On surface spin detection and doping of metallocenes. Physics [physics]. Université de Strasbourg, 2016. English. NNT : 2016STRAE030 . tel-01527663

HAL Id: tel-01527663
https://theses.hal.science/tel-01527663v1

Submitted on 24 May 2017

UNIVERSITÉ DE STRASBOURG

ÉCOLE DOCTORALE Physique Chimie-Physique (ED 182)

Institut de Physique et Chimie des Matériaux de Strasbourg

THÈSE présentée par :

Nicolas Bachellier

soutenue le : **13 Décembre 2016**

pour obtenir le grade de : **Docteur de l'université de Strasbourg**
Discipline/ Spécialité : Physique

On surface spin detection and doping of metallocenes

THÈSE dirigée par :

M. LIMOT Laurent	Chargé de recherche, CNRS (IPCMS), Strasbourg

RAPPORTEURS :

M. CREN Tristan	Chargé de recherche, CNRS (INSP), Paris
M. JELINEK Pavel	Professor, Institute of Physics of the Czech Academy of Science

---

AUTRES MEMBRES DU JURY :

Mme BOCQUET Marie-Laure	Directrice de recherche, CNRS (ENS-Paris), Paris
M. SIMON Laurent	Directeur de recherche, CNRS (IS2M), Mulhouse
M. BOWEN Martin	Chargé de recherche, CNRS (IPCMS), Strasbourg

Acknowledgements

I spent more than 3 years as a PhD student in IPCMs, and met exceptionnal people without whom my Phd time would have been much less interesting.

First, I would like to thank my PhD advisor, Laurent Limot, for welcoming me in his team as a PhD student and for the time he invested in the lab to show us how to properly run an STM and the hours we spent to repair and upgrade the STM to make the measurements possible. I also thank him for all his teaching concerning science and the world of research.

The second member of the team is Maider Ormaza (great fan of cookies and chocolate, especially those in my drawers), who entered the group as a post-doc researcher at the same time as me. You showed me many things about experimental works, particularly that we have to check everything at least twice. The last member of the team, who joined us later as a second PhD student is Benjamin Verlhac. I want to thank you for the nice time we spent working in the lab, drinking coffee, and for the fruitful discussion about video games we had!

Our team couldn't have been so successfull without the help of people from the DSI department. The first of them is Fabrice Schreurer, you are literally a reference for surface science. You helped us in many ways, to deal with measurement interpretation and experiment design, to understand phenomena at works on our samples and brought us to Soleil to experimentally confirm our hypothesis about molecules. By the way, there is a legend telling that one night in Deimos beamline at 3 am, we had an exciting mouse hunting session...

Virginie Speisser, you (can be terrifying when you want to and) provided a priceless support, particularly when we had troubles with pumps, broken filaments or any questions linked to administrative papers. I hope you will continue to take care of the new PhD students as you did for me, because I learnt many useful tips thanks to you.

The other half of the STM group of IPCMS is the team of Guillaume Schull, Michael Chong (we still owe a pizza to each other!), Gael Reecht and Benjamin Doppagne. Even if I didn't closely worked with you, yu offered help many times for cryogenics transfer or when our machine didn't work as expected.

I would like to thank Bernard Muller and Jean-George Faullumel for the amazing work you did for us in the workshop, designing and creating new elements for the STM and repairing the broken parts in no time. Also Emmanuel Stersinsky for your help concerning the electronics of our pumps and the electromagnetic shielding of the experiment.

We spent few weeks in Soleil synchrotron. I thank the DEIMOS beamline staff, especially Phillipe Ohresser who welcomed us, Loic Joly and Michelangelo Romeo who with I spent days and nights acquiring and analysisng XMCD spectra.

I also want to thank again our coworkers, the team of Marie-Laure Bocquet, including Martin Vérot, Tangui Le Bahers and Marisa Faraggi for the impressive work of simulation they did about our molecular layers and their customization. The second group of coworkers was lead by Nicolas Lorente and includes Roberto Robles and Paula Abufager. Meetings we regularly organized were stimulating and interesting moments. And all of you did an amazing job and strongly contributed to the understanding of our measurements.

I want to thank all the jury members who came to review and comment my works : Marie-Laure Bocquet, Tristan Cren, Pavel Jelinek, Laurent Simon et Martin Bowen. I appreciated your useful comments and evaluations.

I thank all members of the "place du café" group : Kerstin, Michael, Dominik and Marie-Astrid, Tindara and Simon, Silvia, Gael, Manu, Celine and Thierry, Peter, Ondrej, Guillaume F., Florian, Dimitra, Tsiky, Olivia, Etienne, Guillaume C., and Francois for the coffee breaks we shared, the and the thrilling rounds of tarot card game that i cannot forget. And I also thank the brave people who came with me to discover the hiking paths in the Vosges mountains : Nasima, Majid, Viktoriia, Yooleemi and Selvi. I hope you enjoyed it as much as me! And finally the ADEPPT association for the parties organized such as bowling or laser tags events and the famous pétanque contest at the end of the year.

I also met really nice people outside of the lab, first in the Aikido club of Illkirch : Michel, Cecilia, Quentin, Gilles, Attila, Olivier, Yohan, Marc, Marcel and all the people I practised with on the tatami. And in a second time in the ASCPA climbing section : Claire, Théo "Tarte aux Pommes", Jérôme, Maud, Christophe, Rémy, Alex and everybody I met at the bottom (or the top!) of the cliffs of Alsace.

At last but not least, I really want to thank my familly, especially my parents. You supported me along those years despite the distance and enabled me to finish my PhD in the best possible conditions.

Table of contents

List of figures

List of tables

Abstract

0.1 Introduction : Contexte de l’étude (Chapitre 1)

Mes travaux de thèse portent sur l’étude par microscopie à effet tunnel des propriétés d’atomes et molecules uniques adsorbés à la surface de crystaux métalliques. Le cadre général de cette étude s’inscrit dans le domaine de la spintronique. Les résultats de transport d’électrons à travers des multicouches de matériaux ferromagnétiques [1] ont montré que la direction d’aimantation relative entre deux couches magnétiques a un grande influence sur la resistivité du système. La découverte de ce phénomène, appelé magnéto-résistance géante (GMR), fut récompensée par un prix nobel en 2007 pour les avancées qu’elle a permis dans le domaine des nanotechnologies.

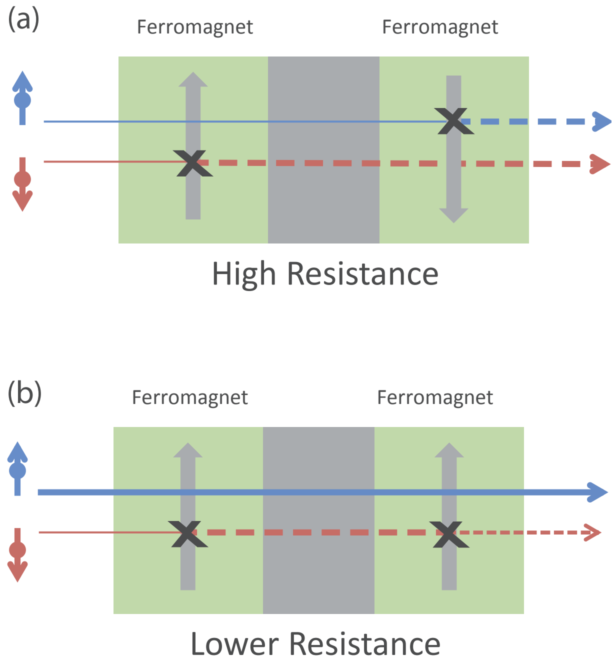

Figure 1: **Courant à travers des couches magnétiques.** (a) Cas de deux couches orientées de manière anti-parallèle. (b) Cas de deux couches orientées de manière parallèle.

Le système de base pour la spintronique (Fig. 1) se compose de 3 couches dont deux magnétiques découplé par une troisième couche. Dans le cas où les deux aimantations ne sont pas orientées dans la même direction, les deux orientations possibles de spin, nommées "up" et "down" vont être pénalisées lors de la traversée d'un matériaux ayant une orientation magnetique opposé à l'orientation du spin considérée (Fig. 1a. Il en résulte un forte résistivité du système. Dans le cas de la GMR, l'application d'un champ magnétique suffisament intense va permettre d'aligner les aimantations des deux aimants (Fig. 1b). Ceci a pour conséquence de favoriser le passages des électrons ayant un spin parallèle à l'aimantation des deux aimants, diminuant ainsi la résistance générale du système.

Mais la propriété qui nous intéresse ici est la polarization magnétique du courant traversant notre système. En effet, le courant traversant le système considéré est majoritairment composé d'électrons ayant un spin orienté parralèlement au moments magnétiques des aimants. Il est alors possible de définir une polarisation en spin du courant notée P comme suit:

$$P = \frac{I_{up} - I_{down}}{I_{up} + I_{down}} \tag{1}$$

L'objectif principal consiste maintenant à créer des dispositifs ayant une polarisation en spin aussi grande que possible.

Pour cela, l'emploi de de molécules organiques au sein des systèmes apparait comme une solution prometteuse. En effet, le faible couplage spin-orbite permet d'obtenir une longueur de diffusion de spin importante. De plus, l'emploi de molécules organique permet de bénéficier de toutes les possibilités offertes par l'ingéniérie moléculaire en matière de fonctionnalisation de molécule. Enfin, l'adsorption de molécules à la surface d'électrodes métalliques peut conduire la modification locale des densités d'état (Fig. 2), ayant une influence directe sur la polarisation du courant passant à travers le système.

0.1.1 Métallocènes

Les molécules à l'étude ici appartiennent à la famille des métallocènes. Elles sont composé d'un atome appartenant aux métaux de transition cerné par deux ligands cyclopentadiényles C_5H_5 notés ici Cp (Fig. 1.6), pour un total de 21 atomes, ce qui en fait une molécule relativement petite et compact par rapport aux autres entitées étudiées comme les phtalocyanines ou les porphyrines. L'attrait principal des métallocènes est l'impact direct de la nature de l'atome métallique sur les propriétées magnétiques de la molécule. Ainsi, le ferrocène est une molecule non magnétique dans son ensemble tandis que le cobaltocène dispose d'un moment magnétique de spin total de 1/2 et le nickelocène dispose d'un spin 1.

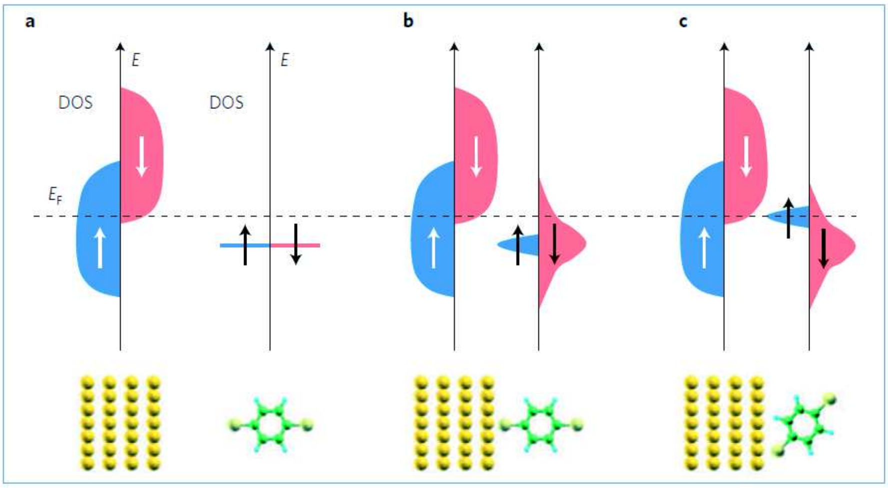

Figure 2: **Influence de l’adsorption sur la DOS d’une molécule** (a) Différentes densités d’états pour des systèmes séparés. (b) Première géometrie d’adsorption d’une molécule et densités d’état résultantes. (c) Seconde géométrie d’adsorption possible et changement dans les densités d’états.

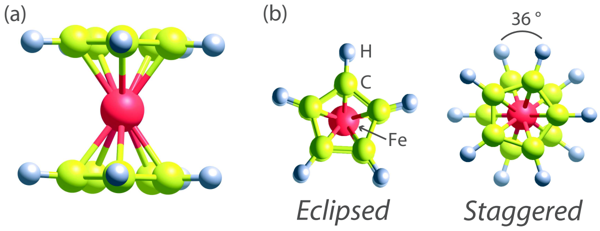

Figure 3: **Structure des métallocènes.**

Les propriétes de transport de spin de ces molécules on été étudiées de manière théoriques et prédictives dans les années 2000. Il est apparu qu’un fil moléculaire composé de metallocènes séparées par des atomes de metal de transition pourrait donner lieu à une polarisation en spin de son facteur de transmission d’electron. Les calculs présentés par Wang et co-auteurs [2] suggèrent qu’une polarisation de l’ordre de 90% serait possible pour deux molécules de vanadocènes (VCp_2) séparées par un troisième atome de vanadium et contactées par deux electrodes en or. De plus, si les vanadocènes sont remplacés par des ferrocènes, la polarisation est inversée favorisant maintenant la population de spin qui auparavant était minoritaire. Ceci montre que la nature du métalocène employé a une grande influence sur le comportement du fil moléculaire théorique. D’autres résultats montrent que la longueur de la chaine ainsi que l’entité chimique contactant l’électrode métallique (Cp ou atome métallique).

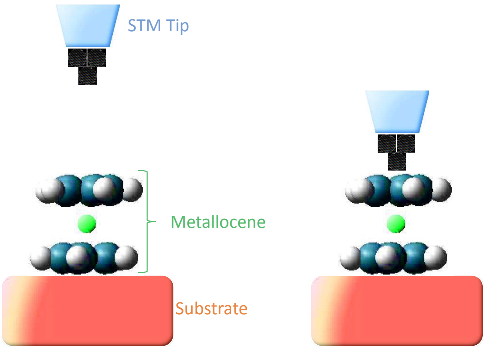

Figure 4: **Schéma de l'étude de métallocènes par STM.** A gauche, cas d'une étude en régime tunnel et à droite, cas d'un contact entre la pointe STM et une molécule.

Les études théoriques ont montré que les métallocènes peuvent être d'interessants systèmes pour concevoir des filtres de spin à l'échelle de la molécule unique. Cependant, la réalisation et l'étude expérimentale de tels systèmes n'a pour le moment pas encore donné de résutlats probants. Notre équipe a choisie d'étudier ces molécules à l'aide d'un microscope à effet tunnel (STM).

0.2 principe STM (Chapitre 2)

0.2.1 Courant tunnel

Le microscope à effet tunnel (STM) s'appuie sur la dualité onde-corpuscule des électrons pour faire passer un faible courant électrique entre deux electrodes espacées de quelques nanomètres seulement. En utilisant l'approximation de Wentzel-Kramers-Brillouin, le courant passant entre la pointe et l'échantillon peut être exprimé par :

$$I(z,V) \propto \int_{-\infty}^{\infty} T(z,E,V)[f(E-V)-f(E)]\rho_t(E-V)\rho_s(E)dE, \tag{2}$$

où

$$T(E,z,V) \propto exp[-kz\sqrt{\phi_{eff}+\frac{V}{2}-(E-E_{\|})}], \tag{3}$$

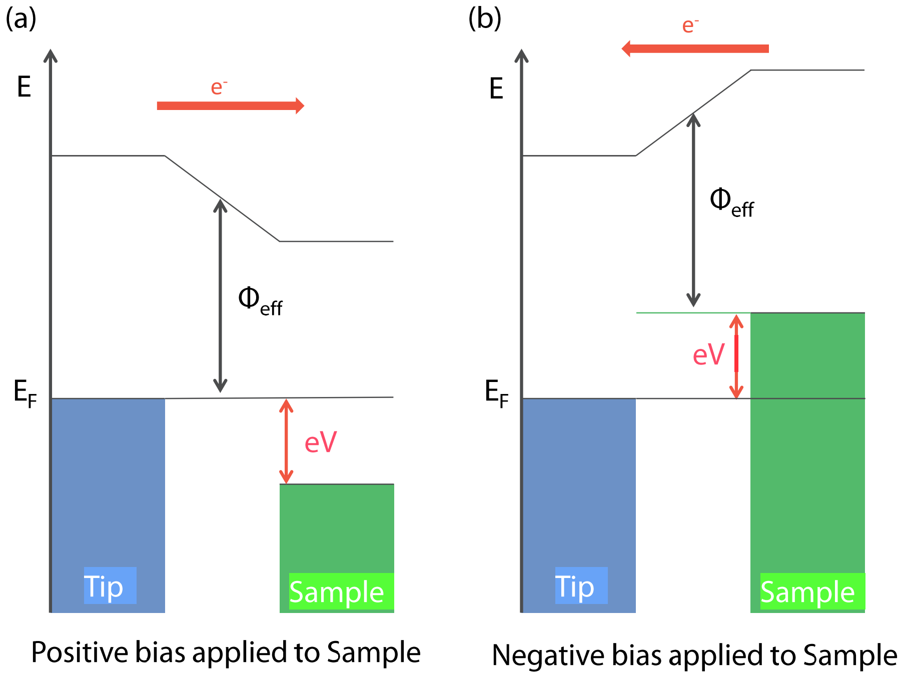

Figure 5: **Schéma énergétique d'un jonction tunnel.** (a) illustre le cas d'une tension positive appliquée à l'échantillon tandis que (b) traite le cas d'une tension négative de l'échantillon. ϕ_{eff} représente le travail d'exctraction moyen, l'énergie est exprimée par rapport au niveau de Fermi E_F.

avec $k = 1.025^{-1} eV^{-1/2} \mathring{A}^{-1}$ et ϕ_{eff} le travail de sortie moyen du substrat et de la pointe. L'énergie $E_{\|}$ est la composante parallèle à la surface de l'echantillon de l'énergie cinétique des électrons et n'a pas de grande influence dans le passage par effet tunnel des électrons entre la pointe et l'échantillon. La valeur moyenne du travail de sortie des métaux étant $\phi_{eff} \simeq 4\ eV$, le facteur de transmission T conduit à une augmentation du courant tunnel d'un facteur 10 par Angström lorsque la pointe s'approche de l'échantillon.

Cette dépendance exponentielle du courant par rapport à la distance entre la pointe et l'échantillon permet d'obtenir des images de la surface de l'échantillon avec une précision de l'ordre du dixième d'angström en scannant la surface ligne par ligne. Pour éviter une collision entre la pointe STM et une éventuelle structure mesurant plusiseurs dizaines d'angströms sur la surface, une boucle de rétro-action permet d'ajuster l'altitude de la pointe pour garder un courant tunnel constant. Ainsi, les déplacements verticaux de la pointe lors du scan sont directement liés à la topographie de la surface de l'échantillon (Fig. 6).

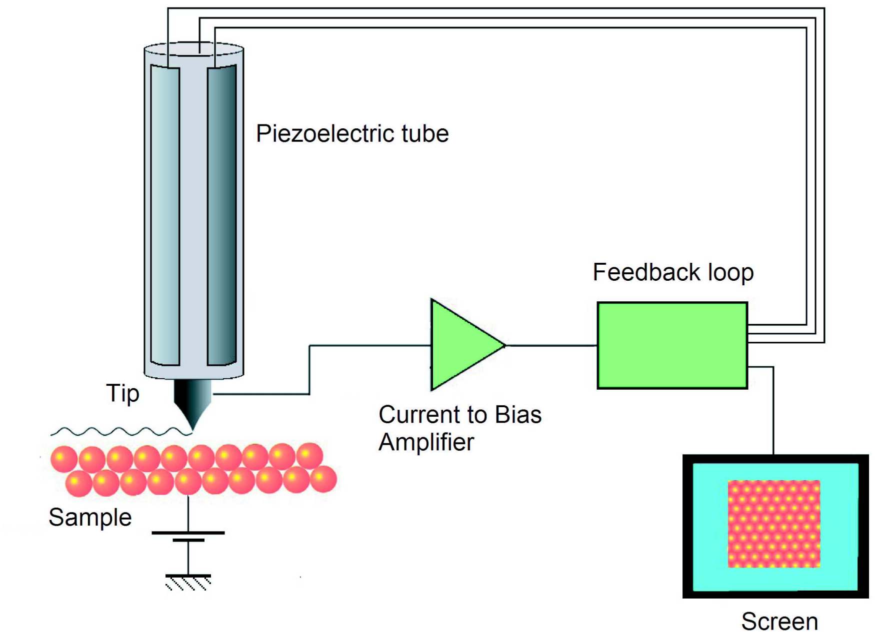

Figure 6: **Principe de fonctionnement d'un STM.** La distance entre la pointe et l'échantillon est régulée grâce à une boucle de rétro-action maintenant l'intensité du courant proche de la valeur consigne.

0.2.2 Spectroscopie tunnel

Le courant tunnel est obtenue par application d'une légère tension entre la pointe et l'échantillon. Cette différence de tension induit un décalage des niveau de Fermi entre la pointe et l'echantillon et ainsi permet d'étudier les densités d'états locales en mesurant l'intensité du courant tunnel pour différentes tensions. Cette operation, appellée spectroscopie tunnel, doit etre effectuée sans boucle de retroaction. Les informations relatives aux densités d'états locales de la pointe et de l'échantillon peuvent alors être extraites de la conductance différentielle obtenue par dérivation du courant tunnel par rapport à la tension :

$$\frac{dI}{dV}(z,V) \propto T(z,E=V,V)\rho_S(V) + \int_0^V \rho_s(E)\frac{dT(z,E,V)}{dV}dE. \tag{4}$$

où la densité d'état de la pointe est considérée constant dans l'intervalle de mesure et la température suffisament basse pour que la distribution de Fermi-Dirac soit approchée par une fonction de Heaviside. En utilisant la définition du facteur de transmission T, on obtient

$$\sigma \equiv \frac{dI}{dV} \propto \rho_S(V)T(z,V,V) \tag{5}$$

Les spectres $dI/dV(V)$ mesurés permettent d'obtenir des informations sur les orbitales électroniques de l'échantillon avec une résolution inférieure au meV.

Cette dernière équation est valide dans le cas d'une spectrocsopie élastique, c'est à dire sans perte d'énergie de la part des électrons passant par effet tunnel de la pointe vers l'échantillon. Dans le cas d'un effet tunnel inélastique, l'énergie cédée par l'électron au système permet d'exciter un transition entre deux niveaux Zeeman, un état vibronique ou un plasmon. Il s'accompagne d'une augmentation du courant mesuré à tension donnée, qui s'explique comme étant l'ouverture un nouveau canal possible pour les électrons passant de la pointe à l'échantillon. Cette augmentation de courant apparait comme une marche symétrique centrée autour du niveau de Fermi dans les spectres de conductance. Pour ce genre de mesure, la résolution en énergie est de 1.26meV.

0.2.3 Densité d'états de la pointe

Techniquement parlant, il est difficile d'obtenir une densité d'état de la pointe parfaitement constante au niveau de Fermi. Il est parfois nécessaire de procéder à une soustraction de la structure de pointe résiduelle pour identifier clairements les signaux qui nous intéressent. Selon la méthode décrite dans [3], la déconvolution se fait selon la formule suivante:

$$\sigma_{deconv}(V) = \sigma_{measured}(V) - \frac{\sigma_{measured}(0)}{\sigma(0)_{tip}} \times \sigma_{tip}(V) + C \tag{6}$$

où $[\sigma(V)]_{measured}$ est le spectre directement issu des mesures, $\sigma_{tip}(V)$ est la structure de pointe obtenue par spectroscopie au dessus du cristal de cuivre et C une constante permettant de ramener le premier point du spectra à la valeur réelle d'ouverture de la boucle de rétro-action. Le résultat de cette déconvolution est présenté en Fig. 7. Cette méthode de déconvolution permet de traiter des strucures de pointes ayant une amplitude relativement faible par rapport aux signaux mesurés.

0.3 Détection de processus de "spin-flip" par STM (Chapitre 3)

En abscence d'électrodes magnétiques dans un STM, il est néanmoins possible de détecter certaines propriétés magnetiques d'atomes ou molécules adsorbés sur une surface. La

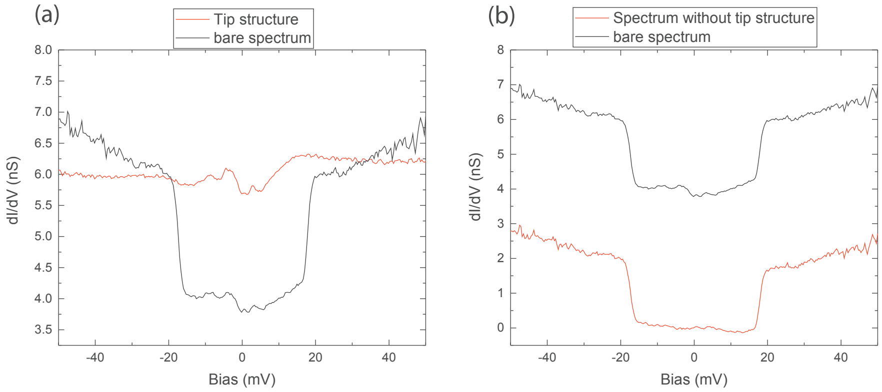

Figure 7: **Spectres obtenus par déconvolution de la stucture de pointe.**

détection fait intervenir un évenement dit de "spin-flip" où le spin d'un atome ou d'une molécule est modifié lors de l'interaction avec un électron passant à travers l'adsorbat.

0.3.1 Spin-flip inélastique

Le premier cas abordé ici est l'excitation par effet tunnel inélastique d'une entité adsorbé en surface. Lors de son passage, l'électron tunnel va céder une partie de son énergie et permettre à l'adsorbat de changer d'état. L'exemple le plus simple est l'atome de manganèse Mn déposé sur un oxide d'aluminium [4] (Fig. 3.2). Cette couche d'Al_2O_3

Dans cet exemple, un champ magnétique permet de lever la dégénérescence des différents états de l'atome de Mn par effet Zeeman. Lorsqu'un spectre dI/dV est effectué dans ces conditions, une double marche centrée autour du niveau de Fermi apparait (Fig. **??**). Elle correspond à l'éxcitation du Mn depuis son état fondamental $ms = 5/2$ vers l'état $ms = 3/2$ par les électrons tunnelant à travers la jonction. L'energie d'activitation de cet effet inélastique est de l'ordre de 0.5 mV et l'Hamiltonien correspondant est le suivant :

$$\mathscr{H}_z = -g\mu_B \hat{\mathbf{J}} \cdot \hat{\mathbf{B}}, \tag{7}$$

La Figure 9 illustre les états avant et après l'intéraction entre l'électon et l'atome. On remarque que le moment magnétique total est conservé, le spin de l'électron passant d'un état $m_s s = -1/2$ vers l'état $m_s = +1/2$.

Dans le cas du système Mn/Al_2O_3, la levée de dégénérescence est activée grâce à un champ magnétique. Cependant, pour certains systèmes particulier, une levée de dégénérescence partielle est rendue possible par l'anisotropie magnétique. L'Hamiltonien s'ecrit alors :

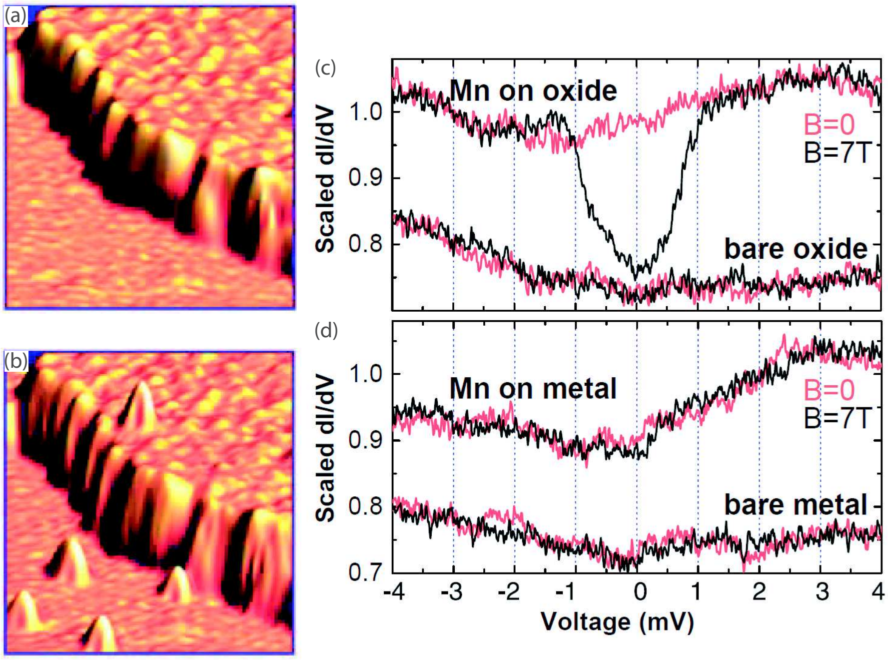

Figure 8: **Spectres obtenus pour le système Mn/Al$_2$O$_3$.** (a) Oxide sans atome de manganèse. (b) Etat de la surface après dépôt des atomes magnétiques. (c) Spectres obtenus en présence d'un champ magnétique levant la dégénérescence entre les differents états magnétiques. (d) Spectres obtenus sans champ magnétique. L'excitation magnétique n'est plus possible à cause de la dégénérescence des états. [4]

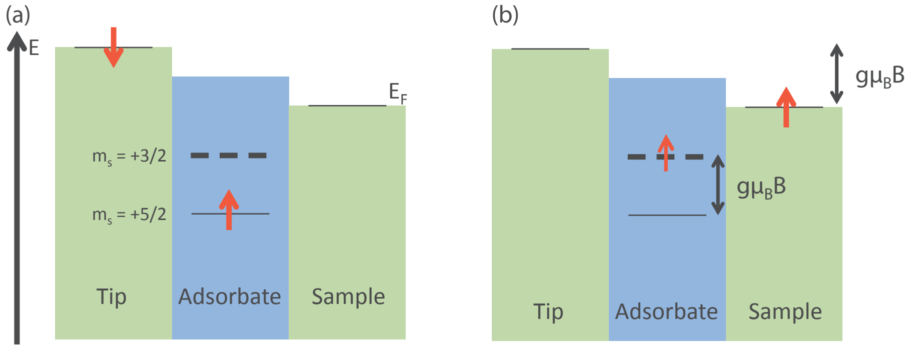

Figure 9: **Conservation du moment magnétique.** (a) Etat initial avant excitation de l'adsorbat. (b) Etat final après excitation. Le moment magnétique total est conservé.

$$\mathscr{H}_s = D\hat{S}_z^2 + E(\hat{S}_x^2 - \hat{S}_y^2), \tag{8}$$

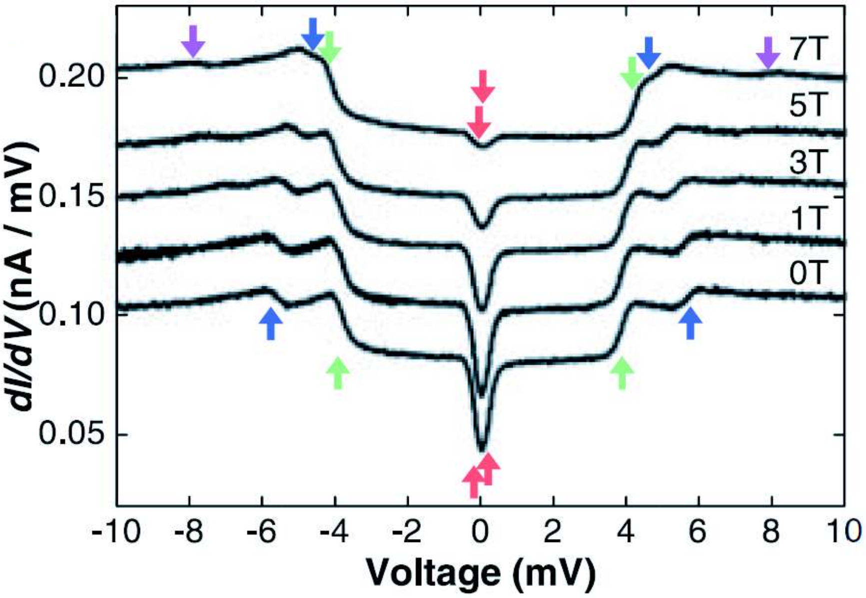

Figure 10: **Spectres obtenus pour le système Fe/Cu$_2$N.** Les différents spectres montrent la réponse du système en fonction du champ magnétique appliqué, prouvant l'origine magnétique des états excités [5].

où D est appelé parametre d'anisotropie longitudinale qui représente la tendance du spin à s'aligner le long de l'axe de quantification z. Le paramètre E, appelé anisotropie transverse, correspond à l'orientation dans le plan perpendiculaire à l'axe z du spin. L'influence de cette anisotropie magnétique dans les spectres de conductance peut être illustrée avec le système composé d'un atome de fer dépose sur un ilôt de nitrure de cuivre Cu$_2$N [5]. La figure 10 montre qu'un signal inélastique est mesuré, même en absence de champ magnétique. Les différentes excitations mesurées correspondent aux transitions entre l'état fondamental et les différents états excités accessibles.

0.3.2 Effet Kondo

Il est également possible de détecter certains effets de spin-flip lors d'une spectroscopie élastique. L'effet Kondo est un processus apparaissant lorsqu'une impureté de spin 1/2 est déposée à la surface d'un metal. En dessous d'une température propre au système considéré, appelée température Kondo, un couplage anti-ferromagnetique apparait entre le spin de l'impureté et les électrons environnants du métal. A cause de la dégénérescence entre les états "up" et "down" du spin de l'impureté, il existe un échange permanent entre les deux

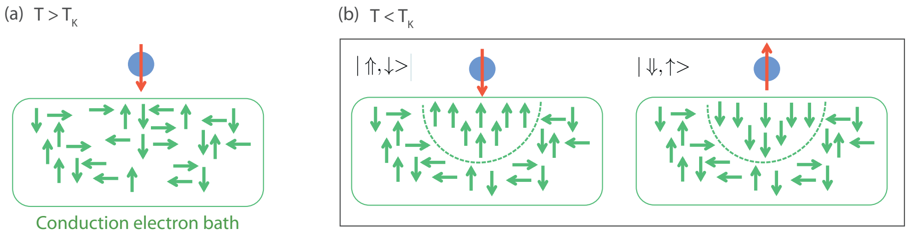

Figure 11: **Schéma décrivant l'effet Kondo.** (a) Au dessus de la température Kondo, le spin de l'impureté ne peut pas être écranté par les électrons du métal. (b) Quand la température du système passe en dessous de T$_K$, un lien s'établit entre l'impureté et les électrons du métal. L'état fondamental du système est alors dégénéré, le spin de l'impureté pouvant avoir l'une ou l'autre des orientations possibles.

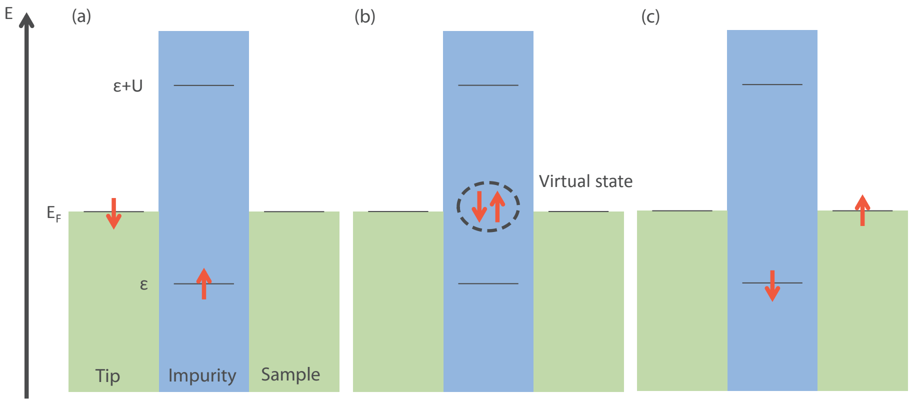

Figure 12: **Schéma énergétique de l'effet Kondo.** (a) Avant le processus de passage par effet tunnel tunneling process. (b) Etat virtuel de transistion entre les deux états. (c) Etat après le passage par effet tunnel.

états du système. Lorsqu'un électron passe à travers l'impureté, il participe à l'echange comme décrit dans la figure Fig. 12.

Cette implication de l'électron tunnel dans l'effet Kondo se traduit dans les spectres de conductance par une résonnance située au niveau de Fermi. La largeur de la résonance est directement liée au couplage entre l'impureté et les électrons du métal hôte ainsi qu'à la température Kondo du système, ce qui permet une extraction de ces valeurs depuis les données expériementales.

0.4 Ferrocène (Chapitre 4)

0.4.1 Adsorption du ferrocène

Nous avons commencé notre étude des métallocène par le ferrocène. Les molécules ont été déposées sous vide sur un échantillon froid. Tout d'abord, sur un substrat Cu(111), nous avons observé la formation spontanée (Fig. 17a-b) de deux types de réseaux. Le premier, appelé Compact, se caractérise par des protusions circulaires arrangées en lignes et colonnes et associées à des molécules verticales. Le second réseau, appelé Zigzag, présente une structure plus sophistiquée mais apparait à la surface de l'échantillon avec la même probabilité que le réseau compact. La déposition du ferrocène sur une orientation cristalline différente, Cu(100), a donné un résultat similaire avec deux réseaux (Compact et Zigzag) cohabitants à la surface de l'échantillon (Fig.17c). La présence équiprobable des deux réseaux sur différentes orientations crystallines suggère une physisorption des molécules à la surface du cuivre.

Une étude plus approfondie des images STM a montré des protusions de forme allongée sont visibles entre les protusions circulaires. Nous avons interprétés ces batonnets comme étant des marqueurs de molécules adsorbées horizontalement entre les molécules verticales. De cette hypothèse, nous avons déduit un modèle d'adsorption (Fig. 14). La viabilité et stabilité de ce modèle a été confirmée par calculs DFT par nos collaborateurs théoriciens. Ils ont également pu, à partir de ce modèle, simuler des images STM correpondant parfaitement à nos résultats expérimentaux et confirmer la physisorption des molécules. Une telle organisation des molécules à la surface de l'échantillon, avec des molécules verticales et horizontales interagissant via des forces de van der Waals, correspond à la structure des cristaux de ferrocène dans un plan(110). De plus, nous avons expérimentalement confirmé la présence des molécules horizontales à la surface de l'échantillon en retournant certaines d'entre elles par l'application locale d'un pulse de tension de 2V sur le réseau moléculaire.

0.4.2 Dopage de spin du ferrocène

Les études théoriques ont montré que l'adsorption d'un atome métallique supplémentaire permet de changer les propriétés magnétiques d'un métallocène. Nous avons commencé par un assemblage manuel et controlé du nouveau système Co-FeCp$_2$. Pour ce faire, nous capturons une molécule de ferrocène sur la pointe STM et la déposont sur un atome de cobalt isolé sur le cristal Cu(111). La nouvelle molécule ainsi crée est stable et présente une hauteur apparente de 3.5 Å, supérieure à ce que l'on obtient pour un simple ferrocène isolé. Un spectre en conductance enregistré sur ce système montre une résonannce au niveau de

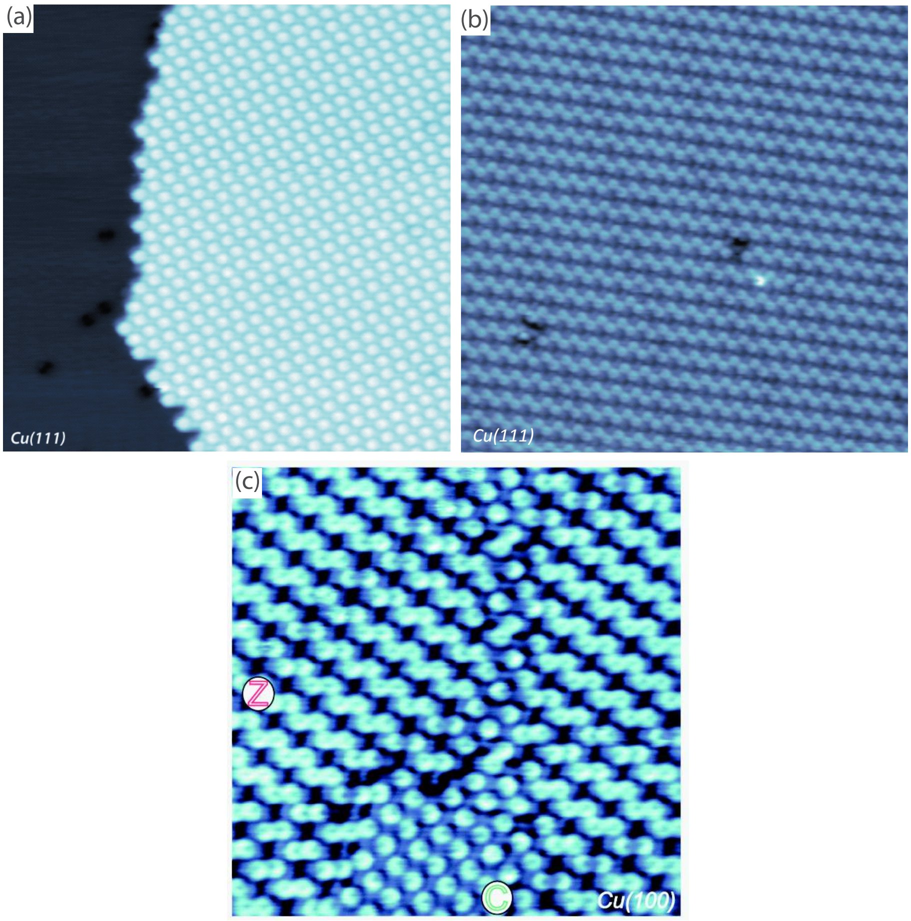

Figure 13: **Images STM des réseaux de ferrocène.** (a) Réseau de type compact sur Cu(111). (b) réseau de type zigzag sur Cu(111). (c) Différents réseaux compact et zigzag observés sur Cu(100).

Fermi associée à une effet Kondo dont la température Kondo est estimée à 33 ± 7 K. Les résultats obtenus par DFT par nos collaborateurs montrent que dans ce système, l'atome de cobalt cède une partie de sa charge au ferrocène. Ceci assure une liaison relativement stable entre l'atome et la molécule, et conduit à une magnétisation de l'atome de fer. Nous avons reproduit la même manipulation sur Cu(100), où la résonance apparait dans les spectre en conductance pour le système Co-$FeCp_2$ sur Cu(100) plus large en énergie. La température Kondo de ce système est alors estimée à 114 ± 7 K. L'accroissement de la largeur de la résonance indique une différence de couplage entre le système et la surface, et confirme la nature Kondo de l'effet mesuré.

Nous avons voulu confirmer expérimentalemnt ces prédictions en déposant des atomes de cobalt sur nos réseaux moléculaires. Nous avons évaporé les atomes de cobalts sur

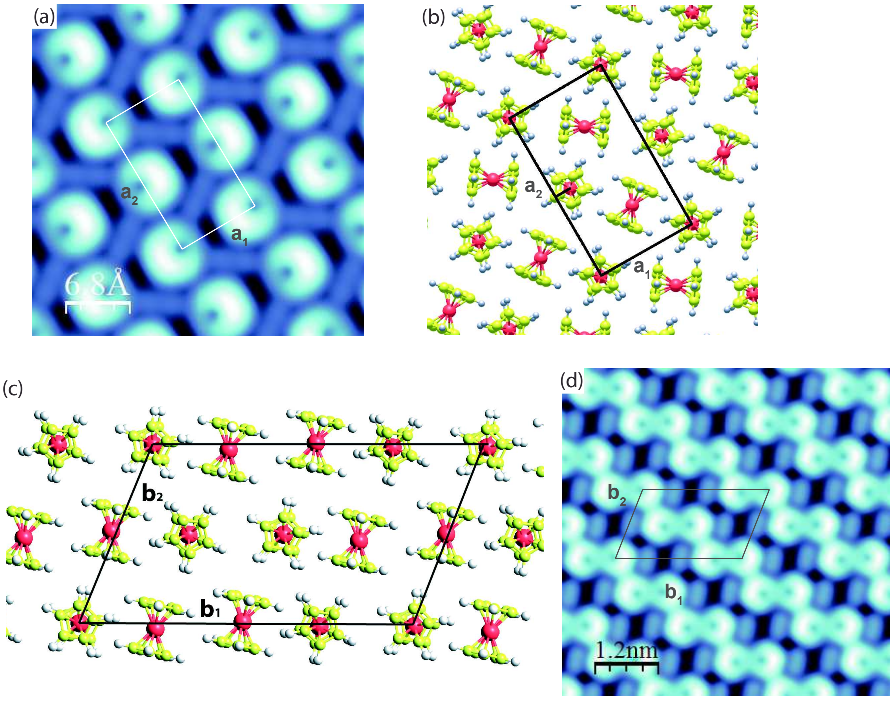

Figure 14: **Réseaux de ferrocène.** (a) Image STM simulée par DFT du réseau compact. (b) Schéma de la structure du réseau compact. (c) Schéma de la structure du réseau zigzag. (d) Image STM simulée par DFT du réseau zigzag.

des réseaux de molécules pré-existant et refroidis à 4 K. La présence d'atomes de cobalt supplémentaires sur les réseaux de ferrocène apparait sur les images STM comme une protusion circulaire haute de 0.6 Å. La forme circulaire suggère que les adatomes s'adsorbent préférentiellement sur les molécules verticales. La hauteur apparente est cohérente avec les mesures effectuées sur la molécule isolée, et les spectres en conductances montrent une résonannce Kondo de température Kondo égale à 38 ± 6 K sur Cu(111) très similaire à ce qui est obtenu pour le système isolé. Ces données expérimentales nous laissent supposer que les atomes de cobalt ne restent pas au-dessus du réseau mais traverse la couche de molécule et se positionne entre le ferrocène et le cuivre.

Les simulations par DFT ont montré que les atomes de cobalt sont bien plus stable quand positionnés entre le ferrocène et la surface plutôt qu'au sommet d'une molécule verticale. La différence d'énergie entre les deux models est de 3 eV par molécule, et seul la configuration avec le cobalt situé sous le ferrocène permet d'obtenir une image STM simulée correspondant aux résulats expérimentaux. Tous ces éléments confirment la supposition selon laquelle les deux molécules $CoFeCp_2$ isolées et incluses dans le réseaux sont identiques.

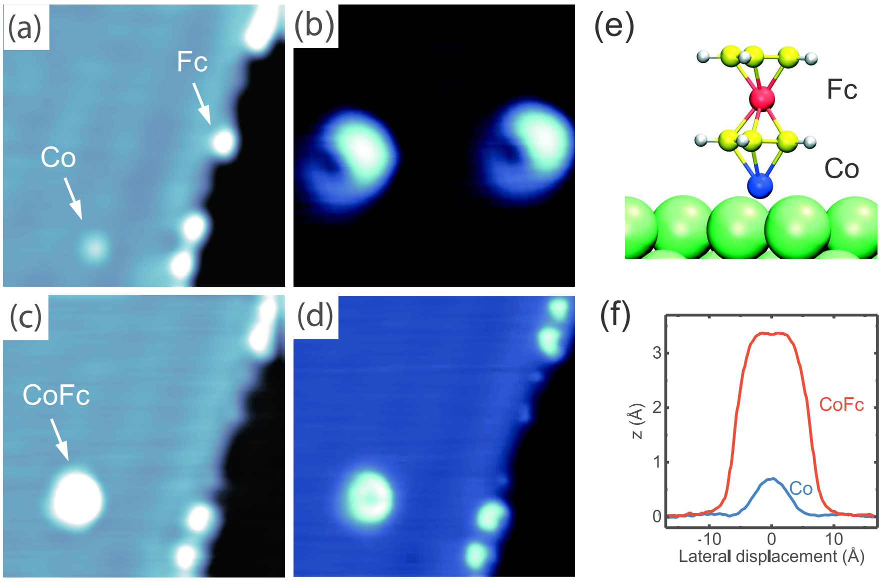

Figure 15: **Construction du système $CoFeCp_2$ isolé.** (a) Une molécule $FeCp_2$ isolé en bordure de marche est contactée puis adsorbée sur la pointe STM.(b) La présence du $FeCp_2$ au bout de la pointe est confirmée par la présence d'un anneau sur les images d'atomes de Co isolés. (c) La molécule de ferrocène est déposée par contact par dessus l'un des atome de cobalt isolé. (d) Même image qu'en (c) traitée avec un filtre laplacien permettant de distinguer l'anneau apparant du nouveau système. (e) Structure chimique du système $CoFeCp_2$. (f) Comparaison des hauteurs apparentes du cobalt et du $CoFeCp_2$ sur Cu(111).

0.5 Nickelocène (Chapitre 5)

Nous avons également étudié les propriétés d'un métallocène magnétique, à savoir le nickelocène $NiCp_2$ de spin $S = 1$. Nous avons déposé nos molécules en suivant la même méthode que pour le ferrcocène. Nous avons de nouveau obtenus des molécules physisorbées. Les images STM ainsi que les résultats des modèles DFT montrent que de nouveau des molécules horizontales et verticales forment spontanément des réseaux à la surface de l'échantillon quelque soit l'orientation cristalline choisie, Cu(100) ou Cu(111). Cependant, sur l'orientation Cu(100), des molécules isolées apparaissent stables à coté des réseaux.

Les spectres en conductances réalisé sur les molécules isolées sur la surface ont donné une marche symétrique centrée autour du niveau de Fermi caractéristiques d'un phénomène de transport par effet tunnel inélastique. L'energie d'excitation est ici de 3.2 meV, ce qui correspond aux mesures d'anisotropie magnétique obtenues précédement [6]. Pour confirmer la nature de l'excitation, nous avons réalisé plusieurs série de mesures XMCD sur la ligne Deimos au synchrotron Soleil. Ces mesures ont montré que le spin de la molécule

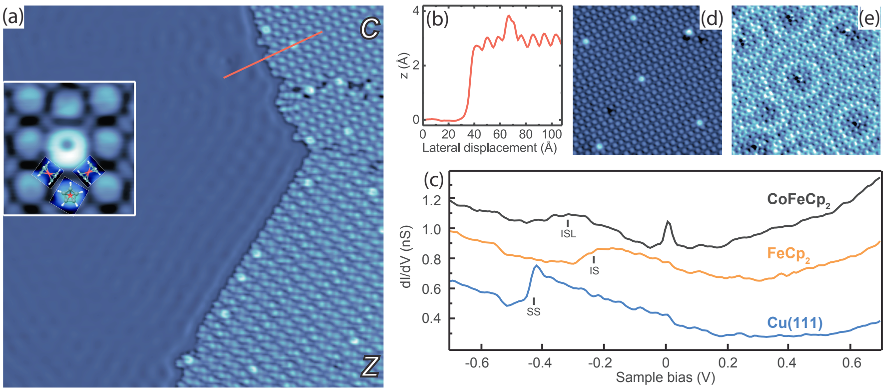

Figure 16: **Etude STM d'un CoFeCp$_2$ inclus dans un réseau moléculaire.** (a) La présence des systèmes CoFeCp$_2$ dans le résau est identifiés par la présence de protusions claires. Le zoom montre la disposition des différentes entitées dans le réseau. (b) Hauteur apparente du réseau ainsi que de la nouvelle molécule. (c) Spectres en conductance du cristal Cu(111), du ferrocène et du système CoFeCp$_2$. Les courbes sont décalés en ordonnées de 0 nS, 0.3 nS et 0.5 nS respectivement (d) Image d'un CoFeCp$_2$ et (e) carte en conductance obtenue à courant constant (-0.1 V, 0.5 nA, 20×20 nm^2).

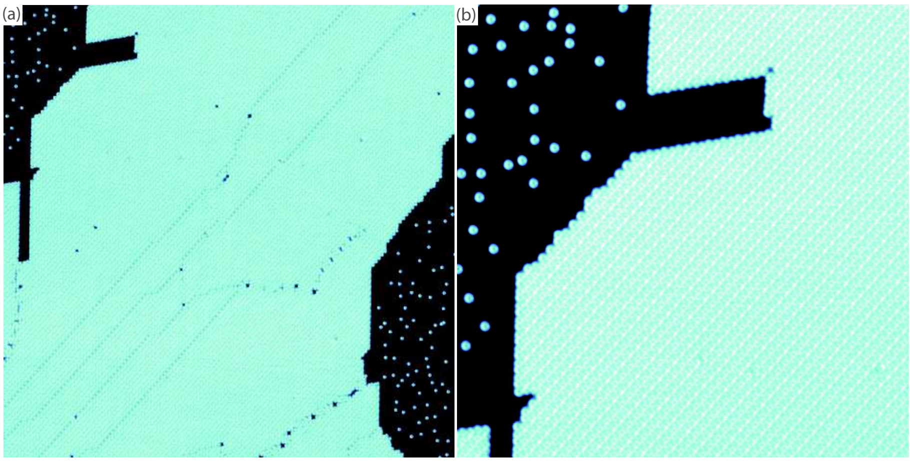

Figure 17: **Molécules de nickelocènes déposées sur Cu(100).** (a) Réseau auto-assemblé de nickélocene sur Cu(100° (Configuration dite paire) et molécules isolées. (50× 50 nm^2. (b) Grossisement sur la partie supérieure gauche du réseau (20×20 nm^2.

était conservé lors de l'adsorption sur la surface, ainsi que la subsitance d'une anisotropie magnétique éstimée à 3.5 meV. Ces résultats ont été confirmés par les calculs DFT de nos collaborateurs. Nous pouvons alors considéré l'excitation inélastique de nos molécules dans la jonction tunnel comme une possibilité de surmonter l'anisotropie magnétique de la molécule, permettant ainsi de contrôler l'orientation du spin dans la molécule par modification

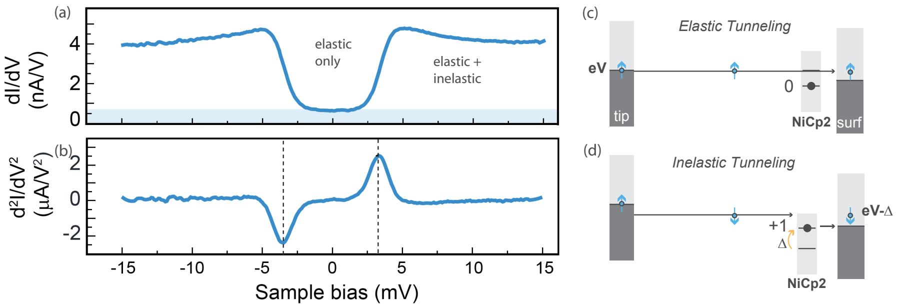

Figure 18: **Spectroscopie du nickelocène.** (a)Spectres en conductance obtenu à basse tension au dessus d'une molécule isolée. (b) dérivée du spectre en conductance par rapport à la tension. (c) Schéma illustrant le passage par effet tunnel de façon élastique puis inélastique (d). Les spectres ont été acquis avec un dispositif à verrouillage de phase (modulation de 150μV en ouvrant la boucle de retroaction à 50 pA et -15 mV à 2.4 K.

de la tension aux bornes de la jonction tunnel. Des résultats identiques ont été obtenus pour des molécules intégrées dans un réseau.

La possibilité de transfert des métallocènes depuis la surface vers la pointe STM nous a permis de créer de manière reproductible une pointe moléculaire magnétique. L'adsorption du nickelocène au bout de la pointe STM mène à une légère modification de l'environement de la molécule, celle-ci étant mainteant adsorbée sur un atome unique plutôt que sur la surface d'un cristal. Il s'en suit une modification de l'anisotropie qui augmente de 15%, et qui augmente en conséquence l'énergie d'éxcitation mesurable dans les spectres en conductance (Fig. 5.15).

Enfin, la présence de la molécule à l'extrémité de la pointe nous permet d'étudier un système composé de deux metallocènes se faisant face dans la jonction STM (Fig. 5.17). Les spectres en conductances sur un tels système ont montré un phénomène de double excitations de spin. La première énergie d'excitation correspond alors à l'excitation d'une molécule seulement dans la jonction tandis que le la seconde énrgie d'excitation correspond au spin-flip des deux molécules simulaténement lorsqu'un électron passe à travers la jonction. L'augmentation significative de la conductance est alors interprété comme une multiplication des canaux de conduction possible à travers le système ainsi que par une meilleur conductance des canaux incluant des effets inélastiques.

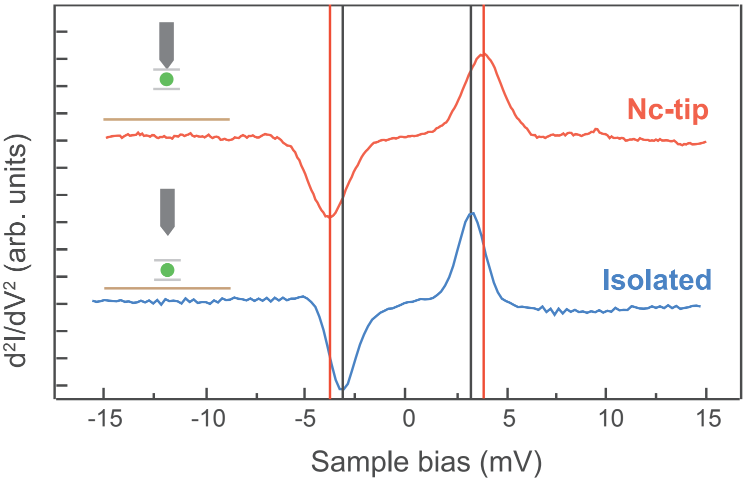

Figure 19: **Spectroscopie d’une pointe moléculaire.** Comparaison entre les spectres obtenues pour une pointe moléculaire (rouge) et une molécule adsorbée sur la surface (bleue) à 2.4 K.

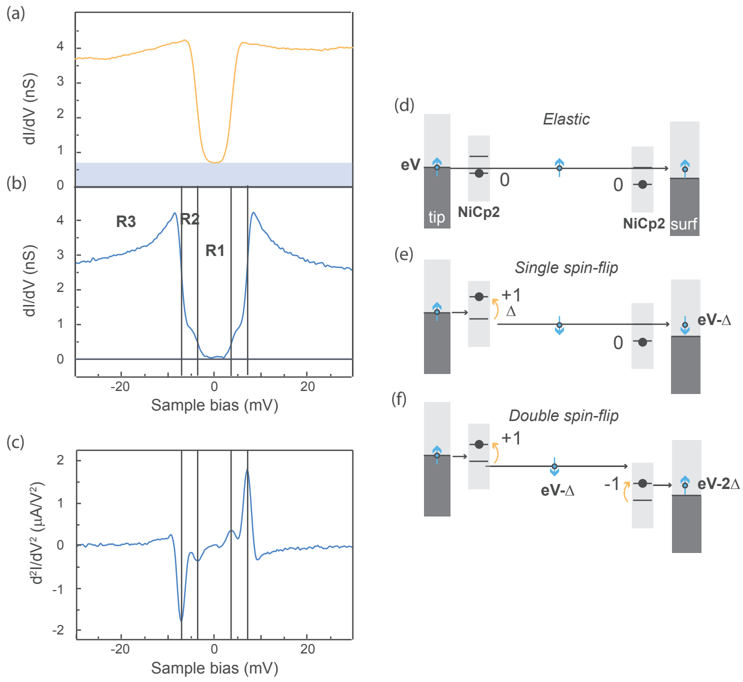

Figure 20: **Spectre d’une double excitation de spin.** (a) Spectre en conductance obtenu à basse tension au dessus d’une molécule isolée. (b) Spectre obtenu au dessus de la même molécule mais avec une pointe moléculaire (c) Dérivée du spectre précédent par rapport à la tension. (d) Schéma illustrant le passage par effet tunnel de façon élastique. (e) illustre le cas de la première excitation où seule une des deux molécules est excitée tandis que (f) montre le processus à l’oeuvre lors d’une double excitation.

Chapter 1

Introduction

Nowadays, semiconductor technology is reaching a limit where elements are a few nanometers apart: 22 nm in 2014, 14 nm in 2016, 5 nm for 2020. At this level, information processing becomes extremely challenging due to quantum effects and new strategies need to be envisioned to keep on miniaturizing devices. A promising route to replace the metal-oxide-semiconductors technology is spintronics where not only the charge of the electrons but also the electronic spin is exploited in order to process information. Spintronics is seen as a promising way to improve the efficiency of both data processing and storage technologies. Efforts in the field of spintronics aim at improving existing technology by conceiving new materials, but also, in a more radical effort, at finding novel ways of manipulating the electronic spin. One possibility consists, for example, in incorporating organic or organometallic molecules into spintronic devices to improve their performances, as shown in a number of pioneering studies. The necessity for a microscopic characterization tool has motivated, in turn, the development of spintronics at the single-molecule level, also known as molecular spintronics. The work presented in this thesis belongs to this new field of research. We mainly focus on analyzing and controlling the spin state of isolated molecules using a scanning tunneling microscope (STM). This chapter presents the main ideas behind the field of spintronics from the spin polarization of the current to single-molecule junctions. We also introduce the general properties of the molecules we investigated, *i.e.* the molecules of the metallocene family. These molecules have been little studied so far and, as we will show all along this thesis, offer a playground to explore spintronic functionalities at the molecular level.

1.1 Spintronics

1.1.1 Basic concepts

The main idea in spintronics is to detect and control the spin of electrons flowing through a device. In a pioneering work, Mott [7] showed that it is possible to model the electron current flowing through a ferromagnet by two non-interacting spin-polarized currents of conductance $G_\uparrow$ and $G_\downarrow$, respectively. Spin-dependent electron tunneling was however only experimentally evidenced in 1970 by Tedrow and Meservey [8, 9], *i.e.* more than 30 years later Mott's work. The spin-polarized current was produced from various ferromagnetic electrodes and after tunneling across an alumina insulating barrier (Al_2O_3) was detected via a thin superconducting aluminum film. An important step forward was achieved by Jullière in 1975, who reported the first conductance measurements on a ferromagnet/insulator/ferromagnet tunnel junction [1], where two ferromagnetic electrodes (Co and Fe) with different coercive fields were separated by a Ge insulating slab. Jullière proposed that the tunneling current depends on the relative orientation of the magnetizations of the two ferromagnets, parallel ($\uparrow\uparrow$) or antiparallel ($\uparrow\downarrow$) (Fig. 1.1). Let us define $\Delta_{\uparrow(\downarrow)}$ and $\delta_{\uparrow(\downarrow)}$ as the the amplitude of the DOS of majority and minority spins, respectively, for each ferromagnet. The arrows refer to spin-up and spin-down electrons. The conductance for parallel and antiparallel alignment is proportional to the product of the density of states (DOS) of the two ferromagnets, which yields, respectively, $G_{\uparrow\uparrow} \propto (\Delta_\uparrow)^2 + (\delta_\downarrow)^2$ and $G_{\uparrow\downarrow} \propto \Delta_\uparrow\delta_\downarrow + \delta_\downarrow\Delta_\downarrow$. Assuming that $\Delta \gg \delta$, then $G_{\uparrow\uparrow} \propto \Delta^2$ and $G_{\uparrow\downarrow} \propto 2\Delta\delta$. In this simple example, the $\uparrow\uparrow$ configuration has a higher conductance than the $\uparrow\downarrow$ configuration. The change of the conductance in the junction can then be expressed as a magnetoresistance (MR)

$$\mathrm{MR} = \frac{G_{\uparrow\uparrow} - G_{\uparrow\downarrow}}{G_{\uparrow\downarrow}}. \tag{1.1}$$

Alternatively, we may define a polarization for the junction as [10]

$$P_n = \frac{\rho_\uparrow v_\uparrow^n - \rho_\downarrow v_\downarrow^n}{\rho_\uparrow v_\uparrow^n + \rho_\downarrow v_\downarrow^n} \tag{1.2}$$

where $v_\uparrow^n$ and $v_\downarrow^n$ denote the spin-dependent Fermi velocity and ρ the density of states of electrons. The tunneling polarization is expressed as $P_{n=0} = (\rho_\uparrow - \rho_\downarrow)/(\rho_\uparrow + \rho_\downarrow)$ assuming that the tunneling barrier is not spin-selective. The current polarization is $P_{n=1} = (I_\uparrow - I_\downarrow)/(I_\uparrow + I_\downarrow)$. The two polarizations $P_{n=0}$ and $P_{n=1}$ are not identical.

The practical realization of a tunneling magnetoresistance (TMR) was carried out with two ferromagnets insulated by a tunnel barrier of Al_2O_3 in 1995 [11]. On another hand,

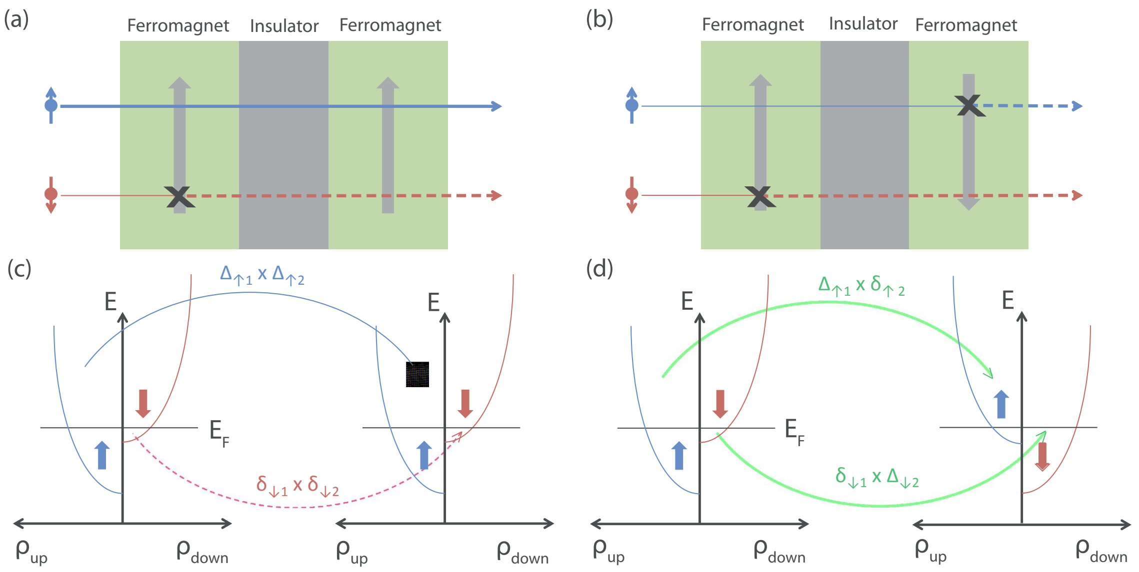

Figure 1.1: **Principle of spin-polarized tunneling between magnetic electrodes.** (a) Parallel, and (b) antiparallel magnetizations.

about ten years before, a giant magnetoresistance (GMR) [12, 13] was instead discovered in "spin valve" devices comprising two ferromagnets separated by a nonmagnetic metallic layer. The working principle of such a GMR device is very similar to a TMR device, however the electrons flow ballistically from one ferromagnet to the other, instead of tunneling. The non magnetic spacer is only a few namometer thick in order to ensure ballistic transport, but sufficient to magnetically decouple the ferromagnets. An electron passing through this multilayer device will be scattered more if the ferromagnets have opposite magnetizations. The device has then a lower conductance than in the parallel case and the collected current differs for the two configurations. A hard disk storing binary information can use the difference in conductance between parallel and antiparallel alignments as a method of storing 0s and 1s. The GMR effect, discovered by Albert Fert and Peter Grünberg (who consequently received the Nobel prize), has boosted the technology of magnetic storage media and brought new products on the market.

1.1.2 Organic and molecular spintronics

A key point of any spintronic device is that spins are injected at a location that differs from where they are detected (Fig. 1.1). During the electron transfer process across the non magnetic layer, the spin population tends to relax towards its non spin-polarized state due to spin-flip scattering events [14]. One of the central research areas in spintronics

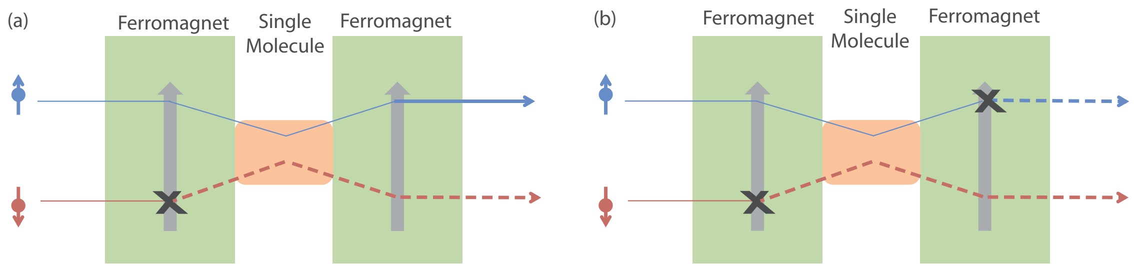

Figure 1.2: **Single-molecule spin valve.** (a) Parallel, and (b) antiparallel magnetizations.

therefore consists in perfecting this transfer process. A number of pioneering studies have recently shown that the performance of spintronic devices is superior when organic molecules separate the ferromagnets instead of a metallic non magnet [15]. The spin-orbit and hyperfine interactions are in fact weak in organic molecules, resulting in considerably long spin relaxation lengths. Specific functionalities can also be built into the molecules contrary to a metallic spacer and new spintronic concepts may then be explored. This motivates the development of spintronics at the single-molecule level and, in particular, of a single-molecule spin valve (Fig. 1.2) [16, 17]. The working principle of such a device is similar to the TMR (Fig. 1.1), except that the molecule adds more possibilties thanks to molecular engineering techniques.

There have been several investigations demonstrating convincingly that spin-polarized currents can be injected into single molecules such as carbon nanotubes [18, 19] or H_2-Phthalocyanine molecules [20]. All these studies show that two critical factors impact the spin-polarized current flowing across the molecule: (1) the intrinsic ability of the molecule to conduct, (2) the interface between the molecule and the ferromagnetic electrodes [21]. To understand this, we consider the situation depicted in Fig. 1.3 where a simple molecule is placed on a ferromagnetic surface. When the two are well separated (Fig. 1.3a), the overall DOS is simply the superposition of the individual DOS of the two spin components (blue represents the spin-up DOS and red the spin-down DOS). Once the molecule hybridizes with the surface (Fig. 1.3b), its spin-dependent energy levels shift and broaden into two resonances. The hybridization differs for the two spin components and the spin-polarization of the junction at the Fermi level remains governed by the DOS of the surface (Fig. 1.3b). However, if the broadened molecular resonances cross the Fermi level (Fig. 1.3c), the spin polarization is then governed by a new hybrid interfacial state. It is this new state that determines the spin-polarization of the junction, which can be dramatically different, and even reversed, compared with the polarization of the electrodes.

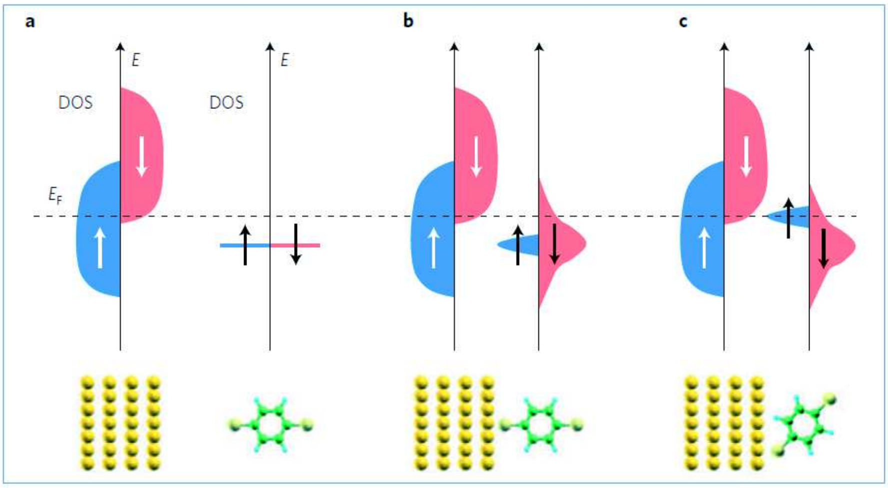

Figure 1.3: **Spin filtering mechanism at an organic/inorganic hybrid interface.** Figure taken from [22].

A control of these factors at the molecular scale could open up the exciting prospect of precisely tuning the spin polarization of a spin valve through a custom-made chemistry and an accurate choice of the electrode material. A molecule could act in particular as a spin filter, similarly to the oxidized layer introduced in macroscopic spintronic devices (see Fig. 1.9). To further increase device performances it is also possible to introduce some spin functionality into the molecule. The spin state can then be controlled, for example by changing the molecular conformation [23–29], or by changing its spin through a metalation process, also known as spin doping [30–33] as we will see later in the thesis.

1.2 Spin-dependent signatures in single molecules using STM

As we mentioned above, the ability to manipulate the magnetic properties and the spin-polarized current through single molecules is at the basis of molecular spintronics. Within this context, the investigation of single molecules with built-in magnetic moments that are coupled to ferromagnetic, or more generally, to metallic electrodes represents a model playground for exploring novel spintronic concepts [34, 17]. Among the most commonly studied molecules we find transition metal phthalocyanine (Pc) or porphyrin molecules. The magnetism of these planar molecules arises from the unpaired spins residing in the *d*-orbitals of the transition metal atom at the center of the molecule (Fig. 1.4a). The STM has been employed for gathering direct microscopic evidence of how specific, well-characterized adsorption configurations on a metal surface can lead to different electronic and magnetic

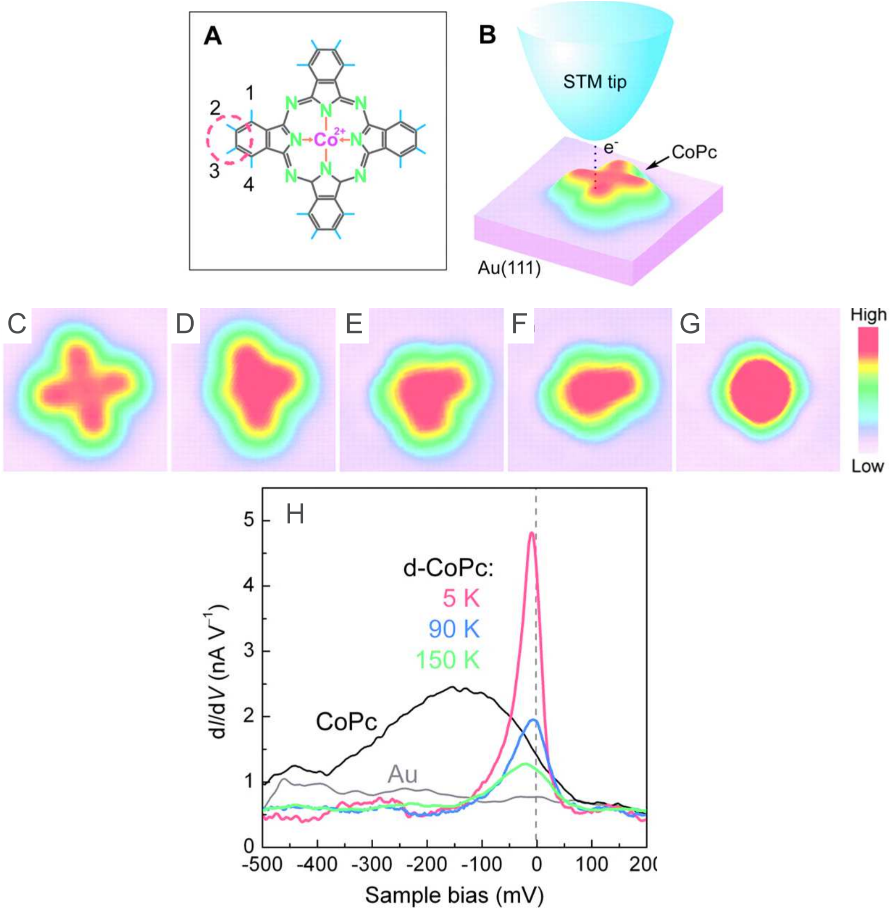

Figure 1.4: **STM tip-induced dehydrogenation of a single CoPc molecule.** (a) Structural formula of CoPc. Hydrogen atoms noted 2 and 3 are dissociated in the experiments. (b) Sketch of the dehydrogenation induced by the STM current. (c-g) STM images of a single CoPc molecule during each step of the dehydrogenation process, from (c) an intact CoPc to (g) dehydrogenated CoPc. (h) Kondo resonance of dehydrogenated CoPc at different temperatures. Figure adapted from [23].

behaviors. In particular, on a surface the interaction between the molecular spin and the electron spins of the host metal can give rise to a many-body phenomenon known as the Kondo effect (see Chapter 3). In the dI/dV spectrum taken by positioning the STM tip above the transition atom of the molecule, the signature of the Kondo effect is detected as a narrow resonance (the Kondo resonance) near E_F (Fig. 1.4h). A standard STM tip (non magnetic) is sufficient to detect this resonance, explaining the profusion of studies devoted to the Kondo effect in molecular systems [35]. Interestingly, the line shape of this resonance is sensitive to the way the molecule hybridizes with the surface. It is therefore possible to monitor how the hybridization affects the molecular magnetism, although in practice it is experimentally

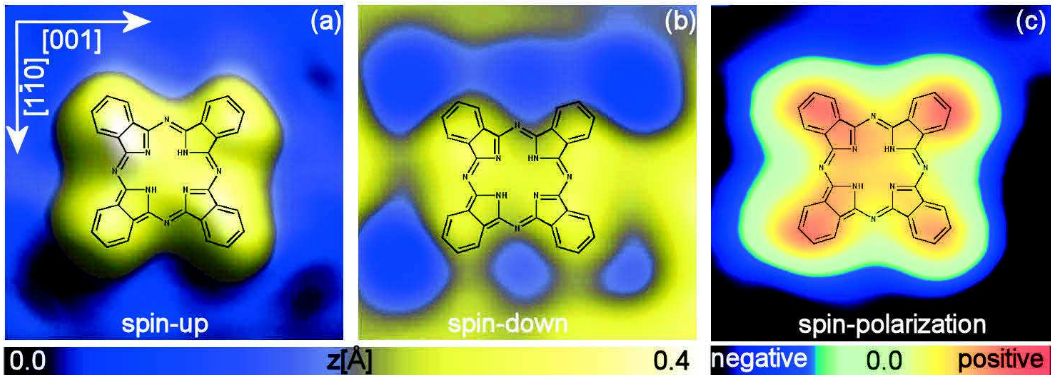

Figure 1.5: **Spin-polarized STM.** SP-STM images for H_2Pc adsorbed on 2 ML Fe/W(110) at a bias of +0.05 V. In (a) the molecule is adsorbed on a domain with "up" magnetization, while in (b) on a domain with "down" magnetization. (c) Difference between the two images showing the spatial dependency of the spin polarization. Figure extracted from [36].

difficult to extract quantitative information. To do so, one then needs to complement the study with density functional theory calculations. For example, in an important work, Zhao et *al.* [23] changed the magnetic nature of a cobalt phthalocyanine (CoPc) molecule adsorbed on Au(111) surface by altering its structure through a dehydrogenation process (Figs. 1.4b-g). For a pristine CoPc molecule sitting on the Au(111) surface they observed the d-orbital of the cobalt ion to be an energetically broad resonance lying below the Fermi energy. After cutting away eight hydrogen atoms from the periphery of the molecule with voltage pulses from a STM tip, the broad d-resonance is presumably replaced by a Kondo resonance with a high Kondo temperature, typically above 200 K (Fig. 1.4h). DFT calculations show that the dehydrogenation implies a change in the Co surface distance, hence in its magnetic moment.

Another possibility for probing spin-related properties in molecules is spin-polarized STM (SP-STM). This technique exploits a similar effect as in TMR devices, while preserving the spatial resolution of the STM. A SP-STM junction consists in replacing one ferromagnet (Fig. 1.1) by a magnetic tip and the other ferromagnet by a magnetic surface (Fig. 1.10). The tip and surface are magnetically decoupled by a vacuum barrier. The spin polarization of the tunneling electrons can reach 50% at selected biases and produces a spin-dependent contrast in the differential conductance. Magnetic domains and walls of metal films and nanostructures on surfaces could be imaged with SP-STM [37]. This technique has even proven to be sensitive to the spin-polarization of single atoms [38–40] as well as molecules [41, 42, 36, 20] adsorbed on magnetic surfaces. In the latter case it is possible to observe at the atomic scale the change in spin polarization produced by the hybridization of the molecule with the surface. For example, Atodiresei *et al.* [36] used SP-STM to investigate

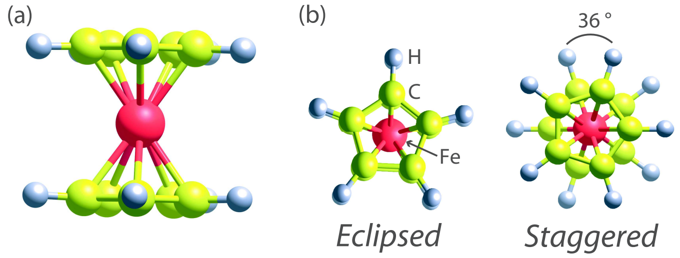

Figure 1.6: **Structure of a metallocene.** Here, we took the example of ferrocene. (a) Side view. (b) Top view of the two possible configurations for the Cp rings.

	Molecule height	Cp ring diameter	C-C bond length	M-C bond length
Ferrocene	3.4 Å	4.6 Å	1.40 Å	2.04 Å
Nickelocene	3.55 Å	4.7 Å	1.43 Å	2.17 Å

Table 1.1: **Computed distances for a ferrocene and a nickelocene molecule.** The transition atom is noted M.

organic H_2Pc molecules adsorbed on a magnetic Fe/W surface. The surface magnetization is out-of-plane with two possible orientations, either up or down. They showed that while the adsorbed molecule magnetic moment remains negligible, the states near the Fermi level are spin polarized : with an up magnetization of the surface (Fig. 1.5a), the SP-STM image yields a different contrast compared to the image with down magnetization (Fig. 1.5b). The difference between the two allows then to locally map the spin-polarization of the junction (Fig. 1.5c). H_2Pc molecules show a high, locally varying spin polarization ranging from attenuation to inversion with respect to the ferromagnetic Fe film (dark blue in Fig. 1.5c). Density functional theory calculations reveal that the degree of the spin polarization depends systematically on the strength of the bonding between the molecule and the surface. The spin polarization of states near the Fermi level makes the molecule act as a spin filter for electrons.

The SP-STM studies of this kind are nicely complemented by X-ray magnetic circular dichroism (XMCD) measurements. This is a spatial averaging technique that allows accessing the local magnetic properties of the system, unlike SP-STM which senses the spin-polarization of the conductance. There has been a growing activity in this area over the past years [43] and marking results have been recently obtained [44, 45].

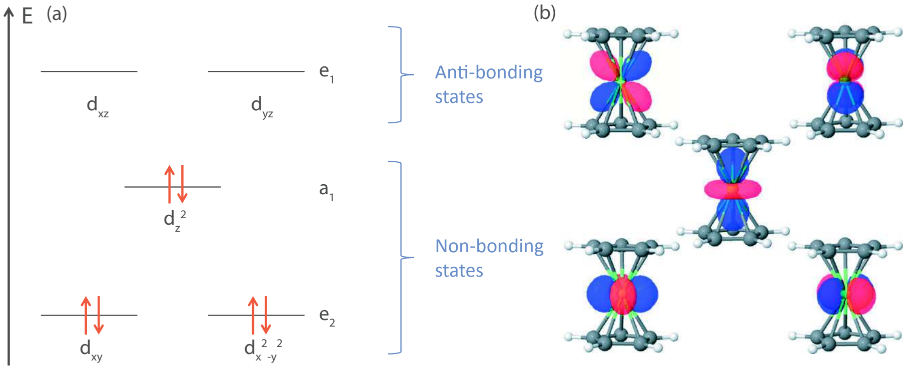

Figure 1.7: **Electronic configuration of ferrocene.** (a) Molecular orbitals of ferrocene, adapted from [46]. Only the states with the highest energy are shown, the bonding states are not represented. (b) Corresponding representation of the 3*d* orbitals [47].

1.3 Metallocenes

This thesis is devoted to the first extended investigation of metallocenes on metal surfaces. In their most common version, metallocenes are relatively simple molecules as they are composed by one of the six elements in the middle of the 3*d* row (V, Cr, Mn, Fe, Co, Ni) sandwiched between two cyclopentadienyl rings (C_5H_5, noted Cp hereafter; see Fig. 1.6a for the molecular structure). This makes them small compared to, for example, phthalocyanines as they posses 21 atoms against 57 for CoPc. Despite minor size differences due to bond lengths, all metallocenes have a similar geometry. In Table 1.1 we compare the bond lengths for the two metallocenes investigated in this thesis, ferrocene ($FeCp_2$) and nickelocene ($NiCp_2$). The Cp rings can be found in two different configurations (Fig. 1.6d). The first one, called eclipsed, consists in having the two rings parallel with the hydrogen bonds facing each other. In the case of a staggered configuration, the rings are parallel but an angle of 36 degrees exists between facing hydrogen bonds. The staggered configuration is the most stable in the gas phase.

In general, each Cp ring captures one electron from the transition atom. Ferrocene has a closed $(e_2)^4(a_1)^2$ shell and is non magnetic (Fig. 1.7), while nickelocene, due to the d^8 configuration of nickel results in an open valence shell of $(e_2)^4(a_1)^2(e_1)^2$ (Fig. 1.8), which endows the molecule with a magnetic moment of $2\mu_B$. This open valence shell makes nickelocene chemically more reactive than ferrocene. More generally, for the metallocene family, as the two 4*s* electrons are captured by the two Cp rings, the 3*d* valence electron configurations for VCp_2, $CrCp_2$, $MnCp_2$, $FeCp_2$, $CoCp_2$, and $NiCp_2$ yield a magnetic moment of 3, 2, 1, 0, 1, and 2 μ_B, respectively. The energy gap between the $a1$ and the $e2$

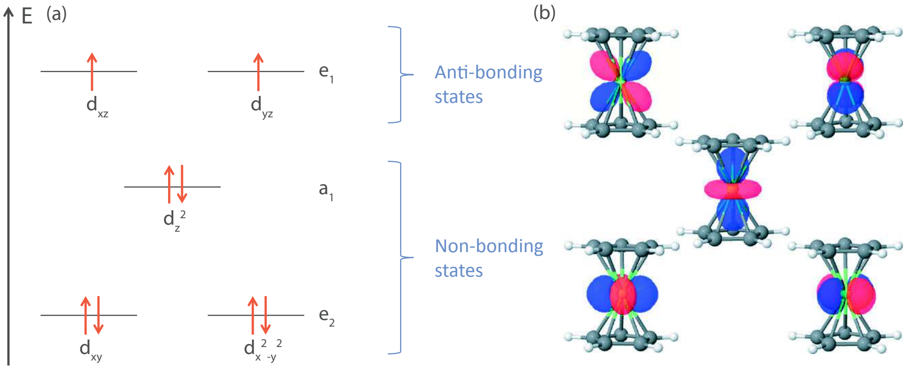

Figure 1.8: **Electronic configuration of nickelocene.** (a) Molecular orbitals of nickelocene, adapted from [46]. Only the states with the highest energy are shown, the bonding states are not represented. (b) Corresponding representation of the 3*d* orbitals [47].

molecular orbitals is always small, whereas the gap between $e1$ and $e2$ is too large to allow for a high-spin configuration.

So why are metallocenes so appealing to molecular spintronics? If experimental data are still lacking, there is a wealth of first-principle studies available in literature. This is not surprising in view of their "simple" molecular structure, which makes them the ideal system for testing new spintronic concepts. Theoretical studies have shown consistently that some metallocenes are half-metallic ferromagnets [48]. In other words, they can exhibit a 100% spin filtering effect over a wide energy range around the Fermi level [48, 2, 49–51]. When these molecules are coupled to ferromagnetic electrodes, the ballistic transport can be characterized by a sizeable transmission for one of the spin channels and a negligibly small transmission for the other, thereby producing a nearly ideal molecular spin valve around the Fermi level (Fig 1.9). Similar predictions have also been made for related systems comprising benzene rings [52, 53]. The spin filtering efficiency is influenced by intrinsic parameters of the molecule, such as its metallic constituents (Fe, V, Co, Cr, ...) [2, 54] or its length [55], but also by extrinsic parameters such as the geometry of the metal-molecule contact [48] or the electrode material [55]. As an example, we recall in Tab. 1.2 some typical values of the computed spin polarization for different metallocene-based wires. Aside spin filtering effects, several other functionalities have also been predicted, such as spin reversal where the spin-polarized direction of the current is controlled through the applied bias without resorting to a magnetic field [56]. Negative differential conductance has also been predicted [48, 56], which is central to several electronic components, including Esaki diodes, and is of particular interest to molecular electronics.

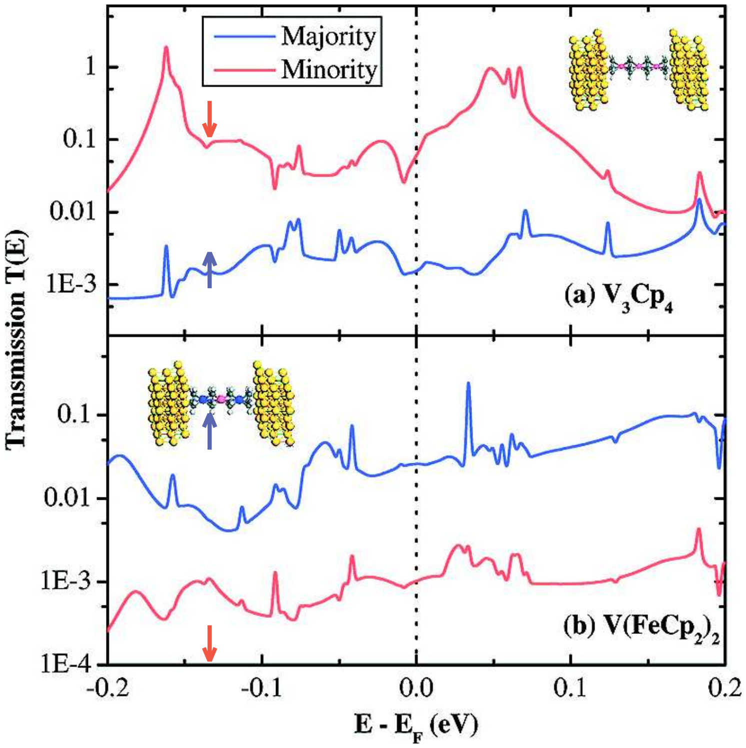

Figure 1.9: **Spin-polarized transmission of metallocene wires.** (a) Majority (↑) and minority (↓) transmissions for a V_3Cp_4 wire between two gold electrodes, resulting in a spin polarization $(T_{\uparrow} - T_{\downarrow})/(T_{\uparrow} + T_{\downarrow}) = -90\%$ at the Fermi level, (b) Majority and minority transmissions for a $V(FeCp_2)_2$ wire between two gold electrodes, resulting in a spin polarization of 85% at the Fermi level. Note the logscale for the transmission. Adapted from [2].

Molecule	$FeCp_2$	Fe_2Cp_2	Fe_3Cp_2	$NiCp_2$	Ni_2Cp_2	Ni_3Cp_2
Transmission spin-polarization	30	96	71	96	18	0

Table 1.2: **Computed transmission spin-polarizations between two metal electrodes for metallocene based chains**, based on [48] and [50].

Despite all these promising theoretical results, experimental studies of this kind on single metallocenes remain limited due to the difficulties in synthesising these molecules in the correct molecular-device environment. The demand for elaborating a prototypical metallocene-based system with atomic-scale control is therefore strong. The work carried out in my thesis is part of a larger project (Fig. 1.10). The project aims at building a metallocene into a ferromagnetic environment and to use a magnetic STM tip to produce the first metallocene based molecular spin valve (Fig. 1.10a-b) with ideal spin filtering efficiency. Prior to this goal, however, it is essential to carefully map the properties of metallocenes in a non magnetic environment (Fig. 1.10c-d). We explored the properties of metallocenes, from their adsorption on noble metal surfaces to their magnetic properties, by using a low temperature STM to gather precise information about the binding properties of metallocene molecules to metal surfaces and characterize their electronic and magnetic properties. X-ray magnetic circular dichroism measurements were also carried out independently to carefully characterize the magnetic status of the molecules. Given the microscopic control exerted with STM, the experimental data collected was highly amenable to theory. This work greatly benefited from the collaborations with the theory groups of M.-L. Bocquet (ENS-Paris) and of N. Lorente (DIPC, San-Sebastián)– who carried out density functional theory calculations and transport calculations to identify the key spintronic properties of these molecules. This manuscript is structured in four chapters:

Chapter 2 will be devoted to the working principle of a STM. We first introduce the tunneling effect within the WKB approximation. We then present the imaging principle and the experimental setup used. The second half of the chapter is dedicated to tunneling spectroscopy, starting with the theory behind it. We will put some emphasis on the various broadening sources of the spectra and present the modifications we applied to the commercial system to minimize the broadening.

Chapter 3 will focus on the detection of inelastic electron scattering in tunneling spectroscopy. We first show how inelastic scattering allows gathering precious information on the magnetic properties of single adsorbates. The second part of the chapter is devoted to the Kondo effect, which instead involves elastic scattering events. We also recall some common aspects between magnetic inelastic scattering and Kondo physics.

Chapter 4 will present the results we obtained with the ferrocene molecule. First, we present the adsorption of ferrocene on copper crystals, describing a new adsorption geometry matching both experimental (STM) and theoretical (DFT-based computations) results. The second part of the chapter is dedicated to the spin doping of a ferrocene molecule with a cobalt atom. We will show how it is possible to produce on the surface a new magnetic cobalt-ferrocene molecule.

Chapter 5 is devoted to nickelocene. As for ferrocene, we characterized its adsorption geometry on copper samples using both STM and DFT computations. We then used inelastic electron tunneling spectroscopy (IETS) and XMCD to characterize its on-surface magnetic properties. We show that the magnetic anisotropy of nickelocene makes it a prototypical

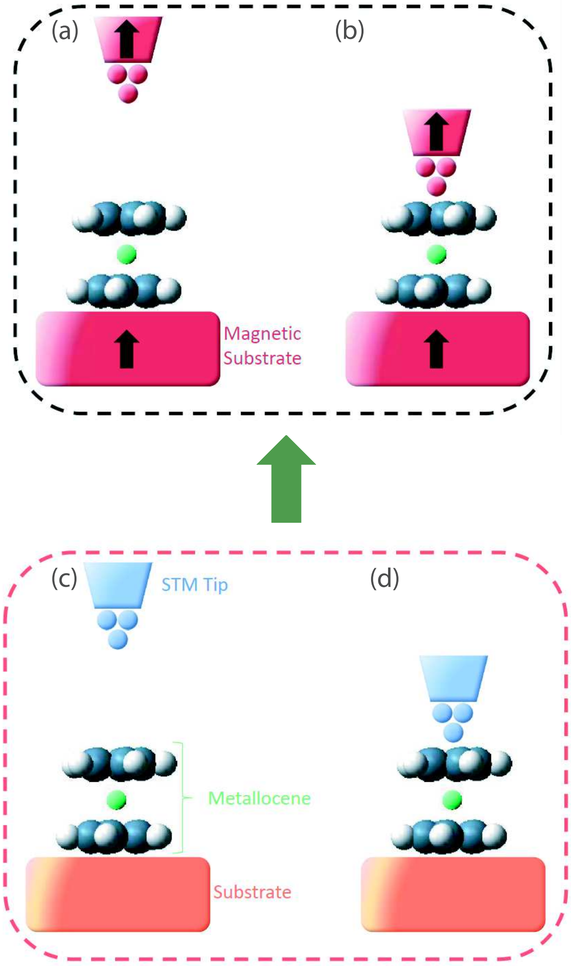

Figure 1.10: **Transport properties of a single metallocene.** Before addressing the spin transport across metallocenes, either in the tunneling regime (a) or in the contact regime (b), we first started by mapping their properties in a non magnetic environnement (c-d).

system where to study the manipulation of a molecular spin via the tunneling current.

Chapter 2

Scanning Tunneling Microscopy

Invented in 1981 [57–59], the Scanning Tunneling Microscope (STM) is today a widely used tool in surface science. Its inventors received the Nobel Prize in 1986 to reward the major advances it brought in the real-space study of surfaces. It belongs to the family of scanning probe microscopes and enables the investigation of nanoscale objects by a topographic and spectroscopic analysis.

The principle of measurement consists in having a metallic tip placed at a distance of a few hundred picometers from the sample surface and collecting an electric current during a scan. The tip and sample act as two electrodes separated by a vacuum-tunneling barrier. By applying a bias, it is possible to shift upward or downward the Fermi energy of one of the electrodes and enable a current to flow (Fig. 2.1). When a negative bias (eV, where e is the charge of the electron and V the bias) is applied to the sample, the occupied states of the tip (grounded) can provide electrons for tunneling to the unoccupied states of the sample (Fig. 2.1a). In the case of a positive bias, electrons tunnel instead from an occupied states of the sample into the unoccupied states of the tip (Fig. 2.1b).

This chapter will be devoted to the working principle of STM, from imaging principle to spectroscopy measurements. Some practical points are also presented, such as the ultra-high vaccum and cryogenics setups used, and precision measurements defining the spectroscopy resolution.

2.1 STM Theory

Tunneling regime

The tunneling process between two electrodes can be described using different models. Here, we present the Wentzel Kramers Brillouin (WKB) [60–62] theory, which relies on

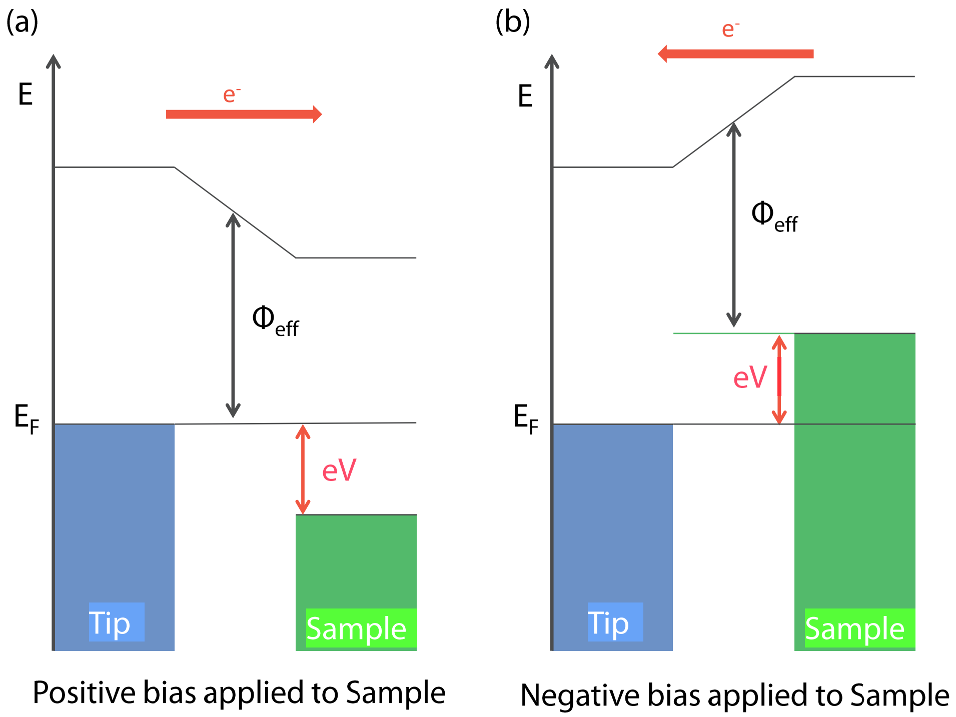

Figure 2.1: **Sketch of a tunneling junction.** (a) shows the case of a positive bias whereas (b) shows the case of a negative bias applied to the sample. ϕ_{eff} stands for the average work function. The energy is expressed with respect to the Fermi level of the system E_F.

a semi-classical approximation. The WKB theory expresses the current through a tunnel junction as

$$I(z,V) \propto \int_{-\infty}^{\infty} T(z,E,V)[f(E-eV)-f(E)]\rho_t(E-eV)\rho_s(E)dE, \tag{2.1}$$

where f is the Fermi-Dirac distribution, ρ_t and ρ_s are the densities of state of the tip and the sample, respectively, and z denotes the tip-sample distance. The transmission coefficient T depends on the shape of the tunneling barrier. A good approximation for the tunneling barrier is a trapezoidal shape [63–65] (Fig. 2.1). This shape leads to the following expression:

$$T(E,z,V) \propto exp[-kz\sqrt{\phi_{eff}+\frac{eV}{2}-(E-E_{\parallel})}], \tag{2.2}$$

with $k = 1.025^{-1}eV^{-1/2}\mathring{A}^{-1}$ and ϕ_{eff} is the average work function of the sample and the tip. The energy $E_{\parallel}$ is the kinetic energy component which is parallel to the junction interface and does not play an important role in the tunneling process as electrons mainly tunnel with a

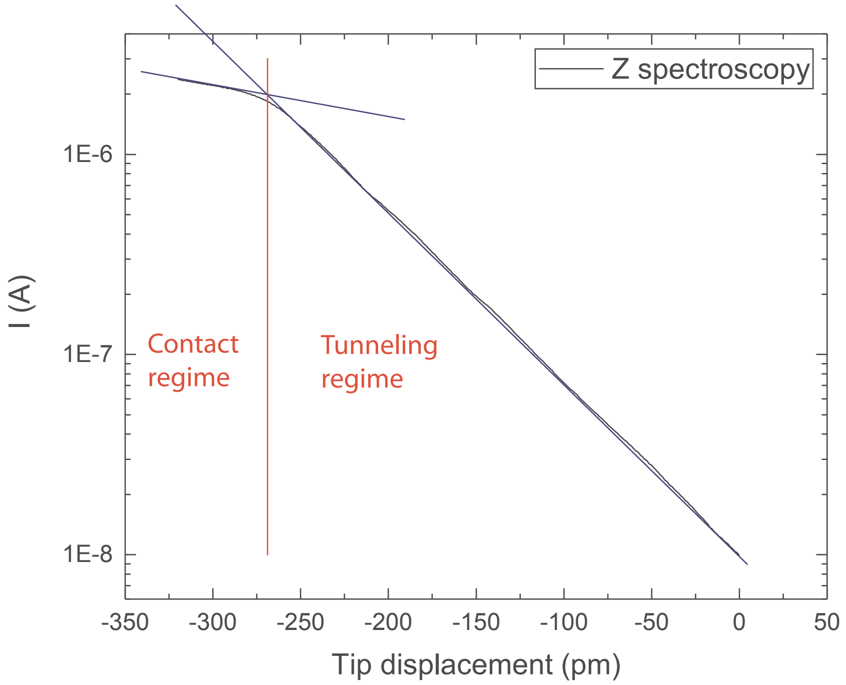

Figure 2.2: $I(z)$ **spectrum above Cu(100).** Current (I) recorded above a copper atom on Cu(100) for a bias of -30 mV with respect to a tip displacement (z). The contact with the atom is reached around 270 pm as shown by the change in the slope of the current. The tip displacement is expressed with negative values when the tip goes from its regulated position towards the surface.

momentum perpendicular to the surface. Typically, $\phi_{eff} \simeq 4\ eV$ for metals, so T imposes a change by a factor 10 in current per Angström.

Contacting the sample with the tip

The exponential behaviour of the tunneling current with respect to the tip-sample distance can be evidenced through a so-called I versus z measurement. To perform such an experiment, one must monitor the intensity of the tunneling current with respect to the tip displacement. To illustrate this, we present an $I(z)$ spectrum that was recorded above a Cu adatom on Cu(100) with a copper-terminated tip (Fig. 2.2). The exponential dependency of the current with respect to the tip/sample distance, (Eq.2.2), is clearly visible below a current in the µA range. Above this threshold, the slope of the I(z) curve changes indicating that the contact regime is reached. Through a geometrical construction (dashed lines in Fig. 2.2) we deduce a contact current of 2.0 µA, which corresponds to a contact conductance (data recorded with a fixed bias of -30 mV) of $0.86 \times 2e^2/h$. The value close to $2e^2/h$, which defines the quantum of conductance, can be explained within the framework of the Landauer theory [66–71]. Assuming that the electrons in the electrodes are behaving as a 1D free electron gas in an ideal square potential and that the tunneling current has a ballistic behaviour, the conductane is expressed as

$$G = \frac{I_t}{V} = \frac{2e^2}{h} \sum_{i,j=1}^{n} |\tau_{i,j}|^2 \tag{2.3}$$

where $|\tau_{i,j}|^2$ refers to the transmission probability for electrons coming from conductance channel i and going through channel j. For noble metal atoms where there is a unique channel that corresponds to a s valence orbital, we have $G \simeq 2e^2/h$. Contact measurements to single atoms such as Cu, Ag or Au can thus be used during experiments to check the metallic character of the tip [72, 73].

2.2 STM working principle

2.2.1 Imaging principle

The WKB theory provides a first model exhibiting an exponential dependency of the current with respect to the distance betwen the tip and the sample. This exponential dependency is the key point for the STM imaging process. Scanning all the sample surface at a distance z (few hundreds of picometers) and collecting point by point the current gives a precise measurement of the surface corrugation below the tip (Fig. 2.3a). This mode is called the constant-height measurement. One can expect that scanning a sample with this mode may lead to a crash of the tip when the corrugation becomes very high. To overcome this limitation, a feedback loop is used in order to change the tip-sample distance after collecting the current (Fig. 2.3b). Thus, the user can scan the sample surface with a given current and when the tip encounters an impurity, the feedback loop retracts the tip in order to keep the current constant. This is the so-called constant-current scanning mode. These z corrections in the tip sample distance are then recorded and used to reconstruct a topographic image of the surface (Fig. 2.4).

The tip position is controlled using piezo ceramics. A first group of piezos is responsible for the so-called coarse-motion and can move the tip by 100 nm when a voltage pulse is applied (usually between 150 V and 400 V). These piezo-elements are therefore used to bring

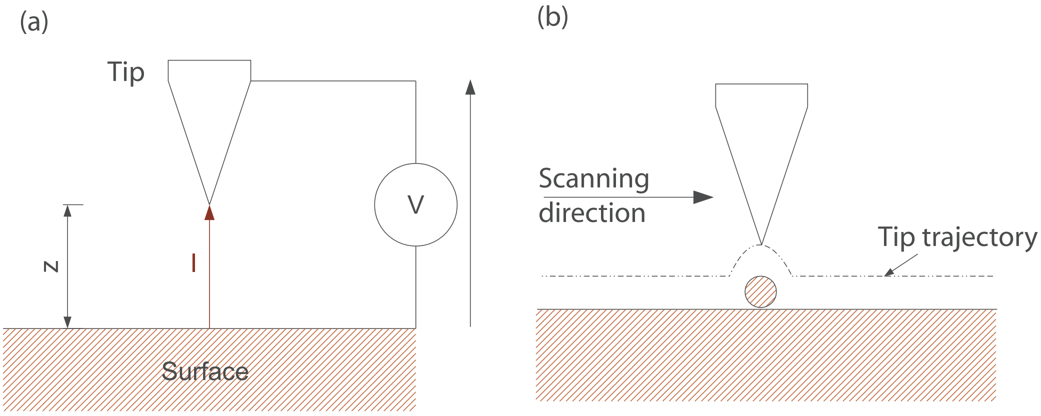

Figure 2.3: **STM working principle.** (a) Tunneling current collected by the tip above a sample surface. (b) Constant-current scanning mode. Scheme adapted from [74].

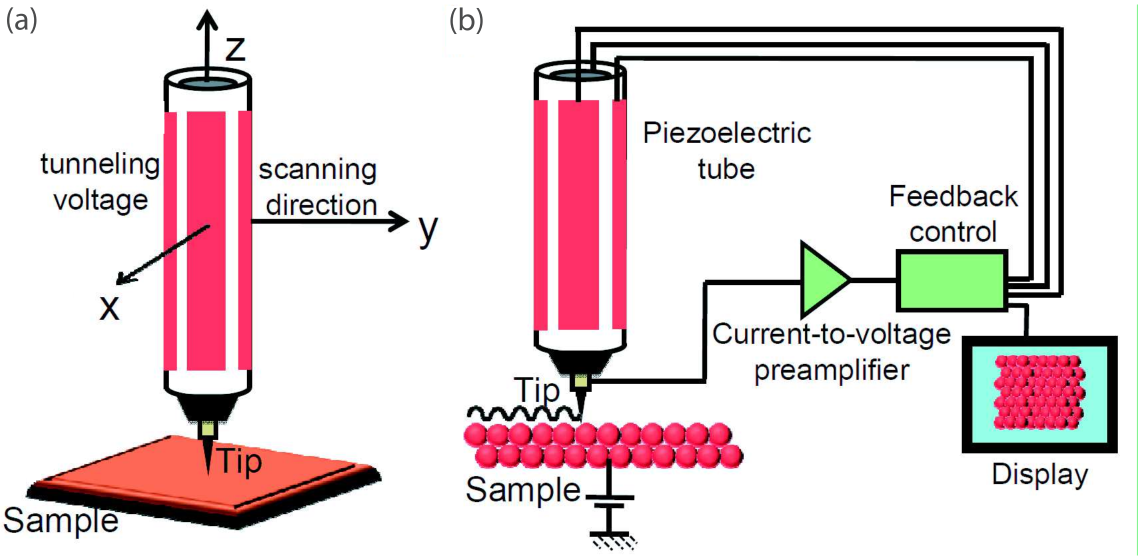

Figure 2.4: **STM tip control.** (a) Sketch of the tip displacement and piezoelectric tube. (b) Sketch of the feedback loop enabling the constant-current scanning, taken from [75].

the tip within tunneling distance from the surface. A piezoelectric tube (Fig. 2.4) enables to scan a small area of the sample surface, usually a square of 200 μm long side.

The calibration of the piezo component can be achieved using a well-known crystal. In our case,we used the step height of Cu(100) to calibrate the Z axis of the piezo ceramic. We then calibrated the X and Y axes giving atomic resolution by scanning the surface with the tip in contact [76] (Fig. 2.5).

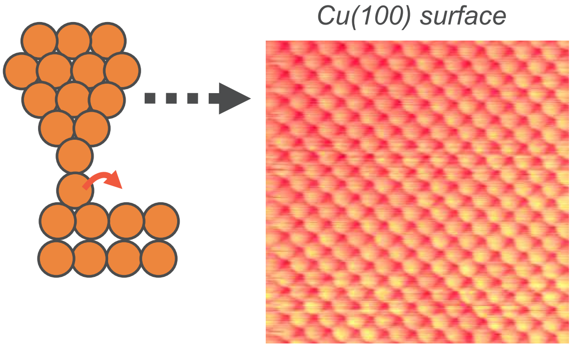

Figure 2.5: **Contact scan of a Cu(100) surface.** The crystal structure of copper appears in the STM image (50 mV, 8nA, 5×5 nm^2.

2.2.2 Experimental setup

The STM we are using is a modified Omicron low temperature STM. The whole system includes a STM chamber (Fig. 2.6a); a preparation chamber (Fig. 2.6b-c); a load-lock introduction chamber and different pumping stages. All chambers are separated by gate valves in order to isolate them from each other during sample preparation. The base pressure is on the order of 10^{-10} mbar. According to the Hertz-Knudsen formula [77], the amount of impurities increases with a rate of 1 monolayer per 10^6 seconds, meaning that we can idealy keep the sample clean for a few weeks. Such a low pressure range is reached thanks to different pumping stages. The primary stage consists in a scroll pump working from atmosphere pressure down to 10^{-2} mbar. The secondary stage comprises a turbomolecular pump lowering the pressure to 10^{-10} mbar. During the measurements, these pumps are stopped and the vacuum is maintained by ionic pumps.

We use single-metallic crystals as samples, in particular Cu(100) and Cu(111). They are cleaned in the preparation chamber (Fig. 2.6b-4) by repeated cycles of argon sputtering (with a base pressure of 10^{-6} mbar and a voltage of 1500V, (Fig. 2.6b-5) and annealing (around 500°C for copper crystals). They are then transfered to the STM chamber (Fig. 2.6a-1) thanks to several transfer rods. The STM tips are made of a tungsten wire with a purity of 99%. The wire is chemically etched using a NaOH solution. As shown in [66], the curvature radius of the tip obtained with such an etching method is lower than 1 μm.The tips are also cleaned in situ with argon sputtering and annealing around 800°C.

The deposition of metallic species can be done in the preparation chamber through e-beam evaporators (Fig. 2.6c-8). It is also possible to deposit metallic atoms at low temperature (77 K or 4.4 K) directly in the STM chamber thanks to a homemade evaporator (Fig. 2.6a-3). This evaporator consists of a thin noble metal wire placed around a 0.25 mm diameter tungsten

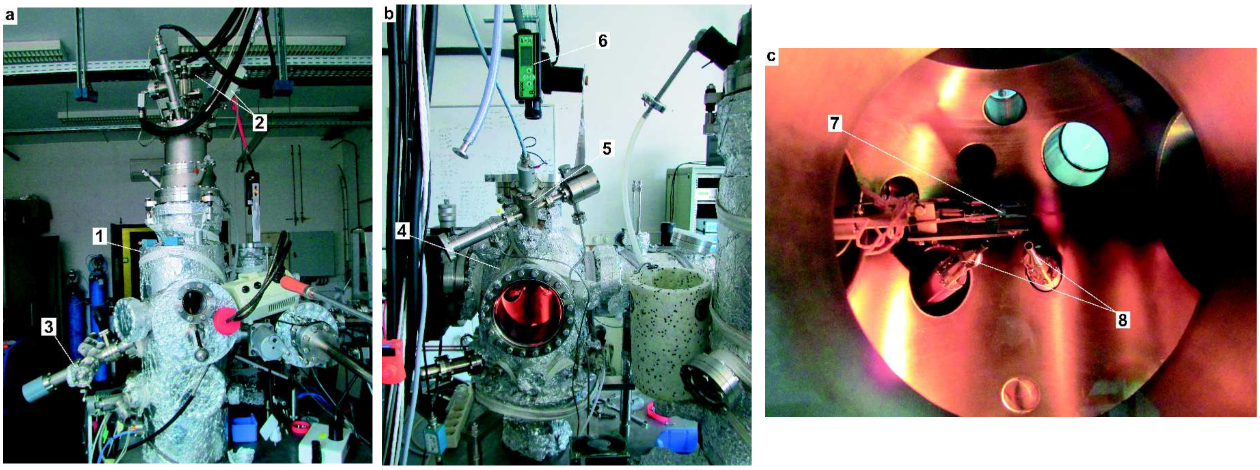

Figure 2.6: **Photos of the experiemental setup.** (a) STM chamber (1) with filtered input and output wires (2) and a homemade evaporator for atom deposition (3). (b) The preparation chamber (4) with the ion gun for sputtering (5) and an optical pyrometer for temperature control (6). (c) View of the manipulator for sample preparation (7) and e-beam evaporators for metallic atoms deposition (8).

wire. A power between 3 and 5 W is sufficient to sublimate the atoms from the metal wire.We use a quartz balance to monitor the flux of the sublimated metallic atoms.

The low temperature is reached thanks to a liquid helium bath. A nitrogen cooled radiation shield surrounds the helium dewar in order to reduce the consumption (Fig. 2.7). The measurement stage is also protected from thermal radiations by two rotative shields coated with gold. We improved the cryogenics by replacing the copper cables by steel ones for both input and output signals, for the piezo ceramics and for the thermocouple measuring the temperature on the sample. The steel cables reduce the heat transfer between the low temperature stage and the upper parts of the cryostat at room temperature. This enables us to reach a temperature of 4.4 K on the sample block and a helium standing time up to 34 hours, which corresponds to an average consumption of 0.1l/hour.

2.3 Spectrocopy

2.3.1 Theory

Standard spectroscopy

The WKB theory shows a dependency of the tunneling current with respect to the bias applied between the tip and the sample. But this bias also shifts the densities of states of one

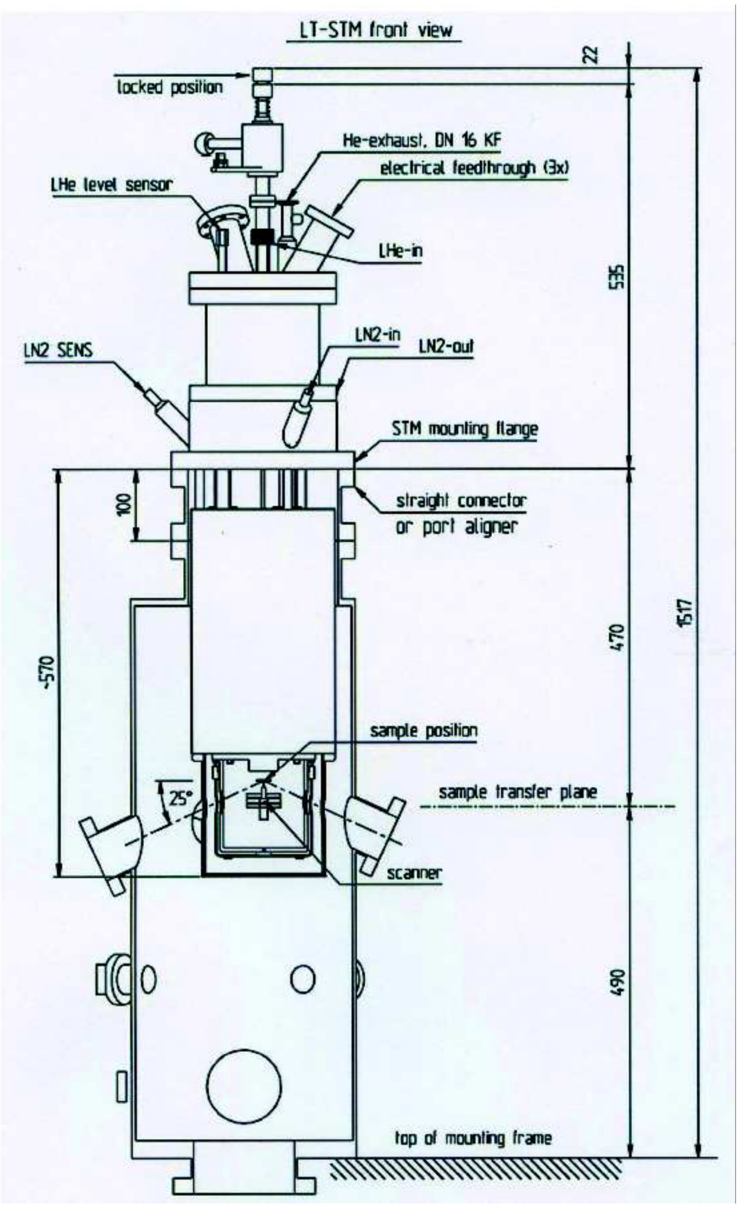

Figure 2.7: **Original schematics of the Omicron LT STM.**

electrode with respect to the other. This means that there is a way to investigate the local densities of states of the sample by measuring the tunneling current at different biases. This operation is called Scanning Tunneling Spectroscopy, or STS, and has to be carried out at a given sample distance, i. e. without the feedback loop operating. From Eq. 2.2, we know that the tip and the sample DOS equally contribute to the tunneling current as one can interchange ρ_S and ρ_T, and vice versa. Here, we assume that the tip DOS is flat around Fermi level, that is to say $\rho_T = C^{ste}$. At our working temperature, we use a step function to approximate the

Fermi-Dirac distribution, leading to a simplified expression of the current in which the Fermi level is used as the energy reference ($E_F = 0$):

$$\frac{dI}{dV}(z,V) \propto T(z,E=V,V)\rho_S(V) + \int_0^V \rho_s(E)\frac{dT(z,E,V)}{dV}dE. \tag{2.4}$$

By using the expression of the transmission coefficient (Eq. 2.2), we have :

$$\sigma \propto \rho_s(V)T(z,V,V) - \frac{\phi_{eff}}{4z}I(z,V), \tag{2.5}$$

with

$$\sigma \equiv \frac{dI}{dV}, \tag{2.6}$$

where ϕ_{eff} is the average work function as defined before. We can see in this expression that for small tip-sample distances, most of the information of the differential conductance spectrum refers to the sample density of states ρ_s. In the case of low distances (high current), the proportion of information coming from the second term increases and can sometimes lead to a negative differential conductance [78]. Generally speaking however, the second term can be neglected and thus the conductance expression can be written as

$$\sigma \propto \rho_s(V)T(z,V,V). \tag{2.7}$$

This equation shows that $\sigma(V)$ contains information about the sample density of states and is therefore a powerful tool to investigate the electronic properties of surfaces around the Fermi energy with atomic-scale resolution.

Inelastic Electron Tunneling Spectroscopy

Inelastic phenomena occur in STM when the electrons flowing through a system give a part of their energy to excite an adsorbed atom or molecule in the junction. This energy, noted $\hbar\omega$ (Fig. 2.8), can be used to induce spin transitions among Zeeman or vibronic levels, or excite plasmons in the tunneling junction. It leads to an increase of the current for a given bias as soon as the excitation energy threshold is reached. The change in current can be explained as the opening of a new tunneling channel for the electrons.

At each threshold energy, a slope change occurs in the $I(V)$ curve leading to a symmetric step around Fermi level (each step corresponding to an excitation process) in the corresponding $dI/dV(V)$ spectrum. This spectroscopy is defined as Inelastic Electron Tunneling Spectroscopy (IETS). To examplify this, we present in Fig. 2.9 the typical signature of vibrational/rotational excitation of a H_2 layer. The rotational excitation of hydrogen is visible at

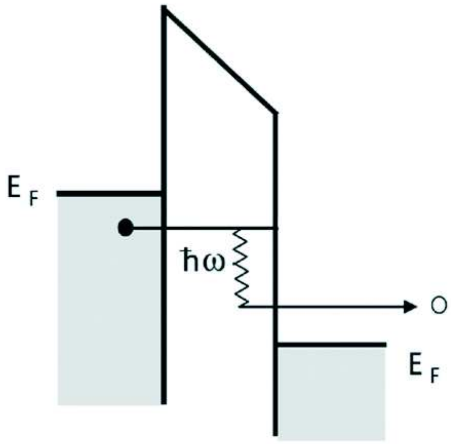

Figure 2.8: **Example of an inelastic process in STM.** Example of an inelastic process in STM. The energy $\hbar\omega$ is lost by the electrons during the inelastic process.

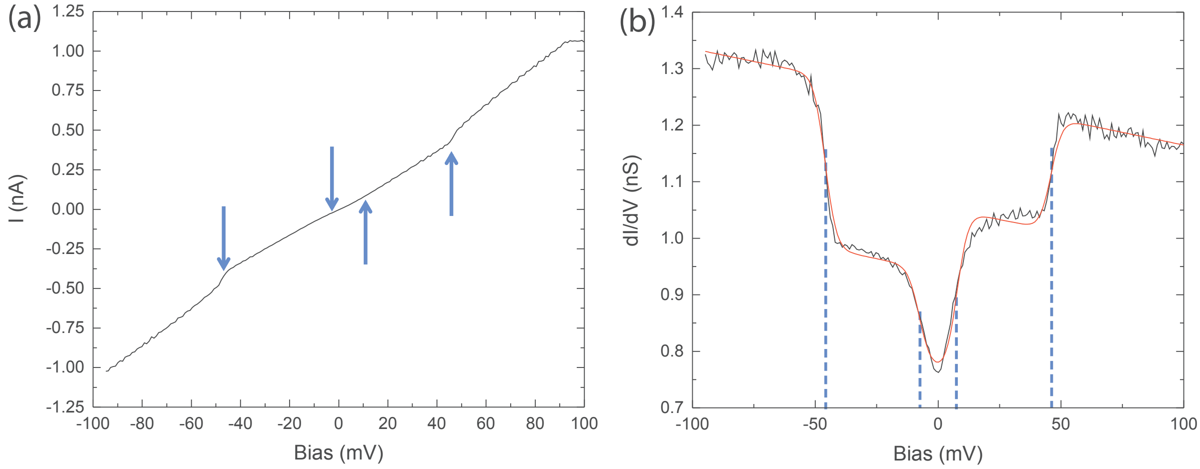

Figure 2.9: **IETS of a hydrogen layer.** (a) shows the slope changes in the current intensity (marked by arrows) and (b) shows the first derivative of the current with respect to bias.

48 meV, while the lower energy excitation (10 meV) can be attributed to a phonon excitation in the layer [79].

2.3.2 Lock-in detection principle

In principle, to record a $dI/dV(V)$ one could numerically derive an $I(V)$ spectrum. This leads to a differential conductance spectrum with a low signal-to-noise ratio (Fig. 2.10). To overcome this limitation, we use a lock-in amplifier. The main idea of the lock-in phase sensitive detector (called lock-in here) is to add a sinusoidal modulation wave to the input

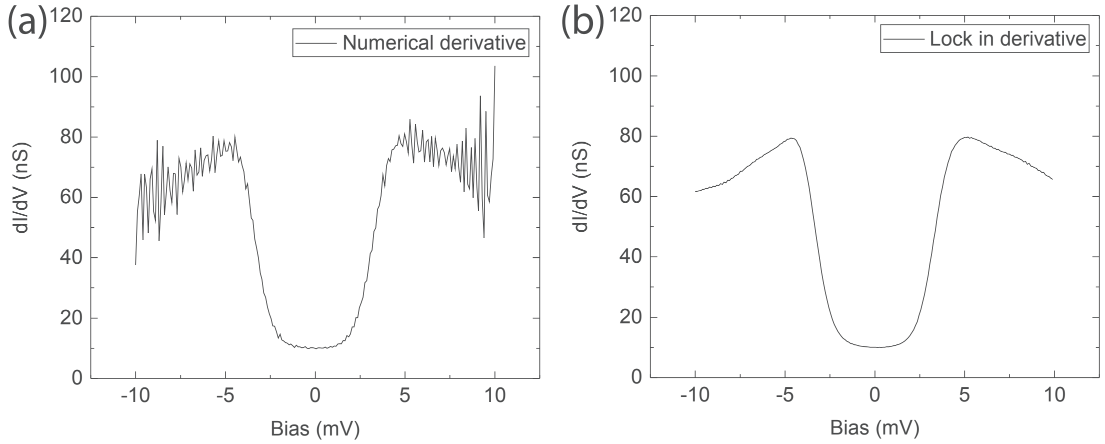

Figure 2.10: **Comparison between the derivation of the $I(V)$ curve and the lock-in recorded conductance $\sigma(V)$.** (a) Numerical derivative of the tunneling current. (b) $\sigma(V)$ obtained through the lock-in technique.

signal of the STM and then deduce the derivative of the output signal (the tunneling current in our case) from the harmonics of the modulation wave. To obtain a result as accurate as possible, the modulation frequency must be selected in a range in which the noise is negligible compared to the signal we are working with.

Formally, we can write the tunneling current as

$$I = I[V + V_m cos(\omega t + \theta)]. \tag{2.8}$$

Using a small enough amplitude V_m for the modulation ($V_m << |V|$), one can Taylor expand the tunneling current entering the lock-in as

$$I[V + V_m cos(\omega t + \theta)] = I(V) + a_1 \frac{dI(V)}{dV} V_m cos(\omega t + \theta) + a_2 \frac{d^2I(V)}{dV^2} V_m cos(2\omega t + \theta) + \dots . \tag{2.9}$$

Using a lock-in amplifier, this signal is multiplied by the phase-shifted modulation signal $V' cos(\omega t + \phi)$ where V' is the constant amplitude of the modulating signal. The first order term of the Taylor expansion becomes

$$\sigma(V)_{lockin} = V' cos(\omega t + \phi) \times \left[a_1 \frac{dI(V)}{dV} V_m cos(\omega t + \theta) \right], \tag{2.10}$$

which can be re-expressed as

$$\sigma(V)_{lockin} = a_1 \frac{V'}{2} \frac{dI(V)}{dV} V_m [cos(\theta - \phi) + cos(2\omega t + \theta + \phi)]. \tag{2.11}$$

By using a low-pass filter, the phase sensitive detector can select only the first term which includes the differential conductance information. Adjusting the phase ϕ , it is possible to maximize the output signal of the lock-in.

In our case, the spectra of interest are located in a bias range $|V| < 5$ mV. In order to satisfy the conditions of the Taylor expansion, we used a modulation amplitude of a few hundreds µV (amplitude taken as Root Mean Square, noted rms). As showed below, such a low amplitude also reduces the broadening of the recorded spectra.

2.3.3 Broadening in spectroscopy

Since the spin-flip excitations are typically of a few meV large (see Chap.3), an accurate control of the broadening mechanism in the tunneling spectra is necessary. Several sources of broadening may be identified as briefly described hereafter. We first treat the case of elastic tunneling (STS), and then of inelastic tunneling (IETS).

Broadening in STS

Temperature induced broadening. The smearing of the Fermi-Dirac distribution causes the $dI/dV(V)$ spectra to broaden with increasing temperature. Recalling Eq. 2.2 and considering T and ρ_{tip} constant, we have

$$\sigma \propto \int_{-\infty}^{\infty} \rho_s \frac{df(E - eV)}{dV} dE, \tag{2.12}$$

that can be rewritten as a convolution product

$$\sigma(V) \propto \rho_S * \chi_T(E - eV), \tag{2.13}$$

where

$$\chi_T(E - eV) = \frac{df}{dV}(E - eV) = \left[\frac{\chi_T(0)}{cosh(\beta \frac{E-eV}{2k_B T})} \right]^2, \tag{2.14}$$

and $\chi_T(0) = \frac{e}{K_B T}$. This broadening function is plotted in Fig. 2.11 (a). The broadening function due to temperature has a Full Width Half Maximum (FWHM) of $\delta_T = 3.5\ k_B T$. In other words, the higher the temperature, the stronger the smearing of the spectrum

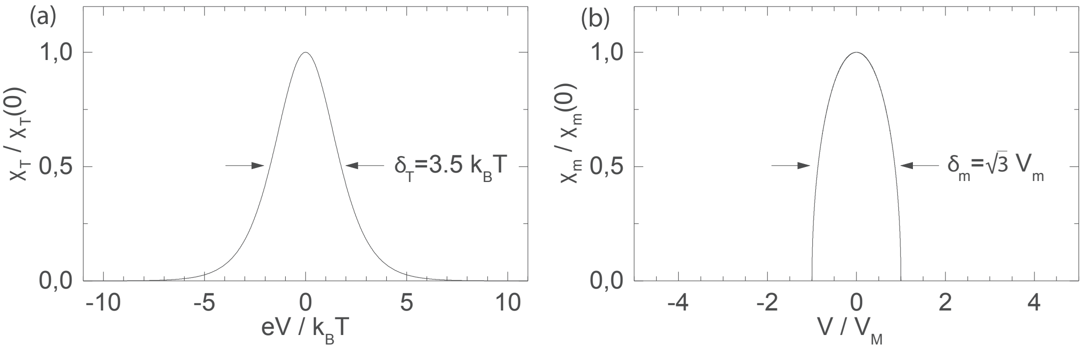

Figure 2.11: **Illustration of the effects of thermal lock-in induced broadening in STS.** (a) Smearing function χ_T. (b) Smearing function χ_M. Adapted from [80].

$$\delta_T = 0.3T \text{ [mV]}. \tag{2.15}$$

To minimize δ_T, we pump on the He bath in order to achieve a working temperature of 2.4 K. For a pressure in the order of 10^{-2} mbar in the helium dewar, this temperature can be kept for approximately 12 hours and the FWHM is then δ_T = 700 µV.

Lock-in broadening. Another source of broadening is the noise present in the signals entering to and exiting from the STM. A major source of noise is the lock-in itself since it introduces a periodic modulation in the bias applied to the junction. This may be rationalized by considering the first harmonic obtained through the lock-in by

$$I_{\omega 1} = \frac{1}{\tau}\int_{-\tau/2}^{\tau/2} I[V + V_M cos(\omega t)]cos(\omega t)dt \tag{2.16}$$

where τ is the measurement interval time. With some mathematical treatments described in [81], the conductance spectrum measured with the lock-in appears as a convolution product :

$$[\sigma(V)]_{lockin} = \int_{-\infty}^{\infty} \frac{dI}{dV}(V - V')\chi_M(V')dV', \tag{2.17}$$

where

$$\chi_M(V') = \frac{2\sqrt{V_M^2 - V'^2}}{\pi V_M^2}, \tag{2.18}$$

is the broadening function of the lock-in signal (Fig. 2.11b). The modulation has then a FWHM of

$$\delta_M = 2.45 V_M \text{ [mV rms]}. \tag{2.19}$$

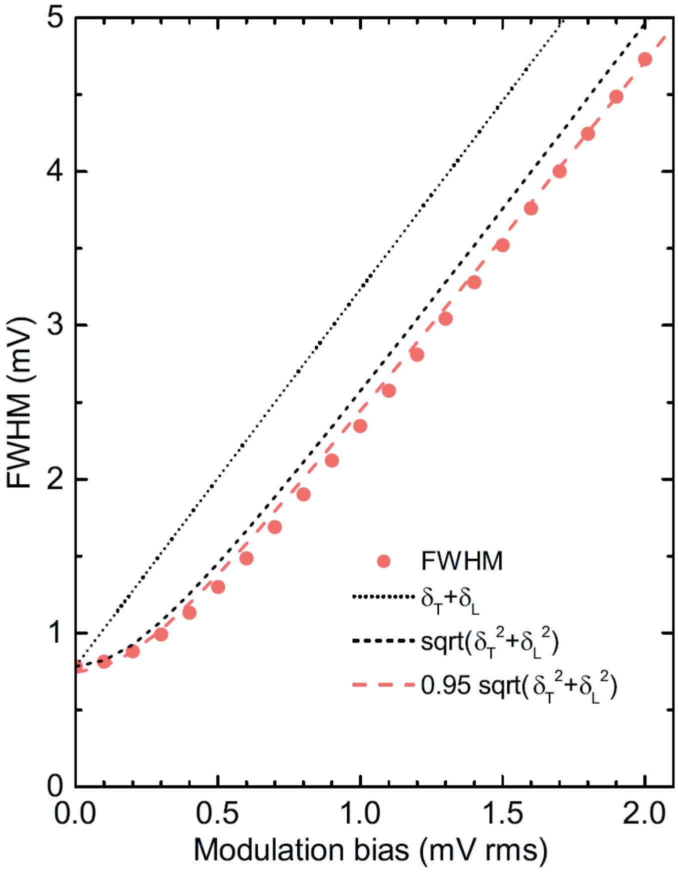

Figure 2.12: **General case smearing function.** FWHM of the smearing function versus modulation bias. Here, both temperature and modulation are taken into account. The temperature for this curve is set at 2.4 K.

General elastic case. When one takes both temperature and modulation broadening into account, the measured signal is

$$\sigma(V)_{measured} \propto \rho_S * \chi_T * \chi_M. \tag{2.20}$$

The computed lineshapes (Fig. 2.12) show that the FWHM of the smearing function $\chi_T * \chi_M$ depends on both δ_T and δ_M and the bias resolution δ_V achieved in the spectra can be approximated as

$$\delta_v \simeq 0.95 \times \sqrt{(\delta_T)^2 + (\delta_M)^2}. \tag{2.21}$$

To obtain a resolution lower than a mV in the spectra, one has to use a modulation amplitude lower than 200 μV rms at a temperature of 2.4 K.

Broadening in IETS

To deal with broadening in IETS, we follow the same approach as above. According to Klein et al., [81], one obtains

$$\delta_T = 0.47T \text{ [mV]}, \tag{2.22}$$

and

$$\delta_M = 1.73V_M \text{ [mV rms]}. \tag{2.23}$$

Our measurements being performed at 2.4 K with a 150 μV rms modulation, we assume that the smearing is carried by the temperature. Then, for simplicity, we only deal with Fermi-Dirac broadening term and thus obtain the following expression for the inelastic current [82] :

$$I_i = C\, e(V - V_0)\frac{e^{e(V-V_0)/k_\mathrm{B}T}}{e^{e(V-V_0)/k_\mathrm{B}T}+1} \tag{2.24}$$

where C is a constant depending on tunneling parameters and here only affects the apparent height of the inelastic step in the differential conductance spectra. V_0 refers to the energy threshold for the inelastic process. This gives a total broadening of $\delta = 1.26$ mV for our measurement at 2.4 K.

High-frequency noise as a source of broadening

Experimentally, we found that the presence of high-frequency (in the order of MHz or higher) noise is also a strong source of broadening. To reduce the impact of this noise, we shielded our cables and installed MHz low-pass filters on all cables entering the STM (piezo controls, thermometer and bias). The gain in precision for our measurements was significant. To evaluate the efficiency of our high-frequency filters, we can compare the inelastic signal of Fe atoms deposited on copper nitride without and with the filters. The inelastic effects that we measure are described in Chap. 3, and the following spectra were taken at 2.4 K with a modulation of 150 μV rms.

In principle, by using a 150 μV modulation at 2.4 K, we should be able to distinguish three inelastic transitions (Fig. 2.13a; see Chapter 3 for details). However, we can see in Fig. 2.13 (b) a signal which is smeared. According to the fit, the noise we have is equivalent to a

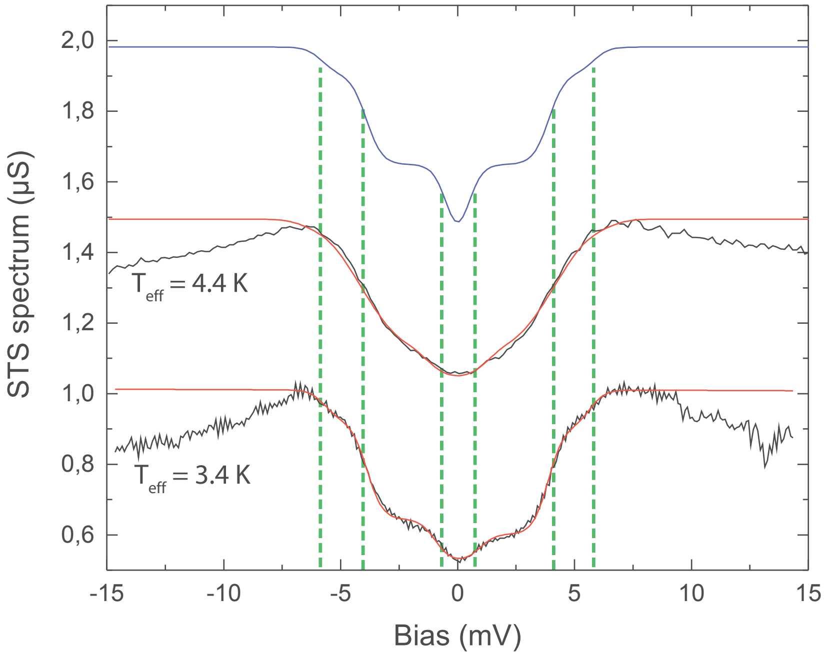

Figure 2.13: **STS spectra taken on the system Fe/Cu$_2$N.** (a) Model spectrum expected with 2.4 K and 150μV rms. (b) Curve obtained before shielding of the measurement stage. Only 2 out of the 3 transitions are identified. The fitted curve (red) indicates an effective temperature of 4.4 K.(c) Spectrum obtained after filtering the high frequency noise. Now the 3 expected transitions are visible, and the fit gives an effective temperature of 3.04 K, closer to the experimental conditions.

temperature of 4.4 K, therefore the spectrum is approximately twice as broad as expected. With the high-frequency filters, 3 transitions can be distinguished instead (Fig. 2.13c) and the effective temperature is 3.04 K.

We compare our resolution with the results published by the group of C. Hirjibehedin [83], who is working with the same base temperature. They studied a system consisting in Co atoms deposited on large (10×10 nm^2) copper nitride islands. For such a system, there is a competition between magnetic anisotropy and Kondo effect. In their study, they show that the closer the Co atom is to the edge of the island, the more intense the Kondo resonnance is, while the magnetic anisotropy decreases concomitantly. In our case, the islands were only few nm^2 large and thus we detect a Kondo resonance at the Fermi energy (Fig. 2.14), flanked by inelastic steps at ±5.5 meV. Interestingly, the width dE of these steps is similar in both sets of data (about 2 meV), indicating a similar resolution for both setups.

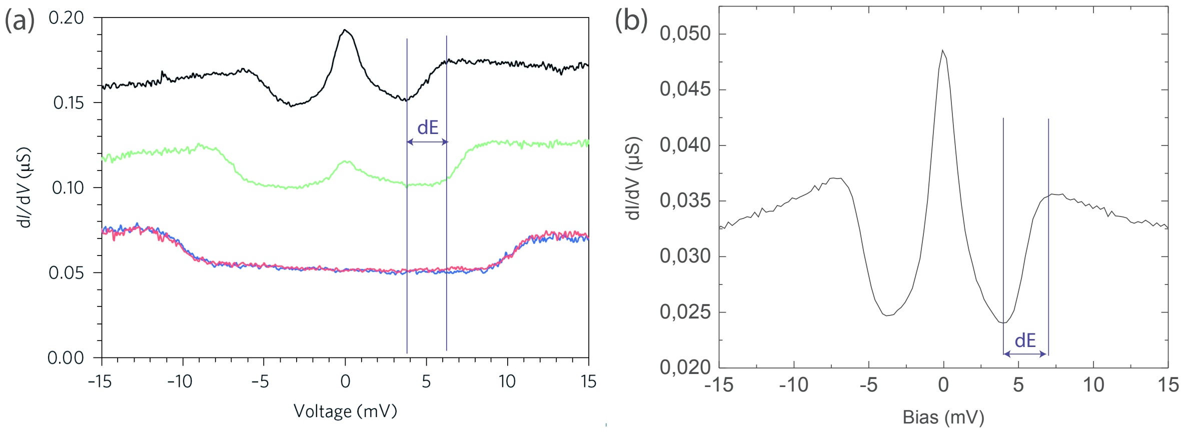

Figure 2.14: **STS spectra taken on the system Co/Cu$_2$N.** (a) Curves presented in [83] for Co/Cu$_2$N. In the case of a cobalt atom located nearby the edge of the Cu$_2$N island (upper black curve), the inelastic step and the kondo resonnance are well defined. (b) Spectra we recorded with our STM at 2.4 K for Co/Cu$_2$N system.

2.3.4 Data treatement : tip structure deconvolution

As shown by the WKB theory, both sample and tip DOS contribute to the tunneling current. ρ_{tip} is usually not constant, and unwanted tip structure can contribute to the dI/dV spectra. We therefore perform a deconvolution process by substracting the normalized tip DOS to the signal as explained in [3]

$$\sigma_{deconv}(V) = \sigma_{measured}(V) - \frac{\sigma_{measured}(0)}{\sigma(0)_{tip}} \times \sigma_{tip}(V) + C \tag{2.25}$$

where $[\sigma(V)]_{measured}$ is the non-treated (bare) spectrum, $\sigma_{tip}(V)$ is the tip structure recorded above the metal crystal and C a constant to shift the deconvoluted spectrum toward the correct (and initial) conductance values. The result of this deconvolution process is presented in Fig. 2.15. This approximated deconvolution works for relatively smooth tip structures compared to the feature of interest in STS. Therefore we are always preparing the tip to have it as flat as possible in the bias range of interest.

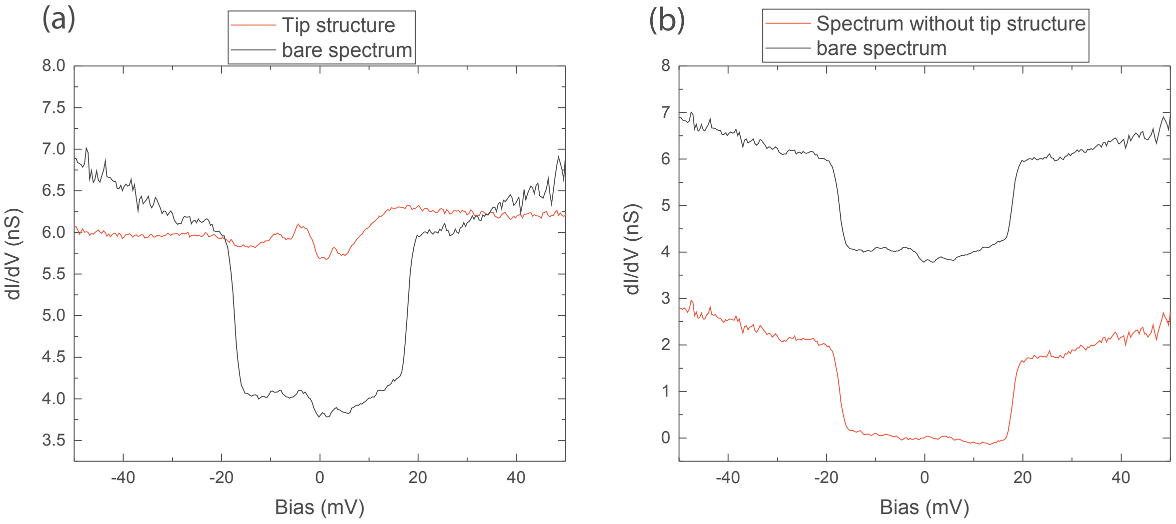

Figure 2.15: **Example of tip structure removal in STS.** (a) Spectrum of the $NiCp_2$ inelastic signal (black curve) and tip structure recorded over a bare Cu(100). (b) Spectrum of $NiCp_2$ inelastic signal (black curve) and same signal with the tip structure removed (red curve), shifted by 4 nS for clarity.

Chapter 3

Detecting spin-flip events with a STM

This chapter is devoted to spin-flip scattering events that are detected in a single impurity using the STM, in particular to scattering events in the presence of magnetic anisotropy. We will be dealing with these scattering events in the following chapter. In the first part, we focus onto inelastic scattering involving spin-flip events, and their detection by magnetic Inelastic Electron Tunneling Spectroscopy (IETS). In the second part, we briefly present the Kondo effect, which instead involves elastic spin-flip scattering. For completeness, we conclude the chapter by mentioning the interplay between inelastic spin-flip events and the Kondo effect.

3.1 Inelastic Electron Tunneling Spectroscopy

In the middle of the last century, physicists started to investigate the inelastic scattering effects in electronic devices. Salaneck *et al.* [84] for instance found that, for conventional conductance measurement at low biases, a periodic feature appeared in the dI/dV acquired across a p-n tunnel junction made up of PbTe(In) and PbTe(In,Ga). The low-bias spectra exhibited zero-bias anomalies having the shape of steps in the dI/dV spectra (fig. 3.1), with a periodic separation. Their analysis led to the conclusion that they were measuring the change in conductance due to the excitation of vibrations of indium and gallium impurities in the insulating layer. Thus, the difference in periodicity of the inelastic features is attributed to the difference in mass of the considered impurities. This finding led to the development of a new type of spectroscopy, inelastic electron tunneling spectroscopy (IETS), that was much exploited from the 70s [85]. IETS consists in a measurable change of the differential conductance due to an excitation of an atom, molecule or atomic structure and it appears as a step-like feature in conductance (dI/dV) spectra.

Soon after the development of STM, surface-science physicists envisioned to use IETS in the tunneling junction of the STM [86, 87]. Compared to macroscopic junctions, STM would

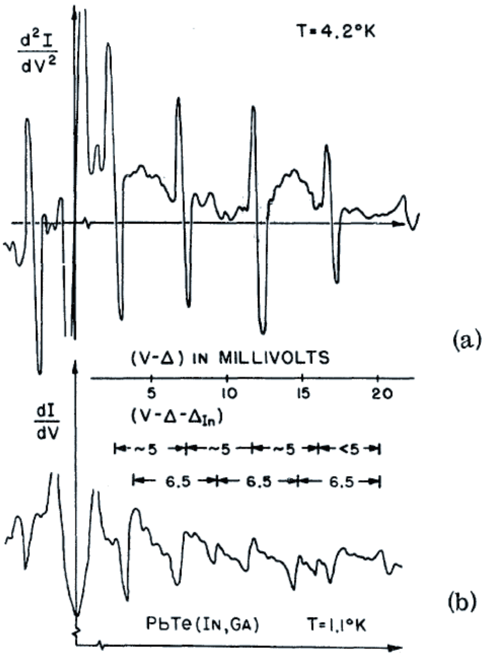

Figure 3.1: **Inelastic spectroscopy recorded in tunnel pn-junctions**, taken from [84]. (a) Second derivative of the tunneling current, d^2I/dV^2, for a PbTe junction doped with In. (b) First derivative, dI/dV, of the current flowing through the pn-junction doped with both In and Ga. The steps related to indium are regularly spaced by 5 meV whereas those induced by gallium are spaced by 6.5 meV.

allow detecting vibrational signatures with atomic scale resolution, thereby opening the path towards single-molecule inelastic spectroscopy. These vibrational signatures would also give a chemical sensitivity to the STM, which is usually absent in standard operating modes of the microscope. The experimental proof only came in 1998 when Stipe *et al.* measured the vibrational IETS of a single acetylene molecule adsorbed on a Cu(100) surface [88–90]. At the end of the 90s, low temperature STM appeared paving the way towards the detection of lower-energy excitations, in particular magnetic excitations involving spin-flip events.

3.1.1 Principle of magnetic IETS

In 2004, Heinrich *et al.* [4] showed that magnetic excitations in a single magnetic atom could be detected using a STM with a built-in magnetic field. This seminal experiment has given rise to a lot of activity in magnetic IETS on the atomic scale. The measurements by Heinrich *et al.* were carried out at 0.6 K on Mn atoms deposited on Al_2O_3 islands (Fig. 3.2a-b). The aluminum oxide layer is used to prevent charge transfer between Mn and the

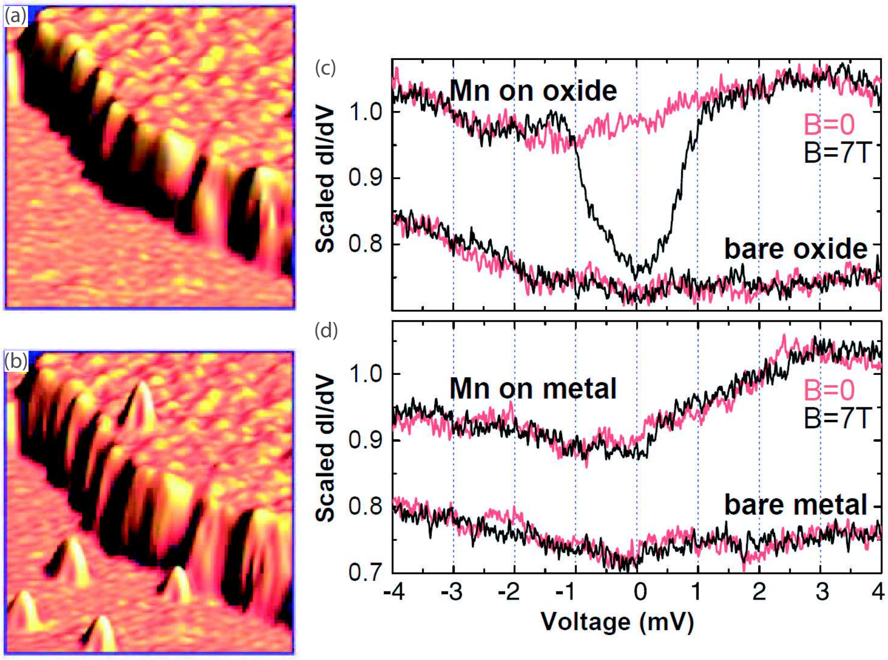

Figure 3.2: **Magnetic IETS of Mn atoms on Al_2O_3.** (a) NiAl(110) surface partially covered with Al_2O_3. (b) Topography of the same area covered with Mn atom. (c) dI/dV spectra obtained on the Mn atom and on the bare oxide with and without the magnetic field. The symmetric feature the around Fermi level only appears on Mn atoms in the presence of a magnetic field. (d) Spectra recorded on the Mn atoms adsorbed on NiAl(110). Fig. extracted from [4].

host metal, *i.e.* to preserve the spin of the Mn atom. This thin insulating layer also effectively separates the Mn atom from the metallic surface leading to a partial decoupling, and thus to longer electronic lifetimes for the Mn states. Experimental identification of these excited states became then easier and better resolved. In the absence of a magnetic field, there is no step-like feature appearing at Fermi level in the dI/dV spectrum. However, when the magnetic field is applied, a symmetric step around the Fermi level appears (Fig. 3.2c). The step corresponds to a 25% increase with respect to the elastic conductance alone, which corresponds to the dI/dV signal at very low bias (0.5 mV).The IETS data of Heinrich *et al.* can be rationalized by assuming the existence of a Zeeman effect for the total momentum $\hat{\mathbf{J}}$ of the Mn atom

$$\mathscr{H}_z = -g\mu_B \hat{\mathbf{J}} \cdot \hat{\mathbf{B}}, \tag{3.1}$$

where g is the gyromagnetic factor, μ_B the Bohr magneton and $\mathbf{B}$ the applied magnetic field. In the case of the Mn atom, the orbital momentum is zero ($3d^5$) and thus the total momentum

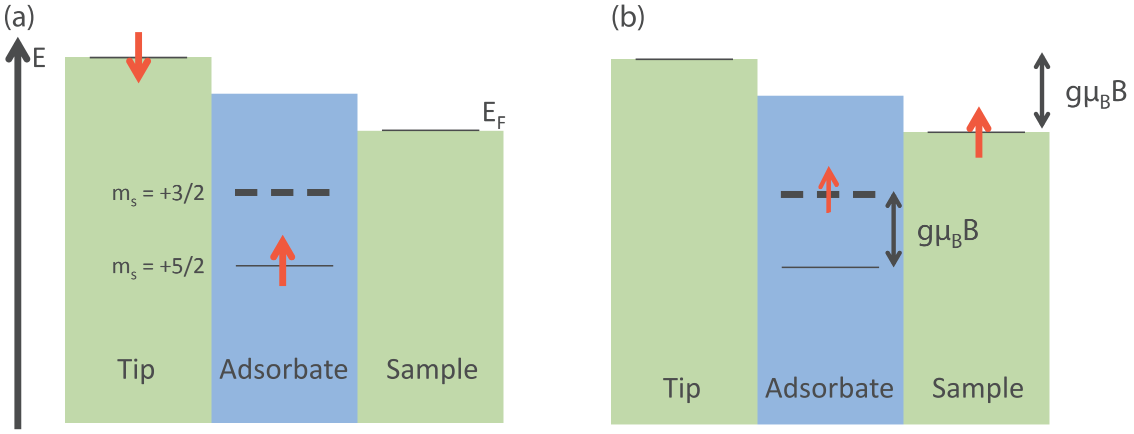

Figure 3.3: **Angular momentum conservation.** (a) Initial state before inelastic excitation of the adsorbate. (b) Final state, the angular momentum of the electron and of the adsorbate change, but the total angular momentum is preserved during the excitation process.

J refers to the spin only, where $S = 5/2$. Supposing this is also the case once the Mn atom is adsorbed on Al_2O_3, when a magnetic field is applied, it is possible to lift the degeneracy of the $S = 5/2$ state, having then $m_S = +5/2$ as the ground state, the $m_S = +3/2$ as the first excited state and so on (Fig. 3.3). Within this viewpoint, the step at 0.7 mV in the dI/dV spectrum corresponds to the $m_S = +5/2 \rightarrow m_S = +3/2$ excitation of a Mn atom. This excitation does not change the total spin of Mn, but the conservation of angular momentum causes the spin of the electron to flip from $m_S = -1/2 \rightarrow m_S = +1/2$, hence the name “spin-flip” spectroscopy that is sometimes used to designate magnetic IETS (Fig. 3.3). Moreover, the spin-flip process of the electron limits the detection to transitions with $\Delta m_S = 0 \pm 1$.

During the very short collisional time between the atom and the tunneling electron, the electron spin couples with the adsorbate spin either through a direct dipolar interaction or through an exchange interaction. The two form a transient collisional intermediate state, whereas the interaction with the environment can be neglected [91, 92]. The efficiency of this process is remarkable compared to vibrational IETS, where the inelastic signal is at most a few per cent of the elastic conductance. The inelastic conductance in magnetic IETS can instead be comparable (Fig. 3.5b) or even exceed (see Chapter 5) the elastic conductance. This behavior can be traced back to the strengths of the interactions at play: while spin-spin coupling is very large, electron-vibration coupling is weak. However, like vibrational IETS, magnetic IETS is very sensitive to the symmetry and to the particular system studied [93], thus not all excited states in a magnetic system can be excited by tunneling electrons. This can also be rationalized in terms of spin-coupling coefficients [91, 94, 95, 92].

3.1.2 Influence of the magnetic anisotropy on IETS Signals

Magnetic anisotropy is a magnetic property coming from the well known spin-orbit coupling phenomenon, favoring a preferential spin orientation in some structures. It has been the focus of research for decades as the bistability it introduces in nanoscale systems is potentially appealing for storing binary information. Recent activity in this domain has consisted in testing whether it is possible to downscale these systems from several nanometers to a single object. Several studies showed encouraging results. First the FePhen molecules [28, 44] exhibit so-called "high spin" and "low spin" states that can be switched by bias application and which survive up to 10 minutes at low temperature. Secondly, metal atoms such as Ho deposited on MgO and magnetically oriented by a strong magnetic field (6.8T) [96] were found to exhibit a long relaxation time, about 1h at 2.5K reduced to 675s ± 77s at 20K because of thermal relaxation processes.

Magnetic anisotropy introduces a small energy difference between two spin orientations called magnetic anisotropy energy (MAE). This weak energy difference, typically of the order of a few meV, renders these spin states accessible to IETS, even in the absence of a magnetic field. Magnetic anisotropy in single objects can be induced by molecular ligands in the case of organometallic compounds [97] (see also Chapter 5) and by structural properties of the substrate as in the case of metal atoms on thin films – MgO or Cu_2N [98, 5, 99]. The Hamiltonian describing the magnetic properties of a single object can be written as

$$\mathscr{H} = \mathscr{H}_c + \mathscr{H}_s + \mathscr{H}_z, \tag{3.2}$$

where $\mathscr{H}_c$ account for the crystal field, $\mathscr{H}_s = \lambda\, \hat{\mathbf{L}}\cdot\hat{\mathbf{S}}$ for the spin-orbit coupling and $\mathscr{H}_z$ for the Zeeman effect. In $3d$ atoms, the crystal-field splitting of the $2L+1$ levels (where L is the orbital quantum number) is much larger than the spin-orbit coupling, leading to the quenching of the orbital angular momentum. It is possible then to treat $\mathscr{H}_s$ as a perturbation of $\mathscr{H}_c$ [100]. In parallel, we can re-write the spin-orbit Hamiltonian as

$$\mathscr{H}_s = D\hat{S}_z^2 + E(\hat{S}_x^2 - \hat{S}_y^2), \tag{3.3}$$

where the axis are taken as presented in Fig. 3.4, the quantization z axis being perpendicular to the sample surface. D expresses the longitudinal anisotropy, which is the tendency of the spin to be aligned along the z axis. A negative value of D will favor a spin parallel to the z axis, whereas a positive value will keep the spin in the xy plane. The parameter E, called transverse anisotropy, accounts for a privileged direction of the spin in the xy plane.

To experimentally illustrate how magnetic anisotropy determines the low-energy spectra revealed by magnetic IETS, we briefly recall the work of Hirjibehedin *et al.* [5] on iron

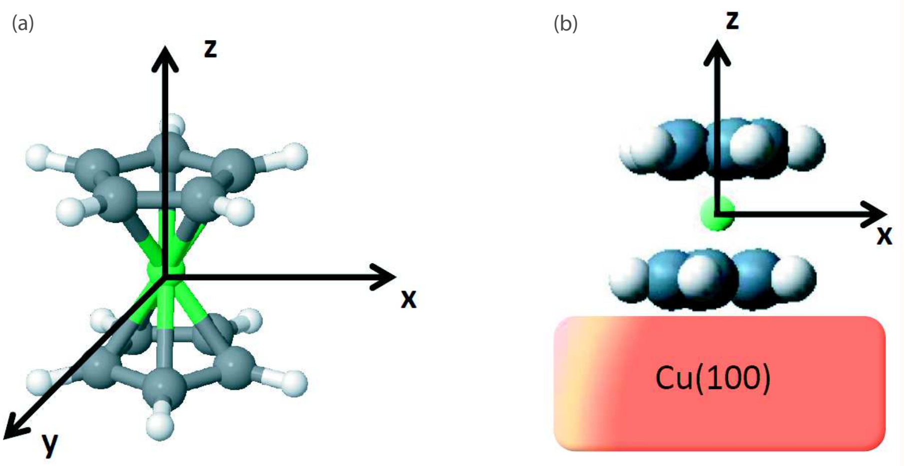

Figure 3.4: **Sketch of X, Y and Z axis on a metallocene.** (a) 3D representation of a single molecule with axis. (b) Geometry of the axis when a molecule is adsorbed on a sample surface.

atoms. In this study, individual Fe atoms are separated from a Cu(100) crystal by a monolayer of copper nitride Cu_2N (Figure 3.5a). The IETS spectra recorded above isolated Fe atoms (Fig. 3.5b) exhibit three transitions, attributed to excitations from the ground state to the different accessible eigenenergies of $\mathscr{H}_s$ (Eq. 3.3). Supposing that the spin of Fe is that of a free iron atom spin, *i.e.* $S=2$, the eigenenergies ε_n of $\mathscr{H}_s$ are

$$\begin{aligned}
\varepsilon_0 &= 2D\,(1+\sqrt{1+3E^2/D^2}),\\
\varepsilon_1 &= 4D,\\
\varepsilon_2 &= (D-3E),\\
\varepsilon_3 &= (D+3E),\\
\varepsilon_4 &= 2D\,(1+\sqrt{1-3E^2/D^2}),
\end{aligned} \tag{3.4}$$

Using these expressions, Hirjibehedin *et al.* extracted D and E, thereby performing the first measurement of magnetic anisotropy at the single-atom level (z axis chosen perpandicular to the sample surface). They found $D=-1.55$ meV and $E=0.31$ meV for Fe. Because of the negative value of D, ε_0 is here the ground state. The robustness of these values was further tested by acquiring IETS at various magnetic fields (Figure 3.5). Note that the shift in energy observed in the IETS steps by application of a magnetic field confirms the magnetic origin of the transitions, excluding a vibronic exitation (insensitive to external magnetic field). Finally,

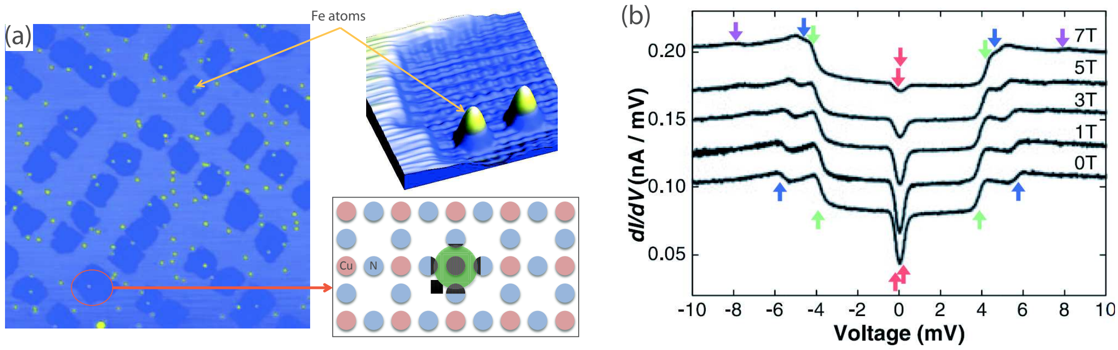

Figure 3.5: **Magnetic IETS of an isolated Fe atom adsorbed on a Cu_2N island** acquired with and without a magnetic field. (a) STM image (65×65 nm^2 of Cu_2N islands on Cu(100) with Fe adatoms. The sketch shows the arrangement of N (blue) and Cu (red) atoms in the islands, the green area being the adsorption site of Fe adatom. (b) Spectra taken with a magnetic field parallel to the nitrogen direction. The spectra were shifted for clarity. The arrows show the three different excitation levels. Figure taken from [5].

the corresponding eigenstates ψ_n can now be fully characterized; they are expressed as a linear combination of the different spin momenta $|S = 2, m_S\rangle$ (Fig. 3.6).

Interestingly, the excitation $\varepsilon_0 \rightarrow \varepsilon_2$ involves essentially transitions from $m_S = \pm 2$ to $m_S = \pm 1$, hence the tunneling electron has to flip its spin to produce the excitation since the Fe spin changes by $\Delta m_S = \pm 1$. Excitations to the first excited level ε_1 remain instead among the $|m_S| = 2$ components. Hence, this transition does not involve a spin-flip of the the tunneling electron ($\Delta m_S = 0$). We can also see from Fig. 3.6 that the direct transition $\varepsilon_0 \rightarrow \varepsilon_4$ is forbidden as the fourth excited state involves essentially a $m_S = 0$ state (in this case we would have $\Delta m_S = \pm 2$). Reaching the state ε_4 could be possible by a double excitation process, but would require higher energies. Hence, only three excitations are detected by IETS. Similarly, when a strong magnetic field is present, the $\varepsilon_0 \rightarrow \varepsilon_2$ transition is forbidden as the ground state involves essentially the $m_S = -2$ component, while the excited state involves essentially the $m_S = 2$ component; accordingly, the transition disappears in the IETS spectrum with increasing magnetic field. These findings clearly show that the mixture of spin states by the anisotropies imposes a specific selection rule for the spin excitations.

By analogy with neutron scattering, if one defines ψ_i and ψ_f as respectively the initial and final eigenstates (Fig. 3.6), the relative IETS step heights for the above transitions was found to be well described by the expression

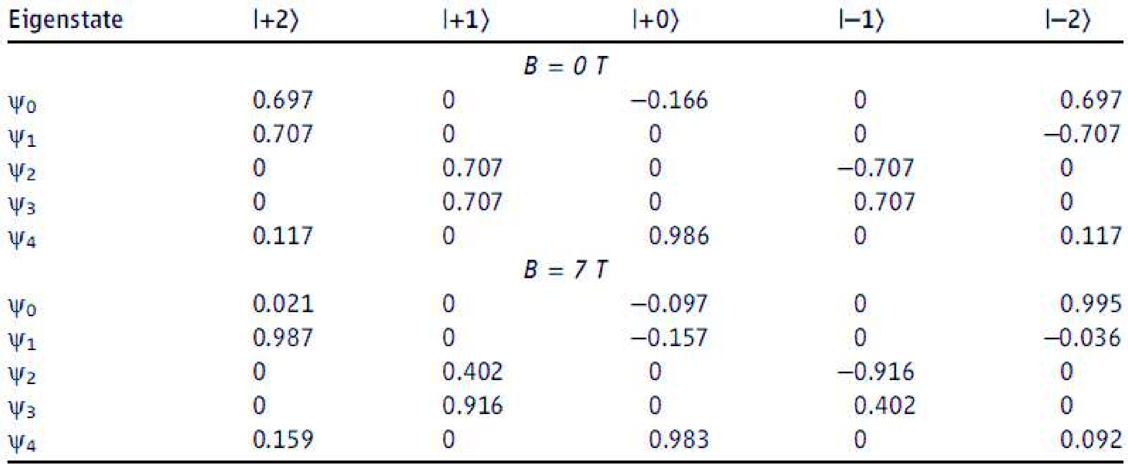

Eigenstate	$\|+2\rangle$	$\|+1\rangle$	$\|+0\rangle$	$\|-1\rangle$	$\|-2\rangle$
			$B = 0\ T$		
ψ_0	0.697	0	−0.166	0	0.697
ψ_1	0.707	0	0	0	−0.707
ψ_2	0	0.707	0	−0.707	0
ψ_3	0	0.707	0	0.707	0
ψ_4	0.117	0	0.986	0	0.117
			$B = 7\ T$		
ψ_0	0.021	0	−0.097	0	0.995
ψ_1	0.987	0	−0.157	0	−0.036
ψ_2	0	0.402	0	−0.916	0
ψ_3	0	0.916	0	0.402	0
ψ_4	0.159	0	0.983	0	0.092

Figure 3.6: **Eigenstates of the spin Hamiltonian for Fe on Cu$_2$N** with $B = 0$ T and at $B = 7$ T. The eigenstates ψ_n are a linear combination of the $|S = 2, m_S\rangle$ states. In the presence of a magnetic field, the Hamiltonian is $\mathscr{H}_s + \mathscr{H}_z$. Taken from [5].

$$
\begin{aligned}
I_{i\to f} &= |\langle\psi_f|\hat{S}_x|\psi_i\rangle|^2 + |\langle\psi_f|\hat{S}_y|\psi_i\rangle|^2 + |\langle\psi_f|\hat{S}_z|\psi_i\rangle|^2 \\
&= \frac{1}{2}|\langle\psi_f|\hat{S}_+|\psi_i\rangle|^2 + \frac{1}{2}|\langle\psi_f|\hat{S}_-|\psi_i\rangle|^2 + |\langle\psi_f|\hat{S}_z|\psi_i\rangle|^2
\end{aligned}
\tag{3.5}
$$

In the zero-field experiment, this yields $I_{0\to1} = 3.88$, $I_{0\to2} = 1.62$, $I_{0\to3} = 0.49$ and $I_{0\to4} = 0.03$, which corresponds to a relative weight of $65\%, 27\%, 8\%$ and 0%, respectively, in good agreement with the IETS data. However, this approach makes wrong predictions on the elastic conductance and cannot account for the overall strength of the magnetic transitions. Indeed, the elastic contribution would yield $I_{0\to0} = 0.95$ and thus is greatly underestimated when compared to the measurements (Fig. 3.5b). Following the study of Hirjibehedin *et al.*, several theoretical models based on one-electron approaches were developed [94, 95], but failed in producing quantitative estimates of the ratio between the inelastic and elastic conductances. A strong coupling theory has been later developed for the magnetic IETS transitions by Lorente *et al.* [91, 92], which explicitly introduces the spin symmetries of the problem and leads to a simple formulation, allowing then for quantitative predictions. This will be developped in chapter 5 with a concrete example.

More IETS experiments by other groups followed. Magnetic excitations could be detected in a variety of atomic scale systems and used to collect information on the magnetic properties of these systems: e.g. the magnetic anisotropy of iron phthalocyanine molecules was shown to depend on the molecular environment [97], the intermolecular exchange interaction between stacked cobalt phthalocyanine was estimated [101], or magnetic impurities have been analyzed on semiconductors [102]. The interactions between spins in individual atomic-scale magnetic structures could also be investigated by assembling linear chains, one magnetic atom (Mn for example) at a time on Cu_2N [98, 103]. The excitations in these finite chains can be considered as quantized spin waves in the finite object [104] where the tunneling electron first flips the spin of a single atom, and then the spin-flip propagates through the chain to build the actual excited state of the full system. More recently, spin torque transfer was shown to be effective in changing the spin orientation of an adsorbate in theoretical works [105, 106], and soon after it was shown experimentally by injecting spin-polarized inelastic electrons into Mn atoms on Cu_2N [107]. In this particular case, an intense spin polarized current is used to excite magnetic states at a higher rate than the natural decay of the atom, performing a spin-pumping experiment close to the phenomenon at work in lasers.

3.1.3 Lifetime of excited states

The magnetic IETS experiments described above were performed in systems in which an insulating layer separates the magnetic adsorbate carrying the spin from the metal surface. They show that an insulating layer and an important magnetic anisotropy lead to spin lifetimes in the ns range [108, 107] and a slightly longer lifetime of 10 ns was evidenced for an organometallic molecule on a superconducting Pb surface [109].

However, when the magnetic atoms are directly adsorbed on a metal substrate the spin lifetime is greatly reduced. This leads to an increased broadening of spectral features and excitations are poorly resolved in energy so that IETS in general becomes harder to detect on a metal surface. Nevertheless, Khajetoorians *et al.* have measured a lifetime of 200 fs for the magnetic excitations of individual Fe atoms on Cu(111) [110] with step heights representing only 5% of the elastic conductance. Interestingly, the Fe magnetic moment extracted from averaged experimental single atom magnetic curve (dI/dV signal at at given bias with respect to magnetic field) is 3.4 μ_B, quite different from the 4.0 μ_B deduced in the IETS experiments of Fe on Cu_2N/Cu(100) by Hirjibehedin *et al.*. The decreased value of the Fe magnetic moment is attributed to the strong hybridization of the Fe atom with the metallic substrate. The lifetime limiting process can then be traced back to substrate electrons colliding onto the magnetic adsorbate and causing a de-excitation of the system. The decay of excited magnetic states in individual adsorbates thus proceeds via electron-hole pair creation.

A breakthrough in this domain was recently achieved by Donati *et al.* [96]. By placing a Ho atom on a thin insulating layer of MgO, they observed that Ho can have a spin lifetime up to 1500 s at 10 K. They demonstrated that the long lifetime is due to the localized nature

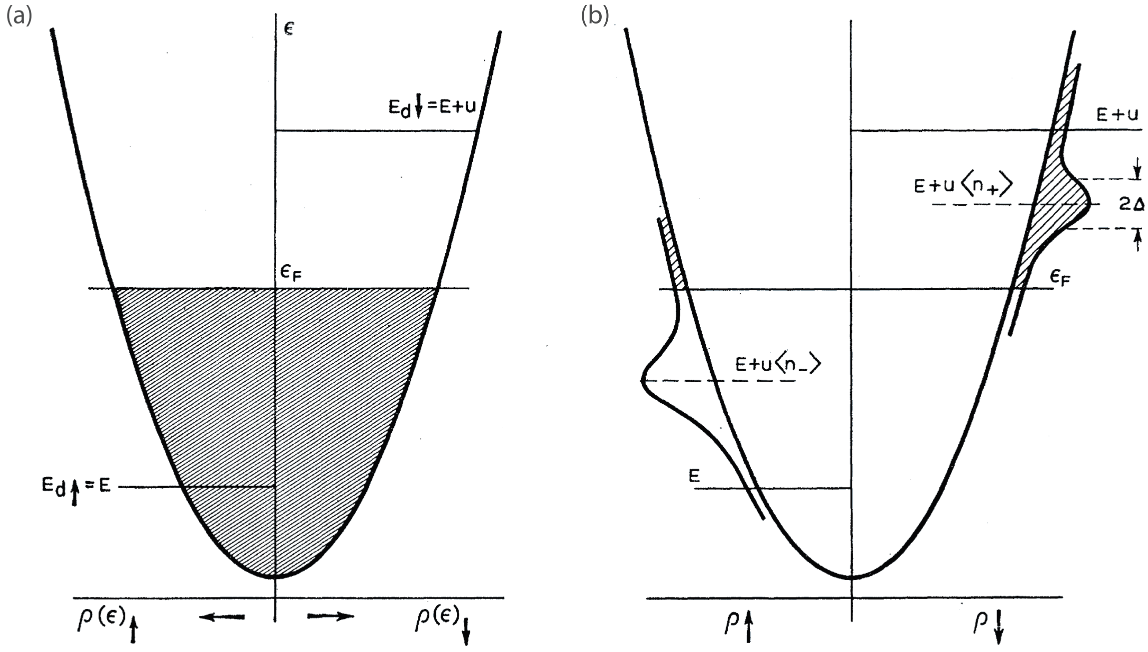

Figure 3.7: **Anderson model.** (a) Density of states (ρ)of a metal with a localized d impurity without $s-d$ mixing, and (b) with $s-d$ mixing. Taken from [111].

of the Ho $4f$ orbitals which results in a symmetry-protected magnetic ground state upon adsorption on MgO, and to the decoupling of the Ho spin from the underlying metal by MgO.

3.2 The Kondo effect

Magnetic excitations in single atoms are only a minor part of a larger problem in physics known as the impurity problem. The Kondo physics represents another facet of the problem which goes way back to the beginning of the 20th century. At the time, it was well established that atomic vibrations are frozen in a metal when the temperature is reduced, causing the resistivity to decrease with temperature and finally stabilize to a residual resistance due to structural defects and impurities. An increase in resistivity with decreasing temperature was instead observed in a gold metal with iron impurities [112]. In 1964, Jun Kondo theoretically explained this observation [113] in terms of spin-flip scattering events involving the spin of the magnetic impurity and the spins of the conduction electrons of the host metal. The model proposed a logarithmic increase of the resistivity below a critical temperature in a second order perturbation theory. Nowadays this effect is the so-called Kondo effect. The logarithmic increase of the resistivity is associated to the screening of the magnetic impurity

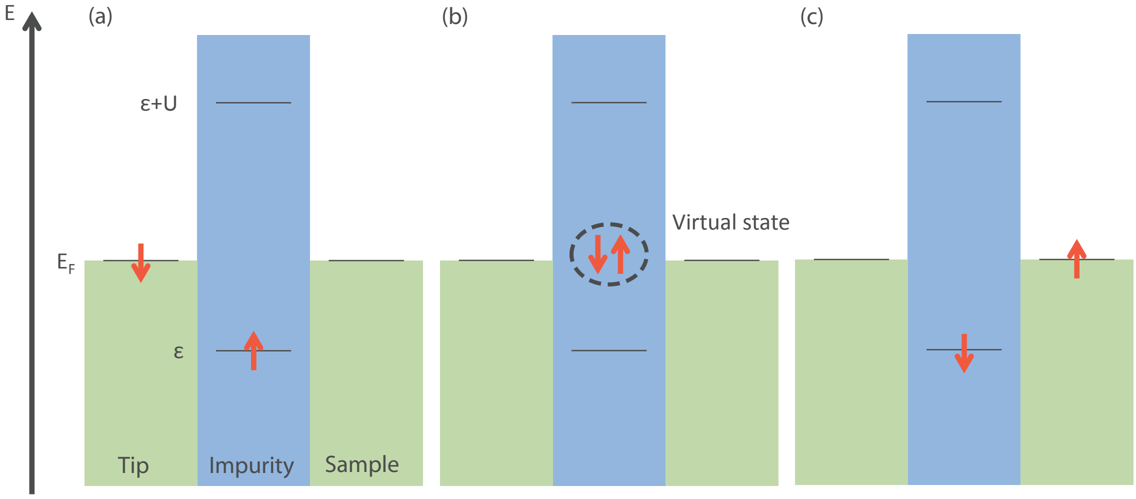

Figure 3.8: **Electron tunneling between the conduction band and the impurity.** (a) Before the tunneling process, (b) Virtual state where the two electrons combine with opposite spin, (c) After the tunneling process.

by the spins of the conduction electrons in the host metal and is therefore a many-body phenomenon involving electron-electron correlations.

3.2.1 Brief overview

A first clue to solving the problem was given in 1961 by the $s-d$ mixing model of Anderson [111]. In this model, the magnetic moment of the impurity is described by a single d-orbital with energy ε_d located below the Fermi level (ε_F), which is filled with a $S = 1/2$ spin-up electron (Fig. 3.7). A spin-down electron which would like to occupy the same level sees the repulsive Coulomb interaction U of the spin-up electron already occupying the level. Therefore only the $\varepsilon_d + U$ level is available for the spin-down electron. As long as this level is above the Fermi energy, the impurity has a net magnetic moment(Fig. 3.7c). This can however change as the d-orbital is hybridized to the electron s-band leading to a coupled system described by the Hamiltonian

$$\mathscr{H} = \sum_{\kappa,\sigma} \varepsilon_\kappa \hat{c}^\dagger_{\kappa\sigma} \hat{c}_{\kappa\sigma} + \varepsilon_d \sum_{\sigma} \hat{d}^\dagger_\sigma \hat{d}_\sigma + U \hat{n}_{d_\uparrow} \hat{n}_{d_\downarrow} + \mathscr{H}_{\kappa d}, \tag{3.6}$$

where ε_κ is the unperturbed energy of the s electrons in the metal, while the operators $\hat{c}^\dagger_{\kappa\sigma}$ ($\hat{c}_{\kappa\sigma}$) and $\hat{d}^\dagger_\sigma$ ($\hat{d}_\sigma$) create (destroy) an electron in state $|\kappa,\sigma\rangle$ and $|d,\sigma\rangle$, respectively. The Coulomb interaction U accounts for the repulsion between opposite-spin electrons on the d orbital. The last term of the Hamiltonian

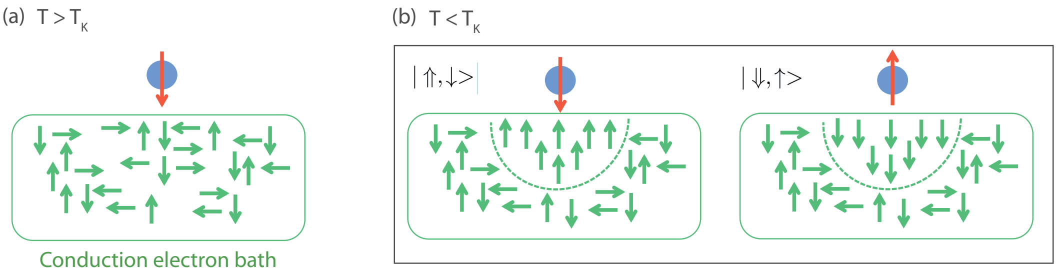

Figure 3.9: **Sketch of the Kondo ground state.** Electron scattering by a magnetic impurity (a) without screening above T_{K}, and (b) with screening below T_{K}. The Kondo state consists in a linear combination of $|\Uparrow,\downarrow\rangle$ and $|\Downarrow,\uparrow\rangle$.

$$\mathscr{H}_{\kappa d} = \sum_{\kappa\sigma}(V_{\kappa\sigma}\hat{d}^{\dagger}_{\sigma}\hat{c}_{\kappa\sigma} + V^{*}_{\kappa\sigma}\hat{d}_{\sigma}\hat{c}^{\dagger}_{\kappa\sigma}) \tag{3.7}$$

describes the scattering of conduction electrons onto the impurity. This occurs through the tunneling of the impurity electron into the conduction band and the concomitant tunneling of one electron of the conduction band into the impurity (Fig. 3.8). Due to the Pauli principle the two electrons have opposite spins, so that after the scattering event, the impurity spin and the conduction electrons spin have flipped. Because of the $s-d$ mixing term $V_{\kappa d}$, there is a perpetual change between up and down spin of the impurity [114]. The $s-d$ mixing shortens the lifetime of the d-state causing it to broaden in energy. Formally, the half width at half maximum of the d state is expressed by $\Gamma = \pi\rho|V_{\kappa d}|^2$ where ρ is the the density of states of the metal at the Fermi level. For a strong coupling, the width of the d state is large enough to cross the Fermi level, leading to a reduction of the magnetic moment of the impurity (Fig. 3.7b).

Three years after Phillip Anderson's works, Jun Kondo proposed to use perturbation theory to describe the scattering of electrons by magnetic impurities [113]. This model is only valid below a critical temperature called Kondo temperature (noted T_{K}) and predicts that the resistivity diverges when the temperature tends to zero. The Kondo effect describes an elastic spin exchange between the magnetic impurity and the spin of the conduction electrons. The Hamiltonian proposed by Kondo is similar to Anderson's, except that the $s-d$ term is replaced by an exchange term

$$\mathscr{H}_{ex} = J_{\mathrm{K}}\hat{S}\cdot\hat{s} = -\frac{J_{\mathrm{K}}}{2N}\sum_{\kappa,\kappa'}[(\hat{c}^{\dagger}_{\kappa'\uparrow}\hat{c}_{\kappa\uparrow} - \hat{c}^{\dagger}_{\kappa'\downarrow}\hat{c}_{\kappa\downarrow})\hat{S}_z + \hat{c}^{\dagger}_{\kappa'\uparrow}\hat{c}_{\kappa\downarrow}\hat{S}_- + c^{\dagger}_{\kappa'\downarrow}\hat{c}_{\kappa\uparrow}\hat{S}_+], \tag{3.8}$$

where J_{K} is the amplitude of the $s-d$ exchange interaction between the impurity spin and the spin of the conduction electrons. In this expression, the total spin momentum has to be conserved. When the $\hat{S}_{+}$ operator rises the spin of the impurity from down to up, the operators $\hat{c}^{\dagger}_{\kappa\downarrow}\hat{c}_{\kappa\uparrow}$ changes the conduction electrons spin from up to down. The exchange term $\mathscr{H}_{ex}$ therefore describes a spin-flipping process between the local moment carried by the impurity and the spins of the N electrons. The Kondo Hamiltonian leads to a new electron state below the so-called Kondo temperature, which may be expressed as

$$k_{\mathrm{B}}T_{\mathrm{K}} = W\sqrt{2\rho|J_{\mathrm{K}}|}exp(1/2\rho J_{\mathrm{K}}), \tag{3.9}$$

where $W \simeq \varepsilon_{\mathrm{F}}$ is the bandwidth of the conduction electrons and ρ is their density of states. Below T_{K}, the many-body ground state comprises the impurity spin and a correlated "cloud" of conduction electrons screening a magnetic moment of the impurity (Fig. 3.9). The ground state of the impurity is doubly degenerate; it can be expressed as a linear combination $(|\Uparrow,\downarrow\rangle + |\Downarrow,\uparrow\rangle)/\sqrt{2}$, where the large arrows stand for the conduction electrons and the small arrows for the impurity.

The Kondo and Anderson models are equivalent as demonstrated in 1966 by Schrieffer and Wolff [115]. In the limit of the small $s-d$ mixing, *i.e.* at low values of Γ compared to ε_d, a canonical transformation enables to re-express the $\mathscr{H}_{\kappa d}$ term of the Anderson model as the $\mathscr{H}_{ex}$ term of the Kondo expression. A rather simple expression between J_{K} and the Anderson parameters can then be established

$$\frac{J_{\mathrm{K}}}{N} = -\frac{2}{\pi\rho}\frac{\Gamma U}{|\varepsilon||\varepsilon+U|}, \tag{3.10}$$

where it can be seen that J_{K} is antiferromagnetic ($J_K < 0$).

3.2.2 Tunneling into a single Kondo impurity

In 1998, the first experimental observation of the Kondo effect in a single object was reported in a quantum dot bridging two metallic leads [116, 117]. The Kondo effect is detected through transport measurements due to the formation below T_{K} of a sharp peak in the density of states near the Fermi energy, known as Abrikosov-Suhl resonance or simply, the Kondo resonance. In the same year, the Kondo resonance was observed for the first time in a single magnetic atom adsorbed on a non magnetic surface by STM [118, 119] (Fig. 3.10). Madhavan *et al.* showed that a narrow asymmetric feature near ε_F appears in the dI/dV of cobalt atoms on a Au(111) surface [119]. The amplitude of the resonance was shown to be maximum when positioning the tip above the center of the single atom and was progressively lost when moving away laterally, confirming that the effect is localized at the atom site.

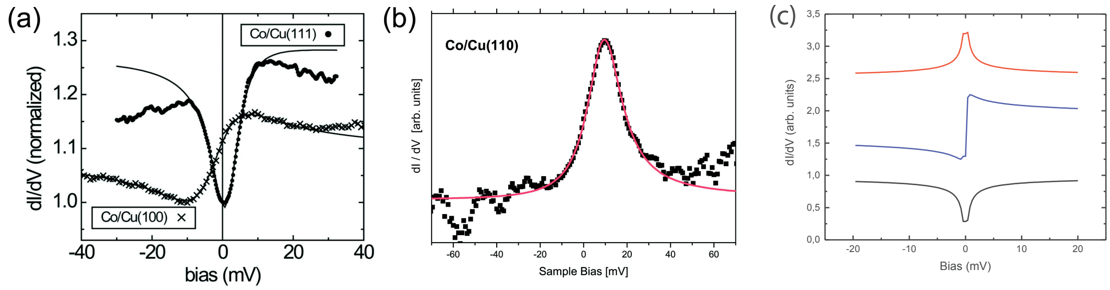

Figure 3.10: **Kondo resonance of single Co on various surfaces.** (a) dI/dV spectra for Co/Cu(100) and Co/Cu(111) surfaces. Taken from [124]. (b) dI/dV spectrum above Co on Cu(110). Taken from [125]. (c) Simulated STS spectra (T_K = 2.5 K) vertically shifted for clarity. The black curve illustrates a Fano factor $q = 0.01$, the blue one corresponds to $q = 1$ and the red curve corresponds to $q = 100$.

The values of the Kondo temperature for adsorbed atoms are generally lower compared to when they are embedded in bulk due to the reduced coordinance, that is to say a lower coupling of the adatom with its surroundings. For example, for cobalt T_K is approximately 30 K on a copper surface while in bulk copper T_K is around 500 K. To a minor degree, the surface structure can also modify T_K by changing the equilibrium position of the adsorbed atom; as we mentioned above, the Kondo temperature is exponentially sensitive to changes of the coupling Γ between the impurity and the metal host (cf. Eqs. 3.9 and 3.10) [120]. The tip can even be used to artificially modify this equilibrium position and therefore controllably tune the Kondo temperature [121–123].

Another salient aspect is that the Kondo resonance can present an asymmetric lineshape in STM. The asymmetry varies depending on surface material and structure. Figure 3.10 shows for example the dI/dV spectra acquired above a Co atom on Cu(100), Cu(111) and Cu(110) [124, 125]. A step-like feature is found for Cu(100), while a dip is observed on Cu(111) and a peak is detected on Cu(110). This results from the quantum interference between the two paths available to the tunneling electrons. Electrons originating from the tip can tunnel into the Kondo resonance which lies close to ε_F (path 1 of Fig.3.11a) or in the empty bulk states above ε_F of the metal (path 2 of Fig.3.11b). The two different paths are chosen by the tunneling electrons with probabilities given by the tunneling matrix elements t_1 and t_2 for tunneling into the Kondo resonance and the bulk states, respectively. The weight of each path, *i.e.* the ratio t_1/t_2, determines the lineshape of the Kondo resonance [118**?** , 126]. The Kondo lineshape in STM is well described by a Frota-Fano model [127, 128] (Fig. 3.11c),

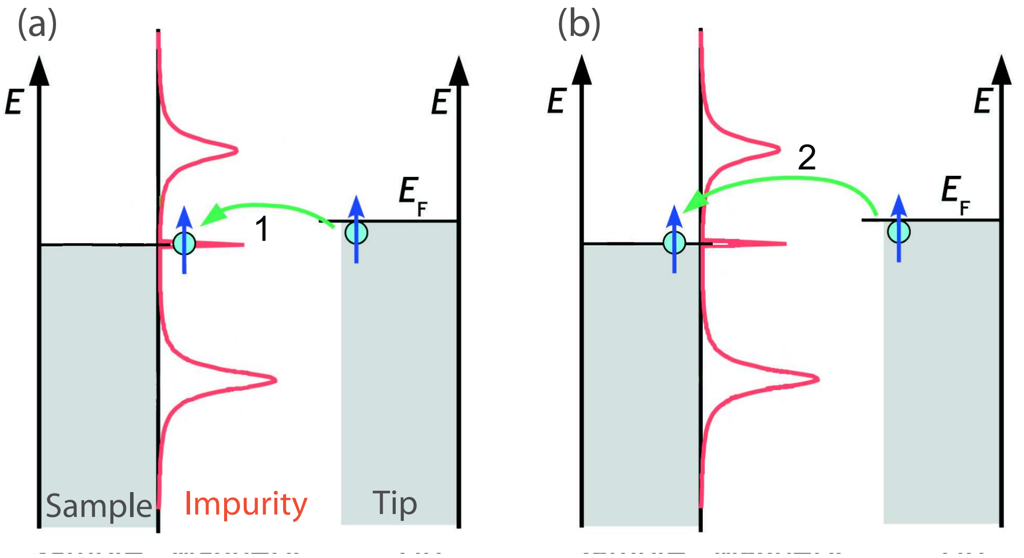

Figure 3.11: **Tunneling paths for the Kondo effect in a STM junction and Fano line shape.** Schematic view of the tunneling paths that electron can follow when the STM tip is positioned above a Kondo atom: (a) direct tunneling into the Kondo resonance of the atom. (b) tunneling into the empty states of the sample.

$$\sigma(eV) = h\left\{(q^2-1)g(x) + sgn(x)2|q|\sqrt{g(x)[1-g(x)]}\right\} + \sigma_0, \tag{3.11}$$

with $x = \frac{eV-\varepsilon_K}{1.455k_BT_K}$ and sgn representing the sign function, while ε_K, h and σ_0 are constants. The Fano parameter q accounts for the lineshape asymmetry and g is the Frota function [129]

$$g(x) = \Re\left(\sqrt{\frac{i}{i+x}}\right), \tag{3.12}$$

with $\Re(z)$ the real part of z. Figure 3.10c presents some simulated lineshapes with increasing q. By using Eq. (3.11) to fit experimental data, it is possible to accurately estimate the Kondo temperature of a system [122].

3.2.3 Kondo physics and magnetic IETS

The Kondo effect results from the screening of the spin of a magnetic impurity by the conduction electrons of a metallic substrate. Unlike the inelastic spin-flips occurring in magnetic IETS, the Kondo effect involves an elastic spin-flip of the conduction electron, *i.e.* it has no cost in energy. Nevertheless, the two scattering mechanisms have some points in

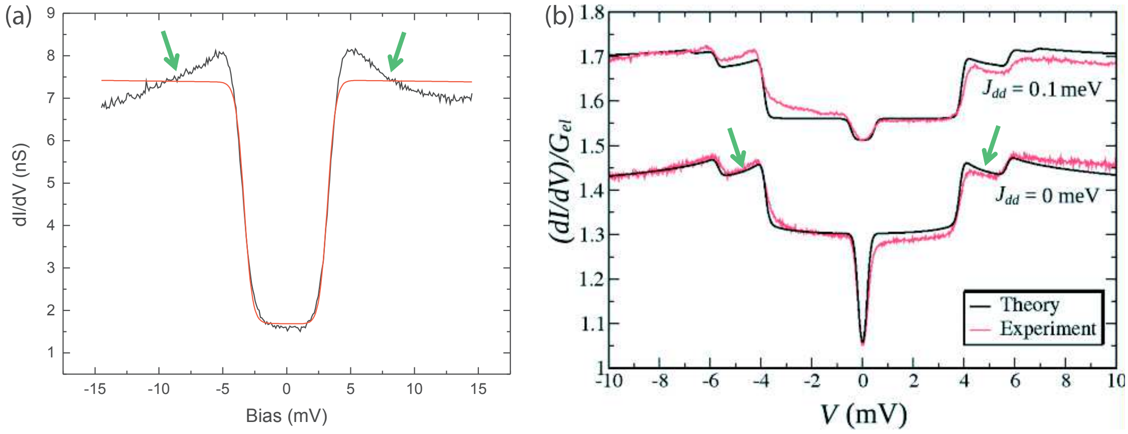

Figure 3.12: **Many-body effects in magnetic IETS.** (a) dI/dV spectra acquired above a nickelocene molecule (see chapter 5) and simulated spectrum based on a one-electron approach (solid red line). The green arrows point to the logarithmic-like decays following the conductance steps. (b) Normalized conductance spectrum for a Co adatom on Cu_2N. The calculated spectra are in black, while the corresponding experimental data from are in red. Image extracted from [132].

common, which we will briefly highlight hereafter. We refer the reader to the review by Ternes [130] and Gauyacq *et al.* [131] for an extensive presentation.

As we showed, the signature of the Kondo effect in an STM experiment consists in a zero-bias anomaly in the conductance spectra. This singular behavior is also present at the conductance steps of magnetic IETS. To illustrate this, we show in Fig. 3.12(a) a typical dI/dV spectrum acquired above a nickelocene molecule (see Chapter 5) where additionally we simulated the IETS spectrum using a one-electron approach [82]. In the experimental spectrum, the spectral weight is greatly increased near the steps (arrows in Fig. 3.12a) and yields peak-like features at variance with the abrupt steps present in the simulated line. A better agreement with experiments is obtained via many-body theory including Kondo-like phenomena [132, 133], which predicts a logarithmic decay of the conductance as a function of bias subsequent to a conductance step (Fig. 3.12b). However, as shown by Loth *et al.* [107], the repeated excitation of the magnetic states as the tunneling current increases could also contribute to the peak-like features at the inelastic threshold.

Another noticeable feature is that many-body effects can shift the inelastic thresholds. This is an important effect for accurately extracting the magnetic energies from IETS. The most striking experimental evidence for this shift was reported by Oberg *et al.* [99]. They observed that the IETS spectra of Co atoms on $Cu_2N/Cu(100)$ islands change dramatically depending on the lateral distance of cobalt to the copper surface (Fig 3.13a). As cobalt

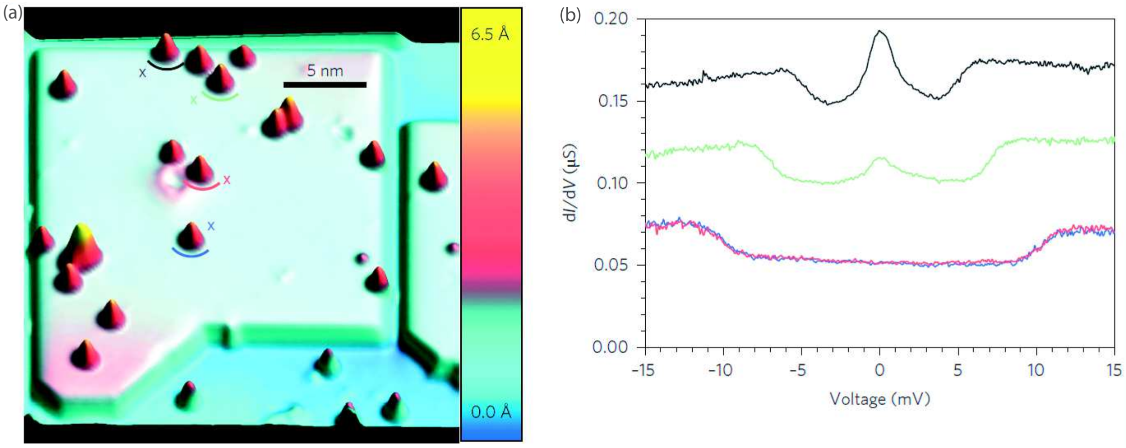

Figure 3.13: **Kondo effect and magnetic IETS for Co/Cu$_2$N**, taken from [99]. (a) STM image of the Co atoms deposited on Cu$_2$N islands. (b) dI/dV spectra recorded above different Co atoms. The colors correspond to the color labels of panel (a). The spectra are shifted for clarity.

approaches the edge of the Cu$_2$N island, the relative height of the Kondo peak increases and the IETS conductance steps shift to lower energy, (Fig 3.13b). This behavior can be explained using both Kondo and Anderson models through second-order perturbation theory. A renormalized spin excitation value Δ can then be expressed as

$$\Delta = \Delta_0 \left[1 - \frac{3}{16} \left(\rho J_{\mathrm{K}} \right)^2 \ln \left(\frac{2W}{\pi k_{\mathrm{B}} T} \right) \right], \tag{3.13}$$

where Δ_0 is the bare excitation energy, W the bandwidth of the conduction electron and T the temperature. The equation links the Kondo peak to the magnetic IETS as ρJ_{K} also determines the Kondo temperature of cobalt, cf. Eq. (3.9). Qualitatively, the above relation accounts for the experimental observation: as ρJ_{K} decreases, the Kondo temperature decreases, and at the same time the spin excitation energy goes up.

Summarizing, in this chapter we have presented how STM can detect spin-flip scattering events. We first presented magnetic IETS which allows for the detection of magnetic excitations of surface-supported atoms or molecules through inelastic spin-flips of the tunneling electrons. These excitations provide information on the magnetic ground state, in particular on the magnetic anisotropy, of the object studied. We then focused on the Kondo effect of a single atom, which involves elastic spin-flip scattering. We showed that STM can be used to characterize the Kondo ground state at the atomic scale through the detection of the Kondo resonance. Both magnetic IETS and Kondo physics will be addressed at the molecular level in the following chapters.

Chapter 4

Spin doping a metallocene

As described in chapter 1, the compostion of a molecule and especially its anchoring group to the surface are determinant for the magnetic properties of the system. Here, we propose a method to combine metallocenes and magnetic atoms to create a new entity. Such a spin-doping process has already been experimented on double deckers based on phtalocyanine (Pc) molecules. First, Gambardella and coworkers[134] showed that the magnetization of a substrate can influence the magnetic proprerties of $Tb(Pc)_2$. One year later, Robles and coworkers [30] deposited Cs atoms on $Y(Pc)_2$. They showed that the Cs atom donates an electron to the molecule and thus changes its DOS. Furthermore, the Kondo peak identified above the molecular layer disappears in the neighbourhood of the Cs adatom, showing a dramatic change in local DOS. The same kind of result was reported for CuPc molecules [31] which were doped with one to four Li adatoms. This led to a change in magnetism of the molecules and therefore to different resonances in STS spectra.

In our case, we specifically focus on ferrocene as an originally non magnetic metallocene and the way it interacts with Co extra atoms to create a new magnetic entity. This chapter will be devoted to the study of ferrocene molecules from an experimental point of view, with the support of DFT computations. The first part is dedicated to the deposition of the molecule on a sample surface. This was the subject of only few experimental and contradicting works so far, so we propose a complete analysis of the ferrocene adsorption on copper surfaces. The second part of the chapter will deal with the spin doping of $FeCp_2$ by a Co atom, starting with the different methods used to create the new systems and then moving to their magnetic characterization.

4.1 Ferrocene deposition and adsorption on noble metals

The first objective consists in depositing $FeCp_2$ on a metallic and non magnetic surface. Up to now, different types of adsorptions have been reported. Several studies reported an associative adsorption (adsorption with intact molecules) at low temperature on Ag [135–137]. These results were obtained on cold Ag(100) crystals by mean of averaging methods, Angle Resolved Photo-Emission Spectroscopy (ARPES) and High Resolution Electron Energy Loss Spectroscopy (HREELS). They claimed a preferential orientation of the molecular axis perpendicular to the surface, *i.e.* a physisorption of vertical molecules (Fig. 4.1). The latter results also indicate the growth of ferrocene assemblies occurs layer by layer. The desorption of ferrocene on Ag(100) induced by temperature was found to start at 150 K with desorption of intact molecules. However, a radiation induced desorption (molecules illuminated with synchrotron radiations) was found to cause a decompostion of $FeCp_2$ during the desorption process. Similar experiments were carried out on graphite and reported a physisorption of vertical molecules again on graphite at 140 K [138]. A second work [139] claimed a partial fragmentation of horizontal $FeCp_2$. On a Mo surface [140], horizontal ferrocenes were found to be associatively adsorbed at 150 K and decomposed at room temperature (300 K). The results obtained on Cu(100) [136], showed an associative physisorption of horizontal $FeCp_2$, with a preferential axis orientation along the [110] direction.

Progresses in local probe measuring techniques enabled STM measurements on such molecules. K. F. Braun and coworkers [141] proposed a dissociative adsorption model of $FeCp_2$ on Au(111), while an associative adsorption has been addressed for various ferrocene-derived molecules on the same substrate [142, 143] or different surfaces [144]. B. W. Heinrich and coworkers [145] presented a molecularly physisorbed ferrocene on Cu(111) lying with the molecular axis perpendicular to the surface. This last result is contradicting the experiments of [136]. Because of the little consensus on ferrocene adsorption onto surfaces, we first dedicated our experiments to undertand the adsorption geometry of ferrocene deposited on noble metals, Cu crystals in our case, thanks to STM imaging.

4.1.1 Deposition procedure

In a first step, we purified the commercial ferrocene powder by spontaneous desorption of impurities in vacuum at room temperature, mainly to remove the remaining solvants. This process was achieved in the preparation chamber. The pressure during the process evolved from 10^{-4} mbar to 10^{-7} mbar in a few hours, indicating that impurities (supposed to be remaining solvant traces) are pumped away. A pressure in the order 10^{-7} mbar was experimentally found to be the moment when the ferrocene starts to degrade in the crucible.

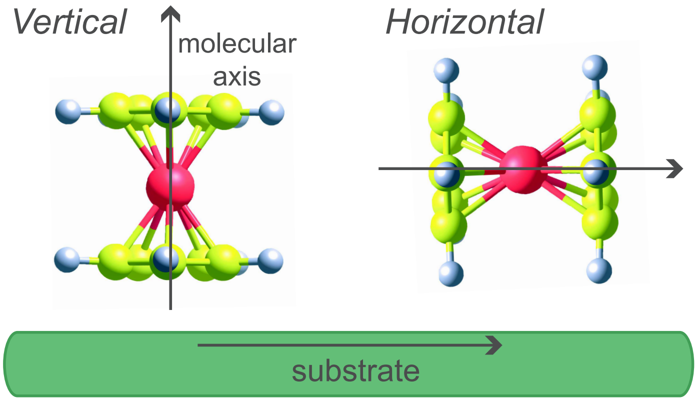

Figure 4.1: **Possible adsorption geometries of ferrocene on a surface.** The molecular axis is indicated in both cases with a dashed arrow. White, yellow, and red balls represent H, C, and Fe atoms, respectively.

This was verified by the yield reduction in molecular deposition and a significant change in color of the remaining entities in the crucible, going from green crystals to orange powder.

The deposition process has to be done on a cold sample so that the molecules stick to the surface. Deposition attempts at room temperature did not result in exploitable samples: the images only exhibited small features on the sample surface incompatible with the $FeCp_2$ apparent height previously recorded on metals [142, 143]. The method we used here consists in taking out the sample from the cryostat and keeping it on the wobble stick in front of the gate valve separating the STM chamber (10^{-10} mbar) and the preparation chamber (10^{-7} mbar) where the crucible is emitting ferrocene at room temperature. Opening the valve between the preparation and the STM chambers allows the ferrocene to flow towards the sample and some of the molecules adsorb on the sample (Fig. 4.2). During the process, the sample is no longer cooled down by the helium bath and its temperature is estimated to be below 150 K. Such a procedure enables to obtain a deposition rate of approximately 1.2 monolayers per minute on the sample surface. After deposition, the samples were immediately cooled down to 4.6 K and analysed by STM.

The $FeCp_2$ molecules can be desorbed by warming up the samples while monitoring the pressure in the STM chamber. At 182 K, the pressure suddenly rises in the 10^{-9} range, suggesting a desorption of the molecules. STM images of the surface after the operation confirmed the disappearence of the ferrocene on the copper crystal.

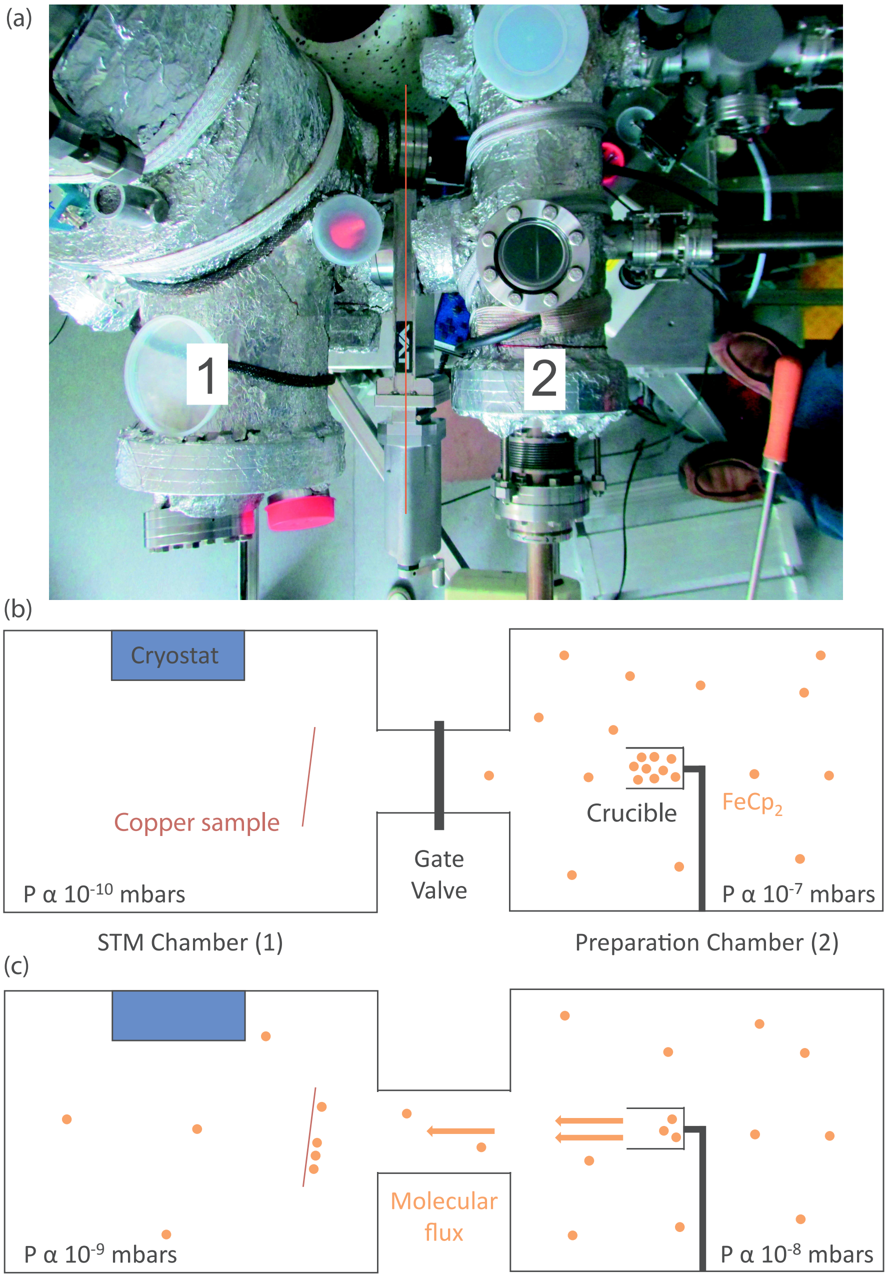

Figure 4.2: **Experimental setup for ferrocene deposition.**(a) Top view photo of the STM chamber (1) and the preparation chamber (2). The red line corresponds to the gate valve between the two chambers. (b) Sketch of the two chambers before the deposition. The crucible in the preparation chamber contains the ferrocene molecules. The copper sample is set in front of the gate valve thanks to the wobble stick (not represented). (c) When the valve is opened, the ferrocene flows to the STM chamber and sticks on the copper surface facing the valve.

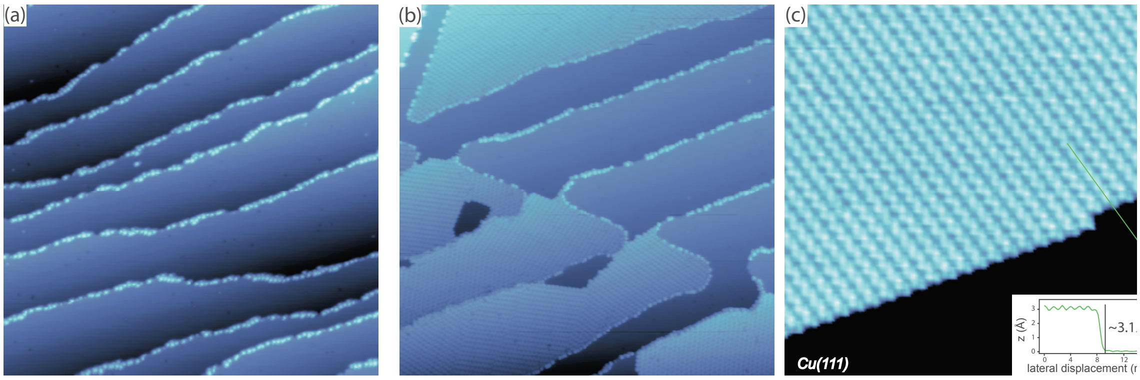

Figure 4.3: **Ferrocene growth on Cu(111) surface.** (a) About 0.1 monolayer of molecules was deposited, leading to a step edge decoration. (b) A deposition of 0.6 monolayer of ferrocene is sufficient to give rise to a self-assembled network on the sample surface. On some areas, the step decoration is still visible. (c) STM image (+1 V, 0.5 nA) of 0.6 monolayer $FeCp_2$ deposited on Cu(111). Inset: Height profile of the molecular monolayer. Image size: 30×30 nm^2.

4.1.2 Deposition on Cu(111)

Let us first analyse the adsorption on Cu(111). For a small quantity of $FeCp_2$ deposited on the sample (below 0.2 monolayers), we obtained only step decoration on a Cu(111) surface (Fig. 4.3a). The molecules appear as bright protrusions with an apparent height of 3.1 Å, as already observed in previous STM studies [145].

A larger quantity of molecules, around 0.6 monolayers, gives rise to long-range well-ordered molecular layers with almost no defects (Fig. 4.3b-c). Self-assembly processes have already been reported for Fe-phen molecules [146] or ferrocene derivatives [143]. The apparent height exhibited by the ferrocene layers is the same as for ferrocene molecules at the step edge, 3.1 Å (inset in Fig. 4.3c). An analysis of the molecular adsorption on the surface as a function of the coverage indicates that the ordered islands grow from the step edges of the copper crystal.

Among the layers, two different molecular configurations, which we label "compact" and "zigzag" (Fig. 4.4a,c respectively), appear equally distributed across the surface.

Compact configuration

In the compact configuration (Fig. 4.4a), elongated rod-like protrusions can be observed between ring-like protrusions. We assign the ring-like units to the Cp rings of vertical $FeCp_2$ while the rod-like protrusions around rings are assigned to horizontal $FeCp_2$ (Fig. 4.1). The supposed horizontal ferrocenes appear with a height 0.5 Å lower than upstanding molecules.

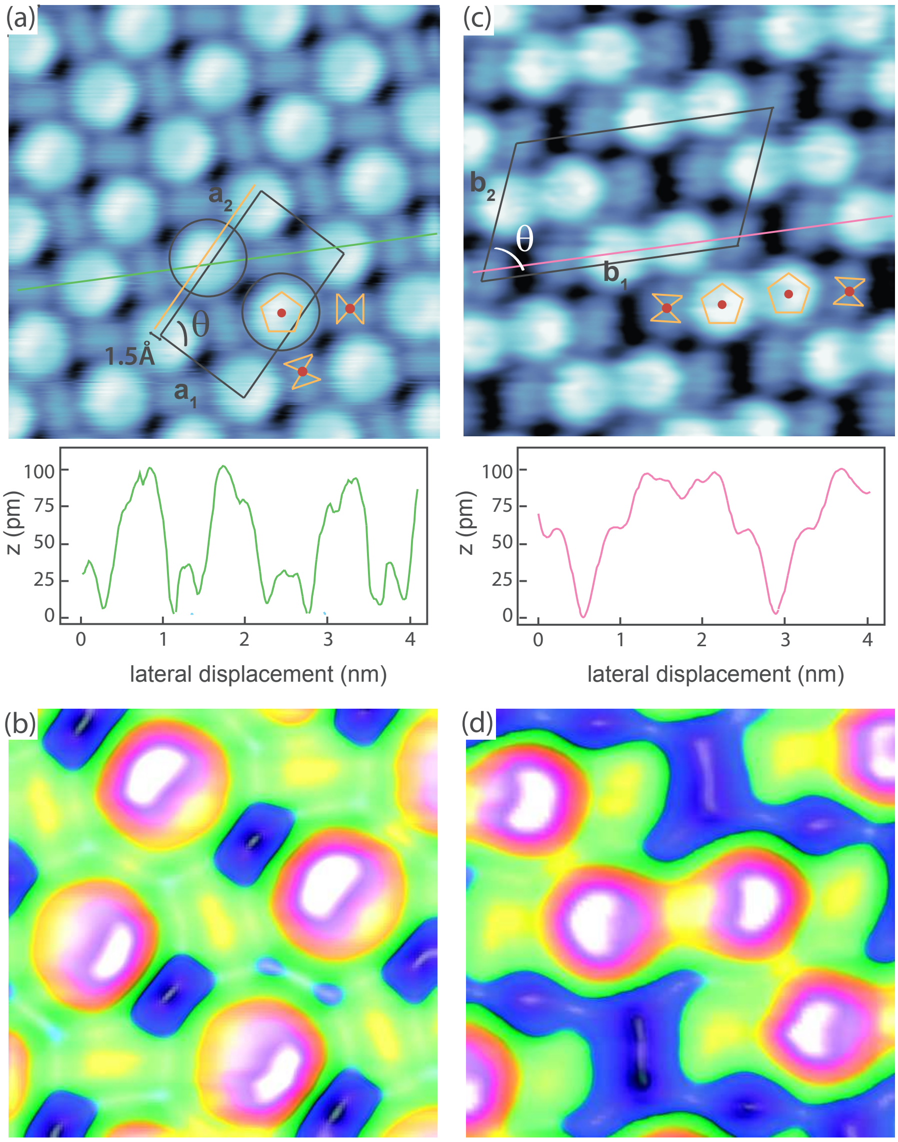

Figure 4.4: **Ferrocene networks.** Ferrocene molecules adopt two different configurations on Cu(111): (a) compact (-1 V, 0.5 nA)and (c) zigzag (+0.1 V, 0.2 nA). The compact configuration is made of an alternating combination of vertical and horizontal molecules. In the zigzag configuration the vertical molecules group form dimers. The unit cells (black dashed lines) as well as the line profiles of both arrangements are shown in each image. (b-d) Close up view of the two configurations, highlighting the asymmetry of the rings in the vertical molecules. Image sizes: (a-c) 4×4 nm^2, (b-d) 2×2 nm^2.

The corrugation of both vertical and horizontal molecules observed along the dashed green line in Fig. 4.4 is shown in the line profile below the image.

The rectangular unit cell of the compact configuration (marked in black in Fig. 4.4a) with lattice parameters a_1, a_2 and angle θ (see Table 4.1 for values), contains four molecules, two horizontal and two vertical ones. Consecutive vertical molecules in the a_2 direction do not lie exactly on the same axis (yellow axis and the molecules marked with circles in Fig. 4.4a), one being shifted aside by 1.5 Å with respect to the second. Moreover, vertical molecules present an asymmetry in the a_1 direction, being brighter on one side of the ring. Vertical molecules in the center and in the corner of the unit cell show the asymmetry at different sides of the ring. This asymmetry (Fig. 4.4b), as shown later, indicates that the axis of vertical molecules is tilted compared to the normal of the surface.

Zigzag configuration

Fig. 4.4c presents the zigzag configuration in which two ring-like protrusions, corresponding to vertical molecules, form a dimer-like pair. They are flanked by horizontal molecules which have a dimer shape with a fainter contrast in the image. The line profile taken along the pink dashed line in Fig. 4.4c shows the corrugation of the molecular assembly. Similarly to the compact case, the apparent height difference between vertical and horizontal molecules is around 0.5 Å. The distance between two adjacent dimer-like vertical molecules is (6.2±0.2) Å, which is small compared to the (8.0±0.2) Å found for the compact arrangement. The unit cell is a parallelogram (see parameters in Table 4.2), as shown in black in Fig. 4.4c. A similar ferrocene pairing has been also observed for ferrocene-derived molecules ($FeCp_2COOH$ and $FeCp_2$-$(CH_2)_n$-$FeCp_2$) deposited on metallic surfaces [143, 147, 144].

Although the identification of vertical ferrocene molecules is straightforward, determining the presence of the horizontal molecules is experimentally challenging. Therefore, to confirm the proposed model we rotated some molecules from a vertical (horizontal) to a horizontal (vertical) position by using the STM-tip [148], as in the layer shown in the before-and-after images (Fig. 4.5). The molecular structure of $FeCp_2$ is superimposed in zooms (Fig. 4.5). Upon application of a bias pulse of 2 V, molecules rotate out-of-plane from horizontal to vertical (molecules noted 1 and 2), or vice versa (molecules noted 3 and 4). In-plane rotations may exist but are difficult to identify. In this example, when the vertical axis of $FeCp_2$ is rotated by nearly 90° (molecule parallel to the surface), the ring-like feature is replaced by the same rod-shaped feature as identified aside vertical molecule. This experimentally supports the hypothesis of the presence of both vertical and horizontal molecules in the molecular layers.

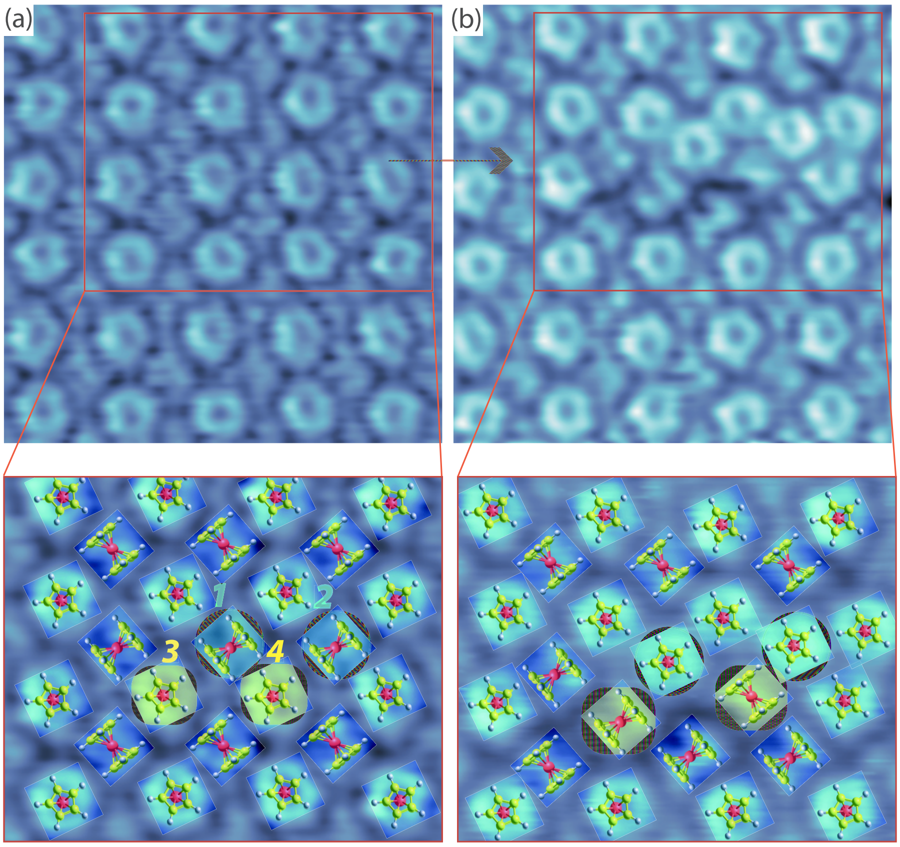

Figure 4.5: **Ferrocene zigzag network.** STM images (+1 V, 1 nA) of the compact configuration on Cu(111) before and after some molecules turned from a vertical to a horizontal position, or vice versa, via tip-assisted manipulation. The lower images correspond to the marked squares in the top pictures, with the sketched molecules superimposed to highlight the molecules that have rotated (1-4). Notice that a molecular tip has been employed in order to enhance the observed features. Additionally, a laplacian filter has been applied. Image sizes: (a-b) 4.5×4.5 nm^2.

4.1.3 Deposition on Cu(100)

Let us now examine the adsorption of $FeCp_2$ on Cu(100). Both compact and zigzag arrangements are co-existing on the surface (Fig. 4.6). This shows that the crystal orientation does not have a strong influence on the network, suggesting that the molecules have a weak coupling with the substrate, indicating a probable physisorption. Reinforcing this idea, we find that the rotational domains observed for each configuration in the Cu(111) surface, (0°, 30°, 60°) for the compact and (17°, 50°) for the zigzag, are also observed for Cu(100). It dismisses the idea of a unique preferential orientation of the molecular axis with respect to

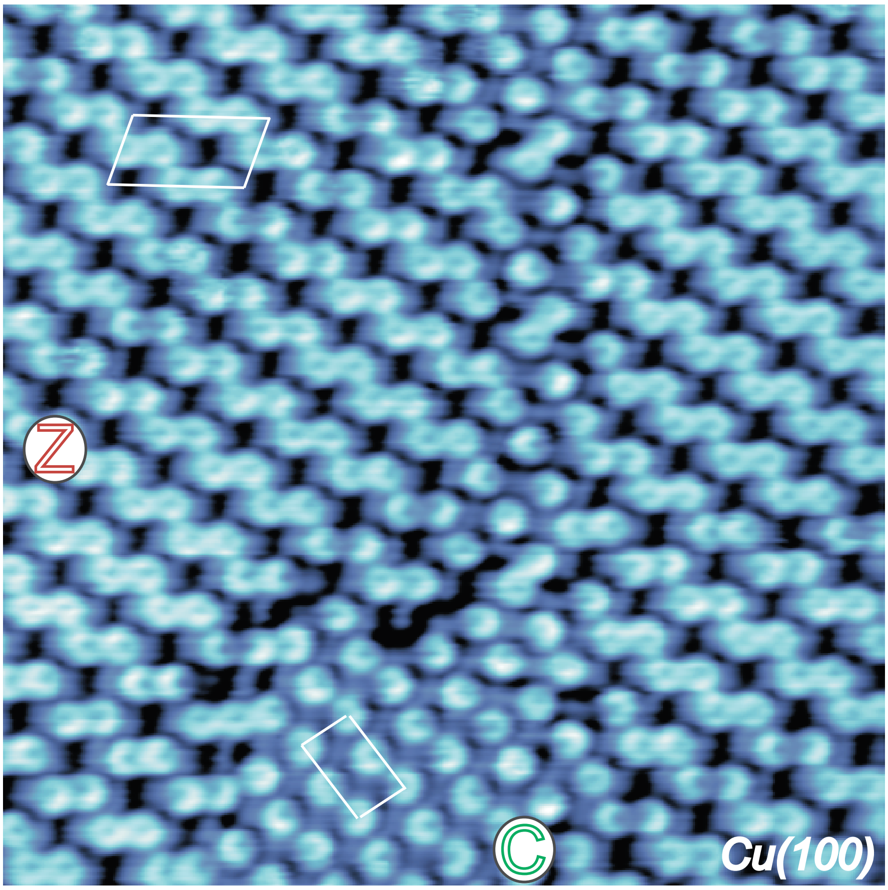

Figure 4.6: **Ferrocene networks on Cu(100).** The compact and zigzag arrangements on the surface are marked by C and Z respectively. The unit cells of both configurations are marked in white. (Image size: 15 × 15nm^2, 0.5 V, 1 nA.)

the substrate suggested in previous works and implies that the rotational domains are only related to the symmetry of the molecular layer itself and not to the one of the substrate.

4.1.4 STM and DFT study of networks stability

In order to better understand the adsorption geometry and interactions between ferrocene molecules, we performed DFT computations and simulated STM images of $FeCp_2$ adsorbed on Cu(111). *Ab initio* calculations have been performed within the DFT as implemented in the VASP code [149, 150]. We have used the generalized gradient approximation for the exchange and correlation functional [151], and the DFT+D2 method proposed by Grimme [152] to treat the missing van der Waals interactions. The initial arrangement for $FeCp_2$ layer

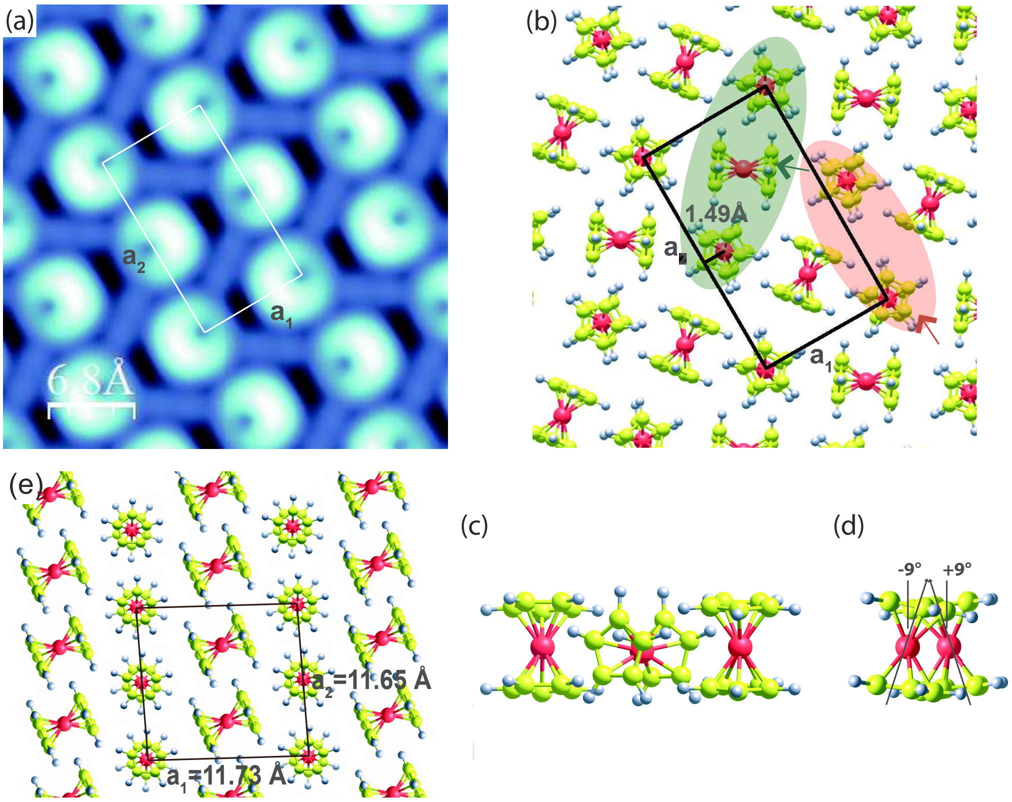

Figure 4.7: **Simulation of $FeCp_2$ compact network.** (a) Simulated STM topographic image for a bias of 1 V corresponding to the relaxed compact structure on the Cu(111) surface shown in (b). (c) Lateral views of the molecules hilighted in green in (b). (d) Lateral views of the vertical molecules along a_2 direction hilighted in red in (b). (e) Crystallographic (110) plane of the bulk solid ferrocene.

was taken out from experimental results and then relaxed. The first step consisted in studying the intra-molecular structure of ferrocene molecules.

Two different configurations exist for ferrocene molecules. First, the eclipsed configuration (Fig. 4.7b) consists in having the hydrogen atoms of the two Cp rings facing each other. It corresponds to the most stable structure in the gas phase [153–155]. The second one, called staggered configuration (Fig. 4.7e), consists in having the Cp rings parallel but shiffted by a 30 degrees angle so that the hydrogen atoms are not facing each other. This is the most common configuration in the solid state [156]. We found in our case that the layer is more stable on the surface by 45 meV with the eclipsed configuration for all adsorbed molecules. According to our calculations, no matter what initial state is chosen, the relaxation always leads to ferrocene with an eclipsed structure for both horizontal and vertical molecules. In the molecular layers discussed hereafter we find exclusively molecules in the eclipsed

Compact network on Cu(111)	a_1 (Å)	a_2 (Å)	θ (deg)	
Experiment	8.9 ± 0.3	15.5 ± 0.3	90 ± 3	
Theory	8.75	15.15	90	
E_{ads}(eV)	E_{ads}^{vdW}	E_{coh}^{free}	q(e-)	d Å
1.35	1.05	0.48	0.11	2.3

Table 4.1: **Compact ferrocene network parameters.** a_1 and a_2 are unit the cell dimensions, θ the angle between the unit cell vectors, E_{ads} the adsorption energy per molecule, E_{vdW} the van der Waals (vdW) contribution per molecule coming from the molecule-substrate interaction, E_{coh}^{free} the cohesive energy per molecule for the free-standing layer, q the molecule-substrate charge transfer per unit cell and d the molecule-surface distance.

configuration. We now focus on the inter-molecular arrangement of both compact and zigzag configurations.

Compact network

A closer view of the computed compact configuration is given in Fig. 4.7a-d. The rectangular unit cell observed in the STM images (Fig. 4.4a) corresponds within the experimental accuracy to a $2 \times 6\sqrt{3}$ unit cell in the Cu(111) surface (see Table 4.1). The stability of the proposed structure has been tested using this unit cell.

Comparing the simulated STM image (Fig. 4.7a) with the experimental one (Fig. 4.4a), we observe that the main features of the image are reproduced. The proposed structure (Fig. 4.7b-d) allows us to explain all the signatures present in experimental pictures : rod-like and ring-like protrusions in the STM image correspond to horizontal and vertical molecules respectively. The computations indicate that the minimum effective distance from the surface to the molecules of the layer is 2.3 Å. A strong contrast difference is observed between vertical and horizontal molecules in the STM images. At first glance, this contrast appears counterintuitive as horizontal molecules appear dimer, despite some of their H atoms are 0.2 Å further away into vacuum compared to the Cp ring of the vertical molecules (Fig. 4.7c). This apparent contradiction can be easily lifted by recalling that the tunneling transmission probability between the STM tip and the molecule depends on the tip and molecular orbitals. Orbitals that extend into the vacuum, such as s, p_z or d_z^2, will be favored in the tunneling process. In the present case, for vertical molecules, the d-manifold orbital of Fe lies around the Fermi level and hybridizes with the p orbitals perpendicular to the Cp rings that protude into the vacuum, enhancing the coupling with the tip orbitals. In contrast, for horizontal molecules, the p orbitals of the organic ring lie in a plane parallel to the surface and do not

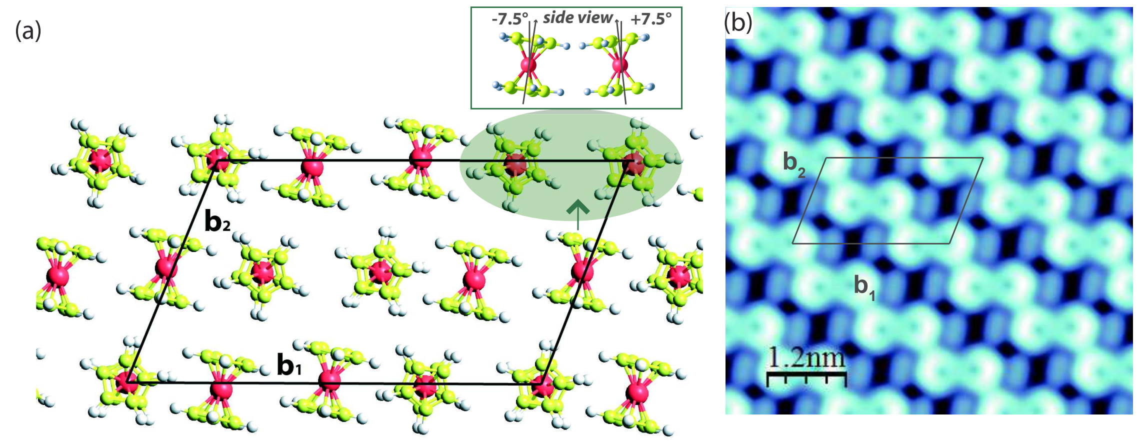

Figure 4.8: **Simulation of $FeCp_2$ zigzag network.** Relaxed zigzag structure on the Cu(111) surface. (a) top view, in which the side view of two vertical molecules is shown in order to present the tilt between them. Cu surface atoms have been omitted for simplicity. (b) Simulated STM topographic image using a bias of 1 V.

point towards the STM tip. Hence, the simulated apparent height of the vertical molecules is 0.5 Å larger, in agreement with the experimentally measured line profiles (Fig. 4.4a).

Our calculations also reproduce subtle effects revealed by STM images. We note a lateral displacement of 1.49 Å between consecutive vertical molecules in the a_2 direction (Fig. 4.7b), measured as the distance between Fe atoms, which is consistent with the experimental shift of 1.5 Å (Fig. 4.4a). Most importantly, we find that the slight asymmetry observed for the ring of the vertical molecules (Fig. 4.4b) results from a tilt between successive vertical molecules in the a_2 direction. This is a robust feature of the molecular layer as in our computation an initial configuration with no tilt always relaxes towards a tilted configuration. Such a tilt is due to the presence of the horizontal molecules. In particular, we found that the most stable situation is the one in which the horizontal molecules have two H atoms of each Cp ring pointing towards the surface, in this case this leaves a single H atom per Cp ring pointing into the vacuum. This configuration gives rise to a 18° tilt between consecutive vertical molecules along the a_2 direction (Fig. 4.7d).

Despite the displacement and tilt required by the network, the stability of the two-dimensional structure actually depends crucially on the combination of vertical and horizontal molecules having their Cp rings in eclipsed configuration (D_{5h} symmetry (Fig. 4.1b). Interestingly, this arrangement bears similarities with both the gas phase and the bulk structure of ferrocene. Similar to the ferrocene crystal (Fig. 4.7e), the presence of the two molecules, vertical and horizontal, ensures the cohesion of the crystal through T-shape interactions, but as in the gas phase—and unlike bulk ferrocene—the eclipsed configuration is favored over the staggered configuration (D_{5d}).

In order to understand the intermolecular interactions, the nature of the interaction between two type of $FeCp_2$ molecules was investigated. We found that the adsorption energy per molecule is 1.35 eV, where the contribution from the van der Waals (vdW) dispersion forces amounts to 1.05 eV. Comparing the adsorption energy of the layer not attributed to van der Waals interaction (0.30 eV) to the cohesion energy of the free-standing monolayer (0.48 eV), it can be concluded that the interaction between the molecules and the surface is due to vdW forces. The modest charge transfer per unit cell from the substrate to the molecules (0.11 e^-) points to molecules being physisorbed on the surface. Furthermore, when the layer is moved to different positions with respect to the Cu(111) surface (top, bridge, *hcp*, *fcc*) the energy cost is only of the order of 0.1 eV per unit cell confirming the little influence of the surface geometry on the molecular networks.

This conclusion is supported by the fact that the presence of the surface is not necessary to stabilize the molecular layer. Calculations of the unsupported monolayer show that the free-standing structure is stable, and presents the main features of the supported compact configuration, including the tilt of the vertical molecules. The (110) plane of pure ferrocene bulk (monoclinic phase P21/a) exhibits a very similar arrangement to the compact structure observed on the surface (Fig. 4.7e). This confirms that alternating orientations of ferrocene in networks are frequently encountered. However, it can be noticed that in the primitive cell observed and computed for the compact structure (Fig. 4.7b), adjacent eclipsed horizontal molecules are oriented differently, contrary to the unit cell of staggered ferrocenes shown by the bulk (Fig. 4.7e). This shows that the packing of ferrocenes in the molecular crystal has an influence on the relative orientation and configuration of the molecules. As in the crystalline structure, in this case we have also seen how the cohesion of the layer mainly comes from vdW interactions.

Zigzag configuration

Let us now consider the zigzag structure. The unit cell observed in the experiments corresponds, within the experimental accuracy, to a parallelogram on the Cu(111) surface (see parameters in Table 4.2). Due to the larger size of the unit cell when compared to the compact arrangement, we have just performed a few calculations to confirm the stability of the proposed structure. Fig. 4.8 shows the most stable structure that has been found after relaxation and the corresponding simulated topographic STM image, which reproduces with high accuracy the main features of the experimental image (Fig. 4.4c). This structure shares some common features with the compact one. First, the same reversal of the apparent height

Zig-zag network on Cu(111)	b_1 (Å)	b_2 (Å)	θ (deg)	
Experiment	23.0 ± 0.4	13.0 ± 0.4	71 ± 3	
Theory	23.15	13.37	68	
E_{ads}(eV)	E_{ads}^{vdW}	E_{coh}^{free}	q(e-)	d Å
1.26	1.02	0.43	0.18	2.4

Table 4.2: **Zig-zag ferrocene network parameters**, with same definitions as previous.

is observed, in which horizontal molecules always appear dimer in the images, although the highest atom of horizontal molecules in this case is placed 0.4 Å further from the surface than the topmost atom of the vertical ones. Second, we also find that four H atoms of the horizontal molecules have to point towards the surface in order to get a stable structure. Third, a tilt in two opposite directions is also observed for the vertical molecules (side view of Fig. 4.8a), even though it is slightly less pronounced (15°) than for the compact structure (18°). This explains the experimentally observed asymmetry between vertical molecules (Fig. 4.4d).

According to an analysis of the energetics of the zigzag configuration, the adsorption energy per molecule is 1.26 eV, of which 1.02 eV comes from the contribution of vdW forces. The interaction between the molecules and the copper surface is mainly related to vdW forces, as may be concluded after comparing these adsorption values with the cohesion energy of the free-standing monolayer (0.43 eV). There is a moderate charge transfer per unit cell (0.18 e^-) which is also indicating a weak molecule-substrate interaction. Therefore, we conclude that the molecules assembled in the zigzag configuration are physisorbed on the surface.The energetics of the adsorption of both, compact (table 4.1) and zigzag (table 4.2), configurations show that they are very similar, pointing in both cases to the same conclusion of a physisorbed layer.

4.2 Spin doping : inducing magnetism

This part describes a method to modify the structure and magnetic moment of ferrocene molecules by coupling them to a single transition metal atoms. Here, we present the results obtained by doping ferrocene molecules with Co adatoms.

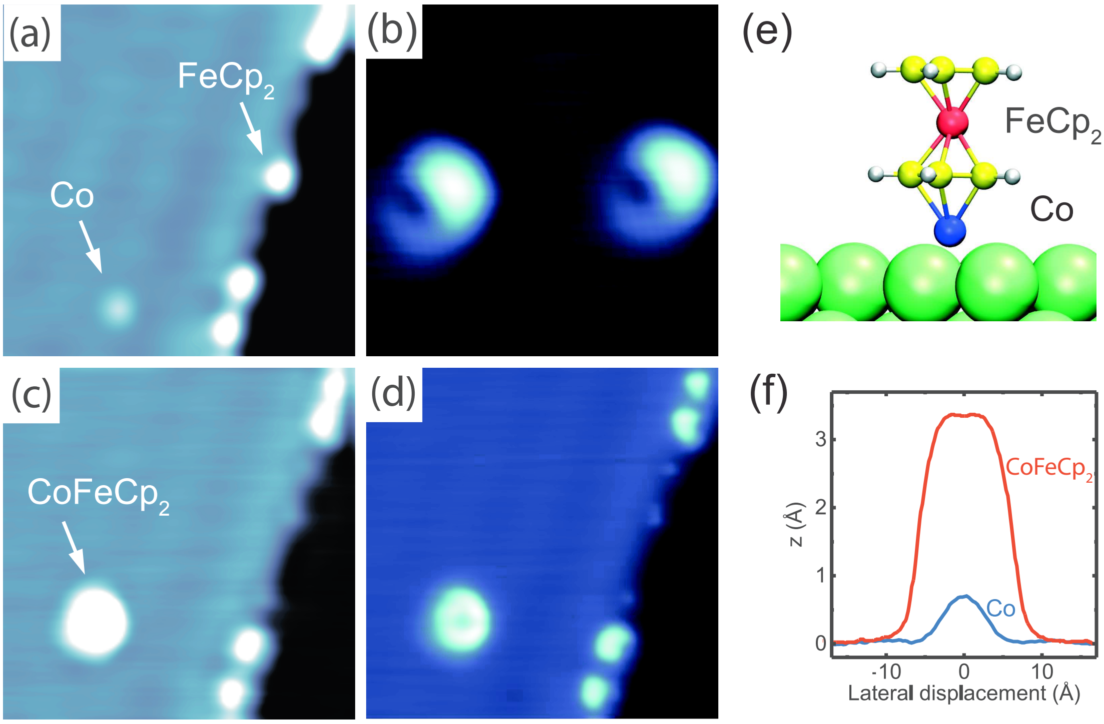

Figure 4.9: **Building process of an isolated $CoFeCp_2$.** (a) a $FeCp_2$ molecule at a step edge is picked up with the tip (image acquired with a tunneling bias: -1 V, current: 20 pA; image size: 7×7 nm^2), (b) the presence of $FeCp_2$ at the tip apex is asserted by imaging Co atoms (image acquired at -50 mV, 20 pA, 2.7×2.7 nm^2), which then exhibit a molecular pattern, (c) $FeCp_2$ is deposited on top of a Co atom by a tip-atom contact (image acquired at -1 V, 20 pA, 7×7 nm^2). (d) Same image as panel (c) but with a Laplacian filter applied in order to enhance the intramolecular contrast. (e) Chemical structure of $CoFeCp_2$; white, yellow, and red balls represent H, C, and Fe atoms of the $FeCp_2$ molecule respectively, and green balls represent the Cu atoms of the Cu(111) surface. (f) Line profiles of isolated Co and $CoFeCp_2$ on Cu(111).

4.2.1 STM investigation

In a first approach, we use a low ferrocene coverage, below 0.2 monolayers, to obtain step decoration only. The cobalt atoms are then evaporated on the cold substrate (4.4 K) to obtain a surface in which Co adatoms are located on the terraces (Fig. 4.9a).

The STM tip is then used as a tool to engineer isolated single $CoFeCp_2$ molecules, following the procedure displayed in Fig. 4.9a-d and described hereafter. The first step towards the formation of a new $CoFeCp_2$ molecule consists in positioning the tip on top of a single $FeCp_2$ molecule and approaching it while keeping the bias constant (-150 mV) until an abrupt drop is observed in the current. This jump in the current indicates that the molecule has been detached from the surface and is now attached to the tip [157], as revealed by the after-images shown in Figs. 4.9b-c. In Fig. 4.9b, a closer view of the Co atom imaged with the $FeCp_2$-terminated tip is shown. The Co atom, which is round when imaged with a metallic tip as in Fig. 4.9a, exhibits now a molecular pattern which corresponds to a *reverse* image of the molecular tip [158, 78, 159]. The ring-shape tip apex corresponds to a Cp ring of a tilted $FeCp_2$ molecule [160]. Placing this molecular tip on top of the Co atom and proceeding the same way, *i.e.*, decreasing the tip-sample distance until a certain threshold value, we are able to release the molecule from the tip. Fig. 4.9c shows how the targeted $FeCp_2$ molecule has disappeared from the step edge and that a new stable molecule, made up of Co-Cp-Fe-Cp (Fig.4.9e), has been created at the place where the isolated Co atom was located. The $CoFeCp_2$ molecule presents a ring-shaped feature (Fig. 4.9d). The corresponding apparent height profiles of an isolated Co atom and a $CoFeCp_2$ molecule, (0.7±0.1) Å and (3.4±0.2) Å respectively (Fig. 4.9f). This molecular building process is fully reproducible, and the upstanding geometry obtained for $CoFeCp_2$ on the surface is ideal for elaborating a single-molecule device, for example by a subsequent connection of the nanowire to a top electrode.

In order to experimentally confirm that a new molecule is formed, we move the whole $CoFeCp_2$ molecule by trapping it using a tip-induced local potential. The STM image (Fig.4.10a) reveals that when changing the tunneling current from 50 pA to 2 nA (at a constant bias of -30 mV) the $CoFeCp_2$ follows the tip movement and the image is then acquired by dragging the $CoFeCp_2$ across the Cu(111) surface. Atomic resolution of Cu(111) is obtained when $CoFeCp_2$ is dragged, supporting the idea a Co atom trapped under the ferrocene molecule and rastered over the surface with the STM tip [161]. As expected, a Cu-Cu distance of 2.5 Å is found. Once the current is set back to 50 pA the molecule is released. This supports the idea that $CoFeCp_2$ behaves as a unique entity, *i. e.*, the interaction between Co and $FeCp_2$ is strong enough to create a new molecular species. An isolated $CoFeCp_2$ is coupled stronger to the Cu surface compared to $FeCp_2$ because of the bonding through the Co atom.

Indeed, DFT calculations show that the role of the surface is to passivate the otherwise reactive $CoFeCp_2$ species. These calculations show that for ferrocene, binding through the Co atom is more stable by 0.8 eV (-1.86 eV compared to -1.06 eV) than having the Cp ring directly in contact with the substrate. Therefore, the surface stabilizes the $CoFeCp_2$, which results to be a molecular unit with a radical character, via passivation of the Co atom. We noticed from calculations that the molecule is found to be more stable when an extra Cp is added to form $CpCoFeCp_2$ [162], but no experimental data confirmed the existence of such a configuration. Table 4.3 summarizes the computed chemisorption properties of a Co atom

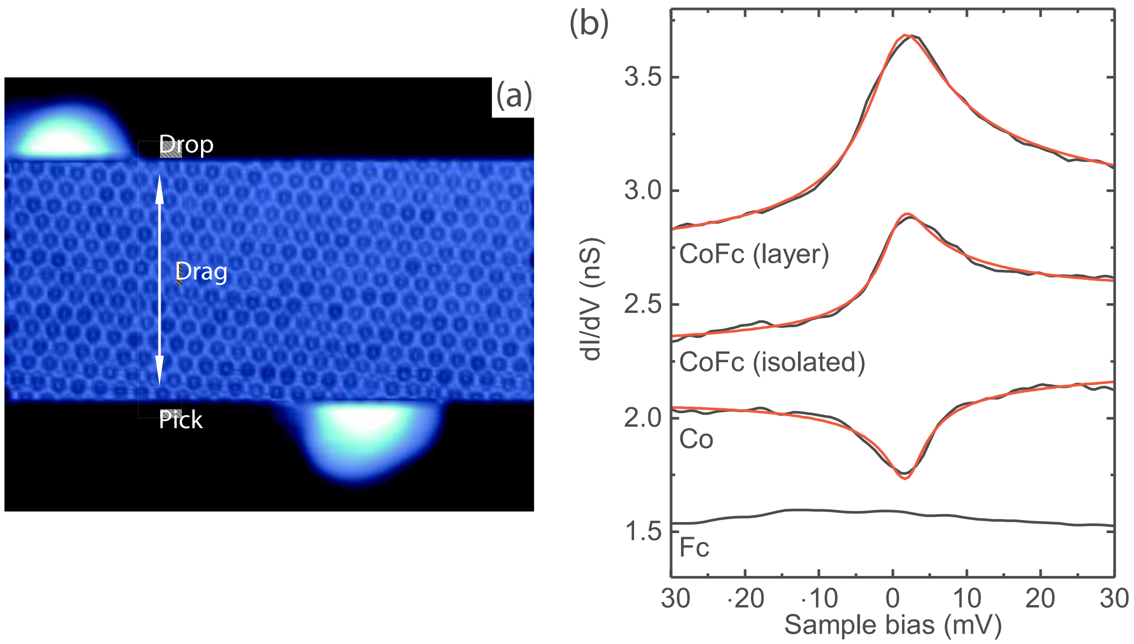

Figure 4.10: **CoFeCp$_2$ dragging on Cu(111).** (a) Image recorded during the process (image size: 6.5×5.2 nm^2). The dragging parameters are 2 nA and -30 mV. (b) dI/dV spectra including Frota-Fano fits (solid red-line) of isolated Co, FeCp$_2$, CoFeCp$_2$ and layer-integrated CoFeCp$_2$. The curves are shifted by 0 nS, 0.3 nS, 0.5 nS and -6.8 nS respectively. The feedback loop was opened at -0.03 V and 0.05 nA for all spectra, except for the the layer-integrated CoFeCp$_2$ were the feedback was opened at -0.05 V and 0.5 nA.

on an *fcc* site of the Cu(111) surface, and its evolution when a FeCp$_2$ molecule is placed on top the Co atom. The Co atom gives more electrons when the FeCp$_2$ molecule is placed on top describing a stronger binding of the Co atom. However, the adsorption geometry of the Co atom is basically unaltered.

The dI/dV spectra near the Fermi energy for isolated Co, FeCp$_2$ and CoFeCp$_2$, are shown in Fig.4.10b. While no spectroscopic feature is observed for FeCp$_2$ around zero bias, a peak is detected at the Fermi level for CoFeCp$_2$. Its narrow line shape suggests that it corresponds to a Kondo resonance, as evidenced for other organometallic molecules [26, 30]. The Kondo resonances exhibited by Co and CoFeCp$_2$ on Cu(111) are fitted using a Frota-Fano function [129, 128], as shown in Fig. 4.10(b). The line width of CoFeCp$_2$ yields a Kondo temperature of T_K=33±7 K, which is higher than that of an isolated Co atom (T_K=19±5 K).

The line shape evolution from a resonance to a dip (Fig.4.10a-b) is quantified by the difference in the Fano fitting parameter found for CoFeCp$_2$ (q=7) compared to Co (q=0.1). This is an indication that the tunneling paths involved in the Kondo effect have changed, the

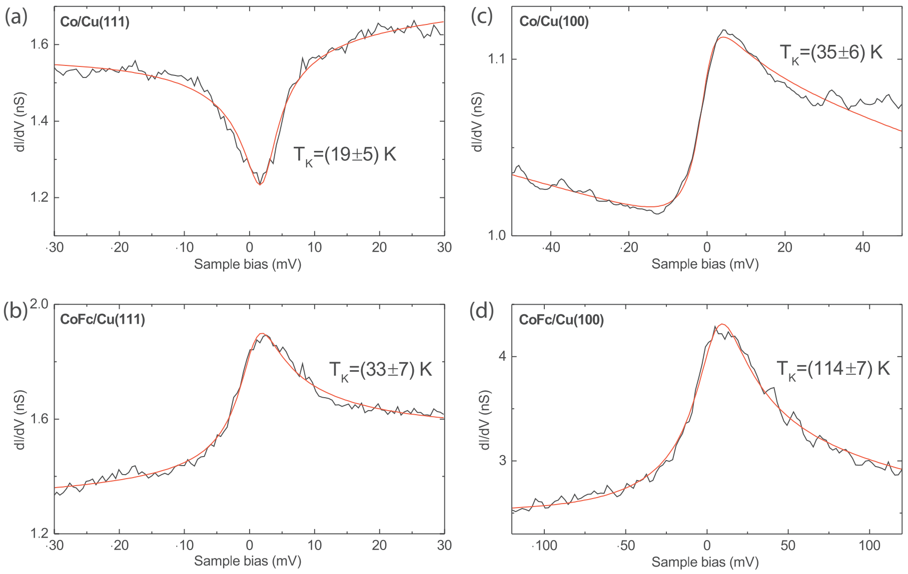

Figure 4.11: **Comparison of Co and $CoFeCp_2$ STS on Cu(100) and Cu(111).** The dI/dV spectra of Co and CoFc were acquired on Cu(111) and Cu(100). The solid red lines are Frota-Fano fits (see main text). The bottom panel presents a STM image of Cu(100) where CoFc molecules can be seen along with Co atoms and the Fc network (image size: 15×15 nm^2, 0.5 V, 0.2 nA).

tip being more coupled to the orbitals of the $CoFeCp_2$ molecule and more coupled to the conduction electron continuum for Co [118, 163, 124]. This is expected in view of the higher corrugation of $CoFeCp_2$ compared to Co atom on Cu(111), which places the tip further away from the surface and therefore weakens its coupling to the electron continuum of copper.

We compared the Kondo temperature of Co/Cu(111) and $CoFeCp_2$/Cu(111) (Fig. 4.11a-b) with Co/Cu(100) and $CoFeCp_2$/Cu(100) (Fig. 4.11c-d) to analyse the influence of the sample symmetry on the Kondo temperature. As expected [124, 120, 121], the difference in hybridization of the Co with the substrate yields different Kondo temperatures for $CoFeCp_2$ molecule and an isolated Co atom. On Cu(100) the Kondo temperature yields, respectively, 35±5 K for Co and 114±7 K for $CoFeCp_2$ (Fig.4.11). The different Kondo temperatures is linked to different couplings between $CoFeCp_2$ and copper depending on the symmetry of the crystal. This confirms the Kondo character of the resonance observed at Fermi level in STS spectra. The tip-assisted assembling process of a $CoFeCp_2$ is the same for both Cu(111) and Cu(100).

	d [Co-Cu] (Å)	μ [Co] (μ_B)	μ [Fe] (μ_B)	δ_N (e-)	E_B (eV)
Co	1.73	2.09	-	-0.16	-3.32
$CoFeCp_2$ (network)	1.70	1.33	0.12	-0.34	-4.04
$CoFeCp_2$ (isolated)	1.75	1.44	0.11	-0.34	-4.21

Table 4.3: **Charge transfert and spin doping parameters of $CoFeCp_2$**. d stands for different atomic distances, μ for the magnetization expressed in Bohr magneton (μ_B), δ_N for the amount of electrons transfered from the system to the surface and E_B refers to the binding energy of the Co atom to the different systems.

4.2.2 DFT analysis of isolated $CoFeCp_2$

The presence of a Kondo effect indicates that isolated $CoFeCp_2$ has a magnetic moment. DFT calculations show in particular that the Co atom loses electrons to the benefit of the Cu crystal and the Fe atom, see Table 4.4. Such an hybridization polarizes the Fe atom in the molecule and we found that the magnetic moment of the Co atom is strongly reduced when bound to $FeCp_2$ due to the increase of the d-shell occupation. In the isolated $CoFeCp_2$ molecule, the occupied peaks for the majority density of states (DOS) of Co shift to higher energies compared to an isolated Co. The majority spin DOS of the $FeCp_2$ splits, so that they can hybridize with splitted states coming from Co (Fig.4.12).

Similar changes occur for the minority spin. The transformation of the DOS due to the Co–$FeCp_2$ interaction, reveals the hybridization of the electronic structure forming a molecular unit and the partial depletion of Co levels leading to a reduction of the magnetic moment. In the $CoFeCp_2$ molecule adsorbed on surface, the computed magnetic moment of the Co atom is in fact 1.44 μ_B (see Table 4.3), which is much higher than the magnetic moment of Fe in the same molecule (0.12 μ_B). The magnetic moment of Co on Cu(111) is in contrast 2.09 μ_B, which shows that after the formation of $CoFeCp_2$, the Co atom undergoes a transition from $S \approx 1$ to $S \approx 1/2$ revealing the above changes in electronic structure. There is a ferromagnetic (FM) coupling between the Fe and Co atoms of $CoFeCp_2$, which is also apparent in the spin density of the molecule (Fig. 4.12b); moreover the Co–Fe hybridization leads to peaks in the DOS projection on Co atom that coincide in energy with peaks of the Fe atom (Fig. 4.12a). Gas phase calculations of $CoFeCp_2$ show that the FM solution is 98 meV more stable than the antiferromagnetic (broken symmetry) one. The Kondo effect of $CoFeCp_2$ and of isolated Co are therefore different, in agreement with the measured spectral signatures of T_K.

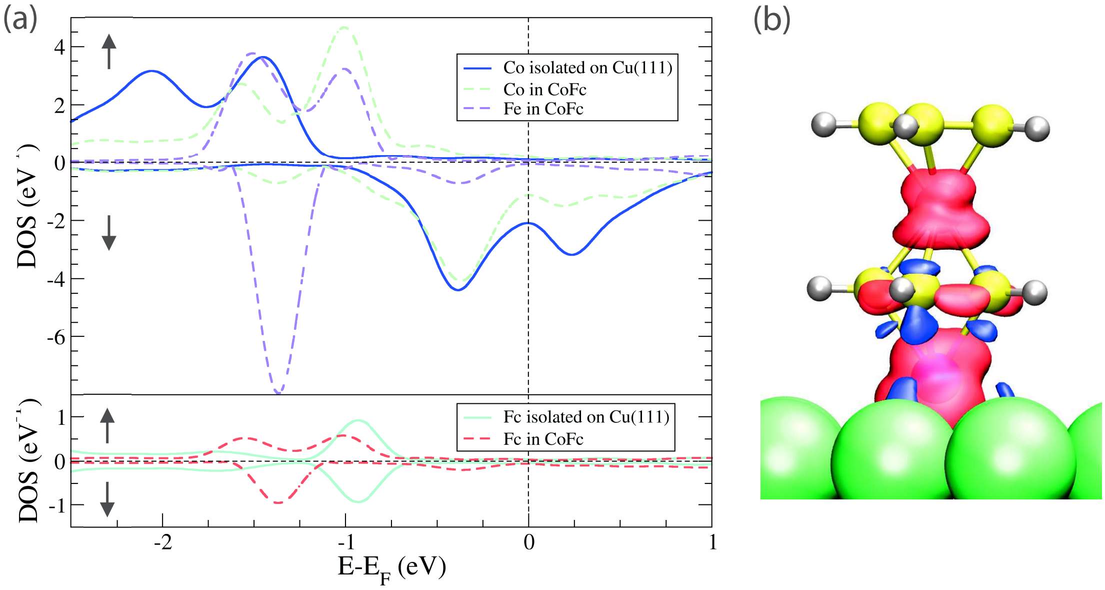

Figure 4.12: **Calculated DOS and spin density of $CoFeCp_2$ on Cu(111).** (a) Calculated DOS projected on different atoms of the $CoFeCp_2$ molecule (up arrow: majority DOS; down arrow: minority DOS). The dashed lines correspond to the DOS projected onto Co (green), Fe (magenta), and $FeCp_2$ (red) when they are part of the new $CoFeCp_2$ molecule.The solid lines show the DOS for Co in the absence of $FeCp_2$ (*i.e.* isolated Co) and for $FeCp_2$ in the absence of Co (*i.e.* isolated $FeCp_2$). (b) Spin density for a $CoFeCp_2$ molecule at the Fermi level (majority spin: red; minority spin: blue).

4.2.3 $CoFeCp_2$ in molecular networks

A different procedure to form the same $CoFeCp_2$ molecule is found when increasing the amount of deposited molecules on the surface and sublimating Co atoms afterwards. In this case, we can obtain a spontaneous on-surface reaction of cobalt atoms with a molecular layer of ferrocene. A Co coverage above 0.35 ML starts degrading the ferrocene layer. This is due to the lattice mismatch between the adsorption site of Co adatoms and the distance between vertical molecules in the networks. Thus, we limited ourselves to a low coverage regime for the following experiments. Fig. 4.13a shows densely-packed two dimensional $FeCp_2$ islands after exposure to a small amount of Co atoms (0.05 ML).There is no significant difference between both network configurations regarding the adsorption of the Co atoms. Hence, in the following we will only focus on the compact arrangement on Cu(111).

Adsorbed $CoFeCp_2$ molecules appear as bright protrusions in the molecular layer with an apparent height of (0.7±0.1) Å with respect to vertical $FeCp_2$ molecules and (3.7±0.2) Å compared to Cu(111), as deduced from the line profile along the dashed line displayed

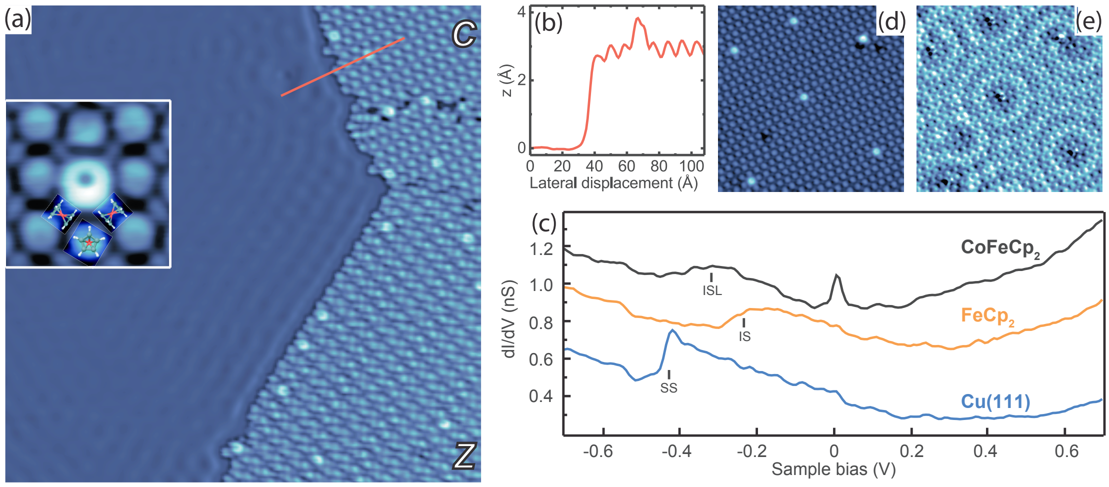

Figure 4.13: **CoFeCp$_2$ imbedded in ferrocene networks studied by STM.** (a) Self-assembly of FeCp$_2$ on Cu(111) (-0.05 V, 0.5 nA,35×35 nm^2). The compact and zigzag arrangements are denoted C and Z, respectively. The bright spots reveal the presence of Co on the molecular layer. Inset: Close up view of the CoFeCp$_2$ integrated in the compact configuration. A FeCp$_2$ model structure is superimposed on the image to highlight the adsorption geometry of the ferrocene layer. Note that the Co deposition in panel (a) was done at 77 K, as a consequence the Co atoms on copper have diffused to the step edges. (b) Line profile along the red dashed line shown in (a). (c) dI/dV spectra of Cu(111), FeCp$_2$ and CoFeCp$_2$. The curves are shifted by 0 nS, 0.3 nS and 0.5 nS respectively (feedback loop opened at -1 V and 0.5 nA). (d) CoFeCp$_2$ image and (e) corresponding constant-current dI/dV map (-0.1 V, 0.5 nA, 20×20 nm^2).

in Fig. 4.13b. After a careful inspection of the surface, it can be unambiguously concluded that Co atoms are exclusively adsorbed at the sites of vertically oriented ferrocenes. A closer view into the molecular layer (inset of Fig. 4.13a) shows that a new molecule is formed upon Co adsorption, which appears as a ring with a pronounced asymmetry.

To see whether there is any difference between the isolated and the layer-integrated CoFeCp$_2$, the electronic properties of the latter one have also been investigated. The dI/dV spectra of Cu(111), FeCp$_2$ and CoFeCp$_2$ are displayed in Fig.4.13c. The onset of the Shockley surface state (noted SS in Fig. 4.13c) of Cu(111) can be easily identified at -0.44 eV; for the physisorbed ferrocene layer, this state is transformed into an interface state (noted IS) with an onset around -0.26 eV [145].The scattering of the interface state of the CoFeCp$_2$ (Fig. 4.13d-e) reveals a different coupling of CoFeCp$_2$ and FeCp$_2$ with the substrate. In fact, in the dI/dV spectrum of CoFeCp$_2$ a broad resonance is observed around -0.35 V, which corresponds to a localization of the interface state (noted ISL) [163, 164, 72, 165]. More noticeable is the narrow peak detected near zero bias, which as in the previous case can be

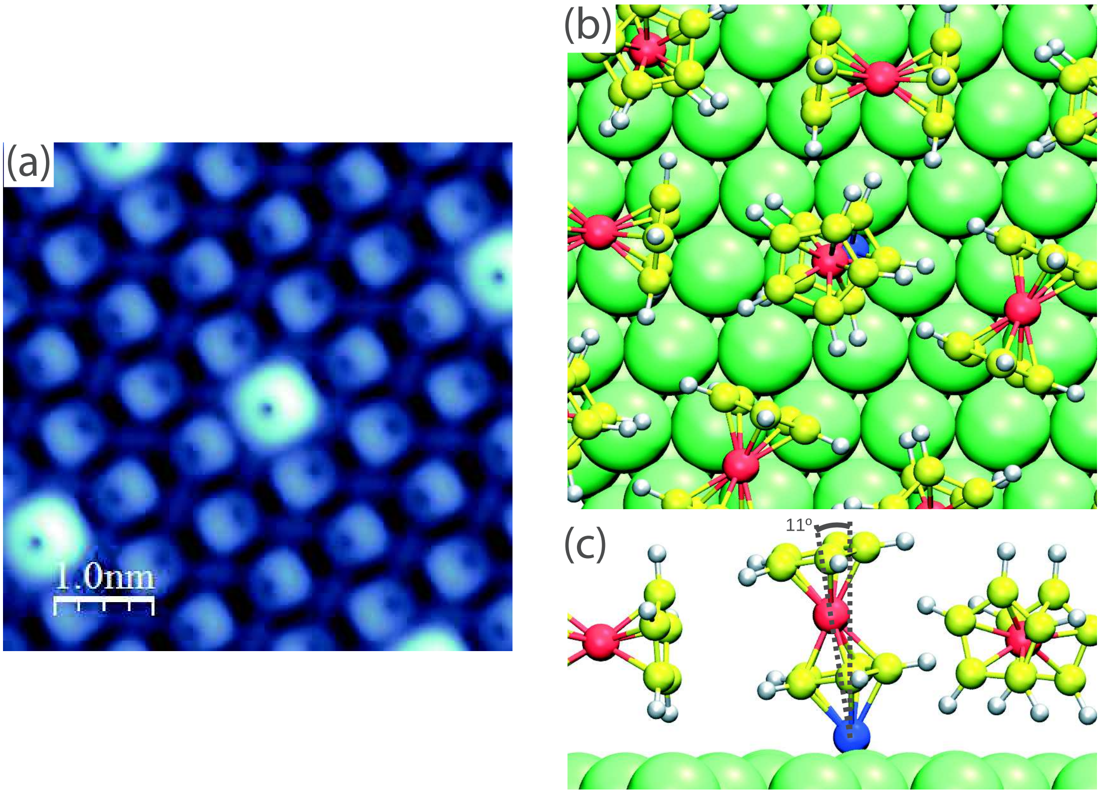

Figure 4.14: **Simulation of $CoFeCp_2$ formation.** (a) Simulated STM image integrating the local density of states 1 eV above the Fermi energy. The unit cell of the calculation contains a single Co atom per 12 vertically standing $FeCp_2$ molecules. (b-c) Top- and side-view scheme of the compact arrangement with a single Co atom giving rise to a single $CoFeCp_2$ molecule in the unit cell. For clarity only molecules in the middle row of the top view are shown in the side view.

referred to the Kondo effect presented by $CoFeCp_2$. The resonance is again fitted using a Frota-Fano function (Fig. 4.10b), from which we obtain T_K=(38±6) K and q=6. Compared to the results obtained for the isolated $CoFeCp_2$ we see that both molecules, isolated and layer-integrated, present an experimentally indistinguishable electronic and magnetic behavior with a Co atom placed between the molecule and the copper surface.

To confirm this experimental observation, we performed DFT calculations. We compared the stability of Co + $FeCp_2$ systems on Cu(100) subtrate by varying the relative position of Co with respect to $FeCp_2$ (Co on top of the molecule, below the molecule, aside the molecule, ...) and the different position of the anchoring species on the crystal possible adsorption sites. From total-energy calculations we conclude that Co atoms prefer to be on an *fcc* position with respect to the Cu substrate and below $FeCp_2$, *i.e.* in direct contact with the Cu(111)

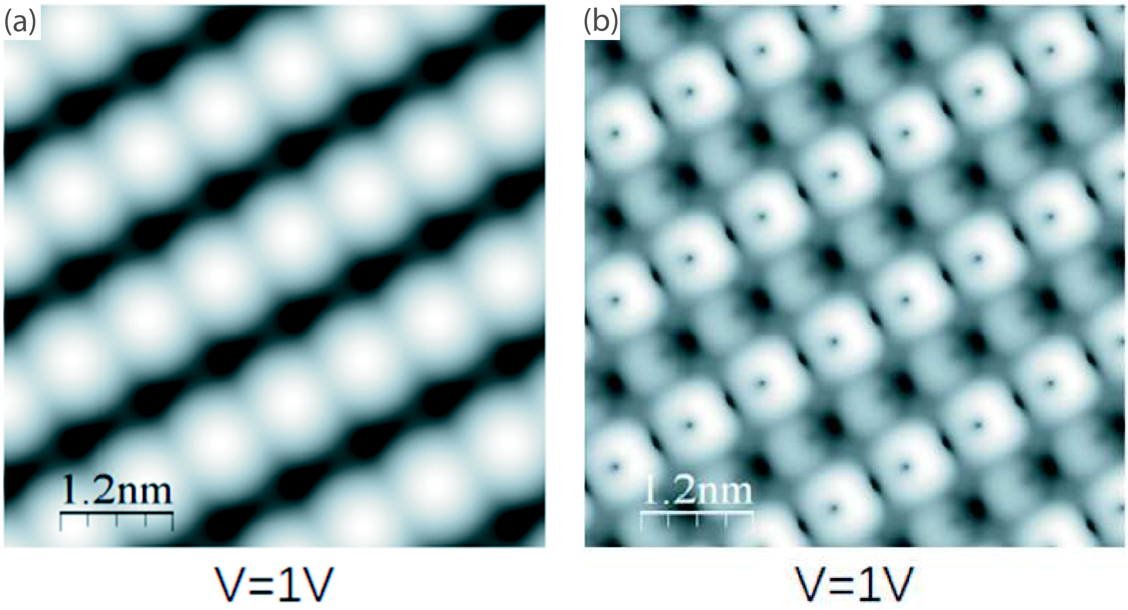

Figure 4.15: **Co adsorption on $FeCp_2$ networks possibilites models.** (a) Simulated STM image obtained when all vertical $FeCp_2$ of a compact network are topped with Co atoms. The apparent shape of such a $CoFeCp_2$ appears round whereas the experimental picture displays a ring shaped protusion. (b) Simulated STM picture of a compact network with Co atoms placed under each vertical molecules. The apparent ring shape corresponds to the experimentals observations.

surface as shown in Figs.4.14(b-c). This conformation is 3 eV more stable than the one with Co on top of ferrocene.

The simulated STM topographic image (Fig.4.14a), obtained by applying the Tersoff and Hamann theory [61, 62] using the method described by Bocquet and coworkers [166], shows how a compact molecular layer would look like if we had several $CoFeCp_2$ molecules integrated in the ferrocene layer. The ring-like brightest protrusions correspond to $CoFeCp_2$ and the dimer ones to $FeCp_2$. Horizontal molecules are observed as rod-like features between the vertical ones. The striking agreement between simulated and experimental STM images of the $CoFeCp_2$ allows assigning the bright ring-like shape in the images to the top Cp ring of the $CoFeCp_2$ molecule. This ring is moreover tilted approximately by 11° with respect to the surface normal (Fig.4.14c) due to the packing of the molecules [160]. Note that if the Co atom were on top the $FeCp_2$ molecule, according to simulated images (Fig. 4.15) no ring-like shape would be observed in the STM images.

The computed adsorption properties given in Table 4.3 also show a small variation when going from the isolated $CoFeCp_2$ to the monolayer. The Co atom better stabilizes

	μ (single entity on metal surface)	μ ($CoFeCp_2$ complex)	Charge transfer ($CoFeCp_2$ complex)
Co	2.09 μ_B	1.18 μ_B	- 0.26 e^-
$FeCp_2$ (Fe atom)	0 μ_B	0.11 μ_B	+ 0.1 e^-
Cu (crystal)	-	-	+ 0.16 e^-

Table 4.4: **Comparison of magnetic momenta between isolated $CoFeCp_2$ and same molecule in a molecular network**. μ stands for different the magnetic moment and μ_B refers to the Bohr magneton.

the new entity in the monolayer (5% lower binding energy). As a consequence, the Co atom approaches the $FeCp_2$ molecule and separates from the Cu (111) surface by 0.05 Å. However, both magnetic moment and charge transfer are similar for the isolated and the monolayer case, showing the calculated DOS a negligible downshift of the Co peaks when going into the monolayer case. Hence, DFT results show that as in the experiment, isolated and layer-integrated cases present a very similar electronic and magnetic behavior, with a magnetization of the iron atom by charge transfer. This indicates that the coupling of the molecule with the substrate is similar in both cases and that the neighboring ferrocenes around $CoFeCp_2$ in the layer do not interact strongly, leaving their electronic properties mostly unchanged.

The experiments and computations of this chapter showed an associative adsorption of ferrocene on copper crystals. Depending on the deposited amount, the isolated ferrocene molecules either move to the edges of the copper steps or form self-assembled networks with two equiprobable patterns both based on alternating horizontal and vertical molecules. The adsorption energy is mainly due to Van der Waals interaction and indicates a physisorption of the molecules on the sample. We have then demonstrated that it is possible to build new customized ferrocene-based molecules in a controlled way via STM manipulation and that the same molecule is formed spontaneously by atomic doping of a ferrocene layer, highlighting the stability of this molecule. In particular, we have shown that $CoFeCp_2$ exhibits a magnetic behavior, as revealed by the observed Kondo resonance. These result can be generalized to other atoms and metallocene molecules, opening a path to create and study a new family of metallocene nanowires coupled to metal electrodes.

Chapter 5

Enhanced spin-flip excitations in nickelocene

Recent advances in addressing and controlling the spin states of a surface-supported object –atom or molecule– have further accredited the prospect of quantum computing [167, 168] and of an ultimate data-storage capacity [169]. Information encoding requires that the object must possess stable magnetic states, in particular magnetic anisotropy to yield distinct spin-dependent states in the absence of a magnetic field together with long magnetic relaxation times [170–172, 96]. Scanning probe techniques have shown that inelastic electron tunneling spectroscopy (IETS) within the junction of a scanning tunneling microscope is a good starting point to study the stability of these spin states. STM-IETS allows for an all-electrical characterization of these states by promoting and detecting spin-flip excitations within the object of interest [4, 5, 101, 97, 173, 174]. It can also provide an electrical control over these states [175], simplifying the information readout process. As spin excitations need however to be preserved from scattering events with itinerant electrons, single objects are usually placed on non-metallic surfaces such as thin-insulating layers [176, 172, 177, 96] or superconductors [29].

In this sense, new approaches to improve the detection of spin-flip excitations are desirable. One possibility we explore in this chapter is the molecular functionalization of the STM tip. Organic molecules have been used in scanning probe techniques to functionalize tips with the purpose of obtaining high-resolution images [178–181] and, more recently, to improve the detection of molecular vibrations [182]. We use in this chapter a similar approach to boost the spin-sensitivity of an IETS measurement by exploiting the spin-flip excitations exhibited by a simple double-decker molecule, nickelocene ($NiCp_2$), attached to the tip. Prior to this study, however, we must investigate how nickelocene interacts with a metal. Regarding the adsorption of $NiCp_2$ on metallic surfaces, few nanoscale results can be found, and most investigations of nickelocene deposition on surfaces were macroscopic studies. A study of $NiCp_2$ adsorption with Angle Resolved Photon Emission Spectroscopy (ARPES) [183] has suggested a weak chemisorption of canted-oriented nickelocene molecules on Ag(100) at low temperature (130 K). The molecules appear to be preserved and a desorption temperature of 212 K was recorded. A study focusing on the desorption process [184] identified instead organic residues after a thermal desorption at 212 K on the same substrate, evidencing a degradation of the molecule. A later study by photolysis [185] suggested two adsorption possibilities on Ag(100): a vertical molecule and a canted-oriented one. All these studies call for an atomic scale study to clarify the interaction between nickelocene and metallic surfaces.

This chapter is organized in three different parts. We will first present how $NiCp_2$ molecules adsorb in two different surfaces Cu(100) and Cu(111), and show how the gas phase properties of $NiCp_2$ are mainly preserved when adsorbed on such metallic substrates. Then we will investigate the magnetic properties of $NiCp_2$ on these surfaces by means of IETS and XMCD. We will see that the molecules exhibit an inelastic excitation due to the presence of magnetic anisotropy. Finally, by attaching a nickelocene to the tip apex of a STM, we will show that two spin-flip excitations can be sequentially triggered, resulting in a large enhancement of the inelastic signal as illustrated by the IETS acquired above a surface-supported $NiCp_2$ molecule. This unique situation can be achieved due to the chemical stability, the presence of magnetic anisotropy and full preservation of the $NiCp_2$ spin on the tip apex (or more generally in a metallic environment) and the extremely efficient spin inelastic effect exhibited by this molecule.

5.1 Nickelocene deposition and adsorption on copper surfaces

The $NiCp_2$ molecular deposition was performed following the same method as for ferrocene, with molecules that sublimate under vacuum conditions. In this case however, the $NiCp_2$ molecules were purified in vacuum for approximately 12 hours to reach 10^{-6} mbar before the deposition to prevent impurities from being adsorbed on the sample. The deposition was performed through a valve onto cold (below 100 K) copper crystals and the sample was then directly inserted in the low temperature STM stage (4.4 K).

5.1.1 Deposition on Cu(100)

$NiCp_2$ can adsorb on copper surfaces as isolated molecules or self-assembled monolayers (Fig. 5.1), depending on the molecular coverage and deposition conditions. Since DFT

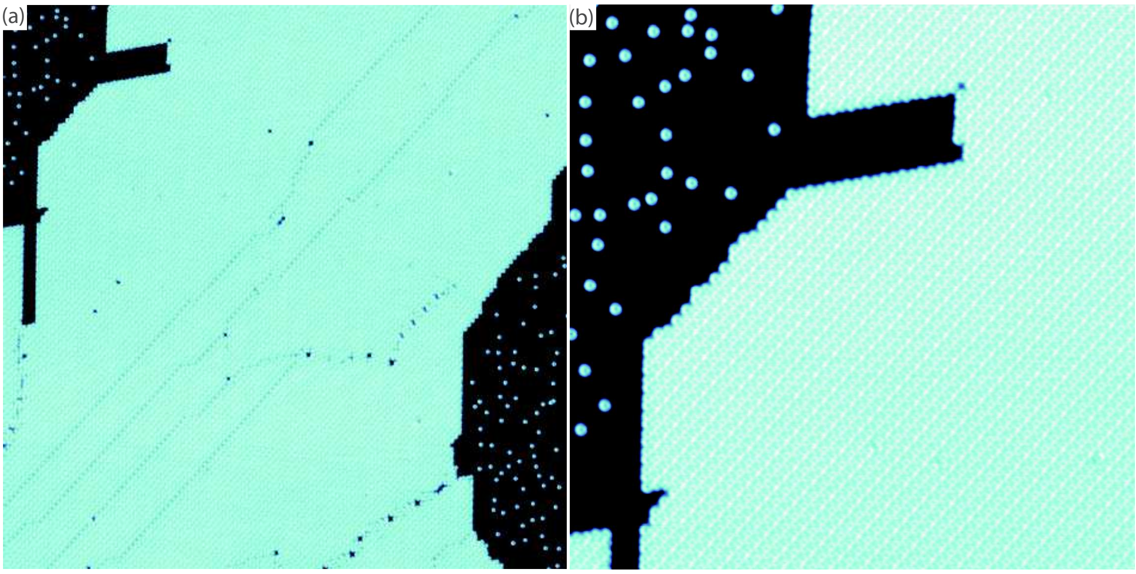

Figure 5.1: **Nickelocene adsorption on Cu(100).** (a) Self-assembled layer (paired confguration) and isolated NiCp$_2$ on Cu(100) (image size: 50×50nm^2, sample bias: 20 mV, tunneling current: 50 pA). (b) zoom on the top left corner of the same area (20×20nm^2).

calculations have been performed for Cu(100), we will mainly present in this chapter the detailed results on this surface. First, we will analyze the adsorption of isolated molecules and afterwards we will carefully inspect each of the networks observed in the copper surfaces.

Isolated NiCp$_2$

Fig 5.2 shows a Cu(100) surface with a molecular coverage of 0.045 monolayer. Such a low amount of molecules does not enable layers to form, so the surface is occupied by isolated NiCp$_2$. From the STM images we can clearly distinguish ring-like shape features which correspond to NiCp$_2$ vertical molecules, *i.e.* molecules adsorbed with one Cp ring facing the sample surface and the other one facing the vacuum. The line profile of an isolated nickelocene (Fig. 5.2b-c), reveals that the apparent height of the molecule is 3.5 ± 0.1 Å.

In order to experimentally determine the adsorption site of those isolated molecules, we compared the NiCp$_2$ position to the already-known location of adsorbed Cu adatoms (hollow position). We deposited Cu atoms directly from the Cu coated tip (Fig. 5.2d). The crystal orientation was obtained by contact measurements on a small area as presented in the inset. From the STM images, it appears that the molecule is adsorbed on a hollow site of the copper crystal.

The preferential adsorption of NiCp$_2$ in a hollow position of the Cu(100) surface, was confirmed by DFT calculations (Fig. 5.3a). The eclipsed symmetry was found to be the more

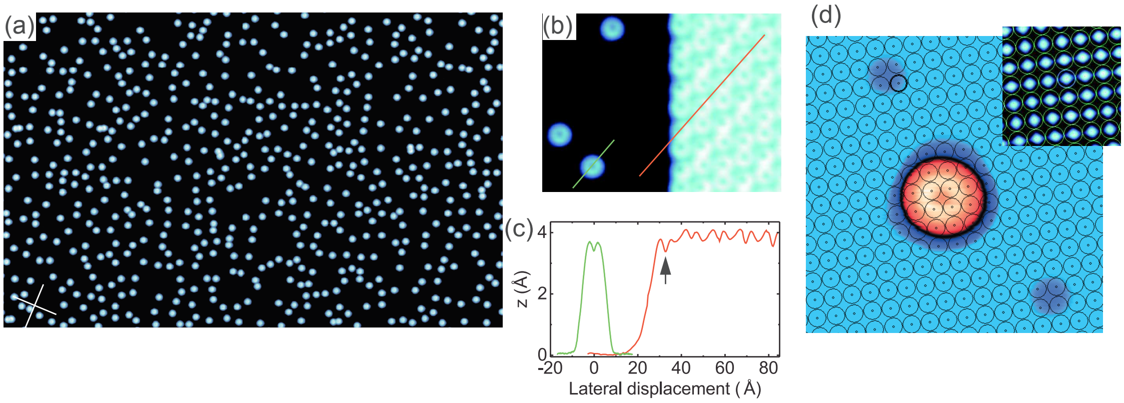

Figure 5.2: **STM images of isolated nickelocene on Cu(100).** (a) Large area with isolated molecules only (650 × 1000 $Å^2$, 10 mV, 50 pA). The white cross indicates the crystallographic directions of the Cu(100) surface. (c) Height profiles of both isolated and layer of isolated $NiCp_2$. The profiles are acquired along the dashed lines indicated in (b). The arrow in (c) highlights a $NiCp_2$ molecule at the edge of the layer. (d) STM image of isolated $NiCp_2$ (40 × 40 $Å^2$, 20 mV, 50 pA) and simulated (100) lattice revealing the adsorption of nickelocene. Two Cu atoms are also visible. Inset: Image of the Cu(100) surface obtained by a tip-assisted manipulation of a Cu atom on a pristine area of the surface (16.5 × 16.5 $Å^2$, 10 mV, 80 nA). The copper lattice parameter is 2.52 Å.

distances (Å)	$NiCp_2$ /Cu(100)	$FeCp_2$ /Cu(100)	$NiCp_2$ (gas phase)
z_{text1}	1.77	1.64	1.79
z_{text2}	1.78	1.62	1.81
z_{text3}	2.35	3.15	-

Table 5.1: **Distances between different parts of the nickelocene and sample surface**, as labelled in Fig. 5.3a.

stable by 23 meV per molecule with respect to the staggered configuration. Furthermore, the adsorption distance is lower than what we obtain for the layers. Details of the bonding distances are given in Table 5.1. The molecules appear to be moderately chemically adsorbed with an adsorption energy E_{ads} defined as

$$E_{ads} = E_{fullsystem} - E_{molecule} - E_{surface} \tag{5.1}$$

and estimated between -0.93 meV (PBE approximation) and -1.33 meV (DFT-D2 method) per molecule.

The computations also provided a projected Density of States of the single $NiCp_2$ adsorbed on Cu(100) (Fig. 5.3b). The shaded light-grey area corresponds to the sum of the *s*,

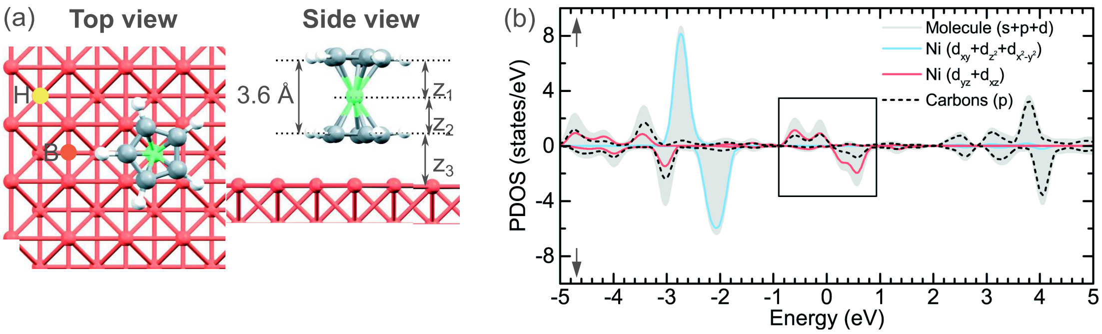

Figure 5.3: **DFT results for the adorption of isolated nickelocenes on Cu(100).** (a) Top and side view of structural model of eclipsed $NiCp_2$ on Cu(100) (green: Ni, grey: C, white: H). Top (T), bridge (B) and hollow (H) adsorption sites are depicted in the top view image. (b) Projected density of states (PDOS) of $NiCp_2$ onto different molecular and atomic orbitals (up arrow: majority spins; down arrow: minority spins). The light-grey area corresponds to the entire molecule projected on s, p and d orbitals. The nickel d orbital is grouped as $d_{yz}+d_{xz}$ (solid red line) and as $d_{xy}+d_{z^2}+d_{x^2-y^2}$ (solid blue line). The dashed black line corresponds to the contribution of all p carbon orbitals. The box between -1 and 1 eV shows the spin-polarized LUMO.

p and d orbitals of the entire molecule, whereas the red line groups d_{yz} and d_{xz} and the blue line considers d_{xy}, d_{z^2} and $d_{x^2-y^2}$.

The lowest unoccupied molecular orbital of $NiCp_2$ (LUMO; box in Fig. 5.3b) can be qualitatively represented by the mixing of C and Ni contributions placed around the Fermi level and is clearly spin polarized, giving a magnetic character to the molecule. The rest of the Ni(3d) shell (blue line) is occupied and does not contribute to the magnetism of the molecule because both up and down spin states are below the Fermi level. The magnetic moment of $NiCp_2$ amounts to 1.96 μ_B (1.18 μ_B for the nickel atom) and is practically unchanged compared to the gas phase (2 μ_B). Upon adsorption, the magnetic moment of nickelocene is preserved ($S \approx 1$) and the electronic structure corresponds to the schematic picture given for the gas phase molecule in Fig. 5.8.

$NiCp_2$ networks

Nickelocene adsorbs associatively forming two different self-assembled $NiCp_2$ networks called "paired" and "compact" that coexist equiprobably on Cu(100). We have investigated and characterized both $NiCp_2$ networks with the support of DFT computations, and compared these results to the ones previously obtained for ferrocene.

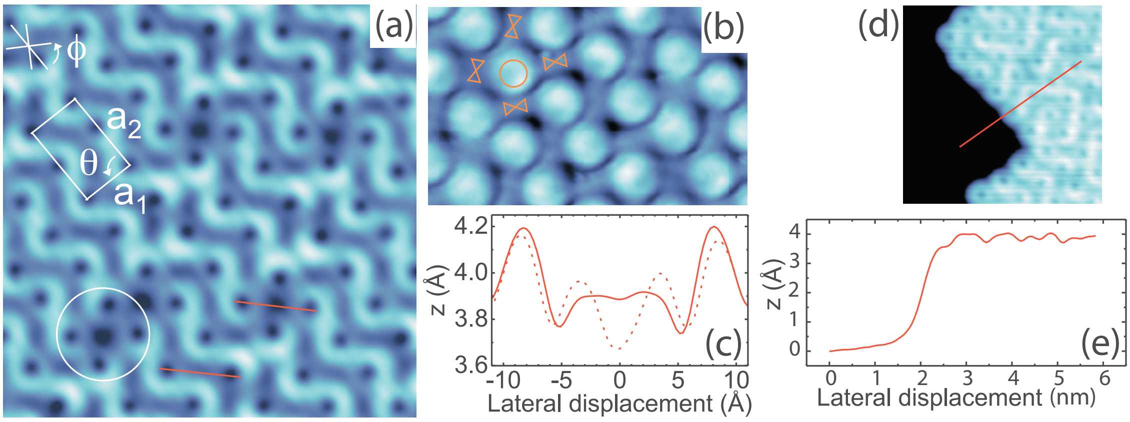

Figure 5.4: **STM image of the compact layer on Cu(100).** (a) STM image of the compact layer (70 × 70 Å^2, 20 mV, 20 pA). The unit cell is shown by a solid white solid line. The layer is tilted by an angle ϕ relative to the crystallographic directions of Cu(100), which is depicted by a cross int the top left corner. The dashed circle highlights a defect in the compact layer. (b) Image of the compact layer acquired with a low tunneling bias (28 $\times$ 46 Å^2, 1 mV, 10 pA). The molecular arrangement is sketched in orange. (c) Corrugation profiles acquired in compact network. (d) STM image of the edge of a compact network image at 20 mV. (e) Height profile of the edge of the compact network. The apparent height is about 3.5 Å.

Compact network. The first type of self-assembly observed on Cu(100) is very similar to the compact network of ferrocene, as can be seen in the closer view STM images (Fig. 5.4a-b). The vertical molecules can be straightfowardly identified as bright circles.

The [010] and [001] directions of the Cu(100) surface are given by the white cross in the top left corner of the image, indicating that the molecular network does not follow the crystal symmetry. Four possible orientations of the molecular layer relative to the crystal orientation underneath can be found with angles $\psi = 53 \pm 3°$, an angle $-\psi$, $90° + \psi$ and $90° - \psi$. The parameters of the rectangular unit cell of the molecular assembly (marked in white in Fig. 5.4a) were estimated to be $a_1 = 8.8 \pm 0.4$ Å and $a_2 = 15.1 \pm 0.5$ Å with an angle $\theta = 90 \pm 2°$ from the experimental images. Such values are very similar to measurements performed on ferrocene, as shown in Table 5.2.

The fact that the intermolecular arrangement is so similar to that encountered for ferrocene, where horizontal and vertical molecules are present in the layer, suggests that horizontal $NiCp_2$ molecules are also present in this case. The detection of horizontal nickelocenes is however experimentally demanding. To visualize them, we acquired low-bias images (Fig. 5.4b) in order to improve the corrugation of the image. This way, we are able to distinguish some features between vertical molecules, which we identify as horizontal

compact	a_1 (Å)	a_1 (Å)	θ (deg)
$NiCp_2$/Cu(100)	8.8 ± 0.4	15.1 ± 0.5	90 ± 2
$FeCp_2$/Cu(111)	8.9 ± 0.3	15.5 ± 0.3	90 ± 3

Table 5.2: **Comparison between the unit cells parameters of the compact networks of $NiCp_2$ and $FeCp_2$.**

molecules. The mechanism responsible for such a corrugation change with bias will be explained later in this chapter. The horizontal molecules are imaged as elongated rod-like protrusions flanking $NiCp_2$ vertical molecules and are aligned in alternated directions. The presence of horizontal molecules can be also inferred from the asymmetry of the ring brightness of vertical molecules that reflects that there is a small tilt of the molecular axis with respect to the surface normal. This tilt appears due to the presence of the horizontal molecules in between vertical molecules.

There are a total of 4 molecules, 2 horizontal and 2 vertical ones, per unit cell and the packing density is 0.030 molecules per Å^2, which is remarkably close to the packing density of found for the same assembly with ferrocene molecules (0.029 molecules per Å^2). Taking into account the similarity of this network with the results obtained on ferrocene, we can already state that the $NiCp_2$ layer is stabilized by T-shape van der Waals interactions between horizontal and vertical molecules.

The compact assembly of nickelocene exhibits a maximum corrugation of 0.5 Å (Fig. 5.4c), different from ferrocene networks (0.1 Å) and the layer has an average height of 4.0 ± 0.2 Å with respect to the Cu(100) surface (Fig. 5.4e). However, the molecules at the edges of the network exhibit a lower apparent height of 3.5 ± 0.1 Å, the same as isolated $NiCp_2$. This 0.5 Å difference between the layer and the edge molecules of the network is attributed to the fewer horizontal neighbours at the edges pushing up the vertical molecules.

In order to study the stability of the structures proposed for the molecular layer on Cu(100), we have performed extensive DFT+D2 calculations. They show that, while the carbon-surface distance for $NiCp_2$ is shorter than for $FeCp_2$, the compact structure is strictly analogous to the one we previously proposed for ferrocene on Cu(111). The adsorption energy for the molecular layer is 1.49 eV, close to the 1.35 eV and 1.26 eV found for the ferrocene networks.

The compact network presents sparse defects that are imaged as dim spots in the layer (highlighted by a dashed circle in Fig. 5.4a). The profiles taken around such defects (dashed line in profile in Fig. 5.4c), show a 0.2 Å corrugation which is not matching with artificially created molecule vacancies (1.5 Å corrugation). We can therefore exclude that they correspond to a missing horizontal molecule. The exact nature of these defects is still unclear and will need further work to be determined.

Paired network. As the compact assemblies, the paired network on Cu(100) (Fig. 5.5a) can be found forming 4 possible angles, $\psi = 53 \pm 3^\circ$, an angle $-\psi$, $90^\circ + \psi$ and $90^\circ - \psi$, with respect the Cu(100) orientation. In the paired layer, vertical $NiCp_2$ molecules are arranged following dimer-like pairs with variable $NiCp_2$-$NiCp_2$ spacing. We identified two kinds of pairs of vertical molecules organized in alternating rows (evidenced in Fig. 5.5a by continuous and dashed line profiles). The spacing between paired molecules is evaluated as 7.9 ± 0.3 Å for the first kind of pair (continuous line profile) and 6.5 ± 0.3 Å for the second one (dashed line profile). The distance between two pairs is 9.0 ± 0.3 Å. The corrugation is at most 0.6 Å, but some differences are evident among the two type of pairs. In the pairs with the smallest $NiCp_2$-$NiCp_2$ spacing, the ring-like protrusion of the Cp rings has nearly same corrugation. The molecules are practically vertical and, therefore, in a configuration similar to that of isolated molecules. On the contrary, for larger $NiCp_2$-$NiCp_2$ spacing, the corrugation increases by 0.15 Å in the center of the pair and decreases by the same amount at the edges of the pair, indicating then that the two molecules are tilted with opposite angles. As the two types of pairs are arranged in alternating rows, the unit cell is a parallelogram with lattice parameters $a_1 = 12.6 \pm 0.3$ Å, $a_2 = 32.3 \pm 0.8$ Å and an angle $\theta = 41 \pm 3$ degrees (solid white line in Fig. 5.5a).

The dimer-like pairing of nickelocene recalls that of ferrocene, and ferrocene-derived molecules on copper surfaces. The intermolecular arrangement is also similar to that encountered for ferrocene, where horizontal and vertical molecules are present in the layer. To visualize the horizontal $NiCp_2$ molecules we acquired low-bias (2mV) images (Fig. 5.5b). The horizontal molecules are then imaged as elongated rod-like protrusions flanking $NiCp_2$ molecules and aligned in the same direction. There are a total of 8 molecules, horizontal and vertical, per unit cell and the packing density is 0.030 molecules/Å^2, which is the same density that the one of the compact network.

The DFT computations performed for such a layer confirm the higher stability of the network including horizontal molecules, as it can be seen in the optimized structure found by the calculations (Fig. 5.5d). The adsorption energy for this layer, 1.52 eV, is close to the one found for the compact network, supporting the fact that we can find both configurations on the surface with the same probability. The tilt of vertical molecules that we observed in STM images (Fig. 5.5a) were reproduced by simulated pictures (Fig. 5.5e-f) thanks to the horizontal molecules which are inducing a geometrical constraint on the vertical ones. This results in a 3° vertical tilt for the lower pairs (blue circled pair) and a 8 ° tilt in the others (red circled pair).

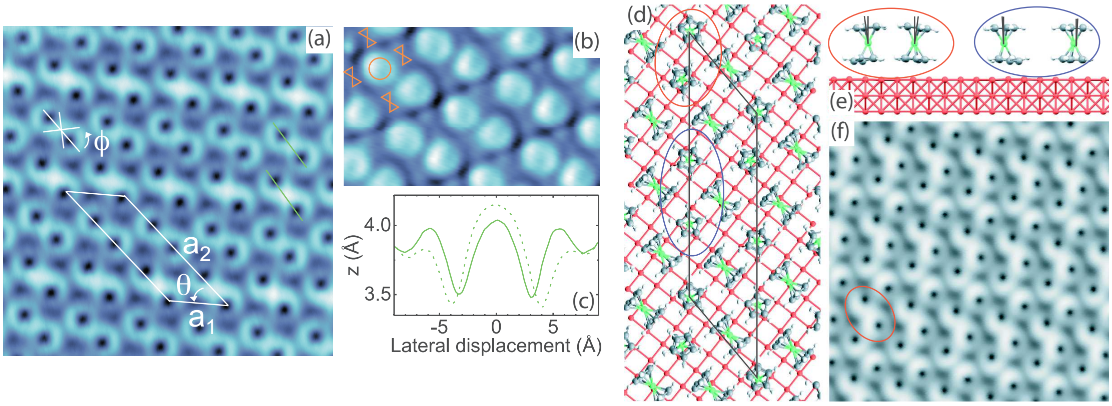

Figure 5.5: **STM image of the paired layer on Cu(100).** (a) STM image of the paired layer (70 × 70 $Å^2$, 20 mV, 20 pA). The unit cell is shown by solid lines. The layer is tilted by an angle ϕ relative to the crystallographic directions of Cu(100), which is depicted by a cross. The dashed circle highlights a defect in the paired layer. (c) Height profiles acquired in compact network. (b), (f) Image of the paired layer acquired with a low tunneling bias (28 × 46 $Å^2$, 1 mV, 10 pA). The molecular arrangement is sketched in orange (circles standing for vertical NiCp2 and hourglasses for horizontal NiCp2). (d) Top view of the optimized paired layer (only one layer of copper is represented), and (e) side view of the paired structure showing the tilt of the vertical molecules (horizontal molecules are omitted for clarity). The two type of $NiCp_2$ -$NiCp_2$ pairs are highlighted in blue and red, respectively. (f) Simulated STM image of the paired layer.

5.1.2 Deposition on Cu(111)

The structure of $NiCp_2$ molecules and layers on Cu(111) was found to be the same as on Cu(100). Isolated molecules were visible aside both compact and paired networks, and the different kinds of molecular assemblies were found with the same rate of occurence at the sample surface (Fig. 5.6).

The parameters of the units cells of the nickelocene networks are compared in Table 5.3 with respect to the crystal geometry. It appears that, as it is the case for ferrocene, the symmetry of the copper crystal does not have a strong influence on the molecule adsorption. This again suggests a physisorption of the molecule on the sample surface.

5.2 Molecular spin excitations

The following section will be devoted to the study of the spectroscopic signatures observed for $NiCp_2$ molecules for both isolated and self-assembled $NiCp_2$ molecules.

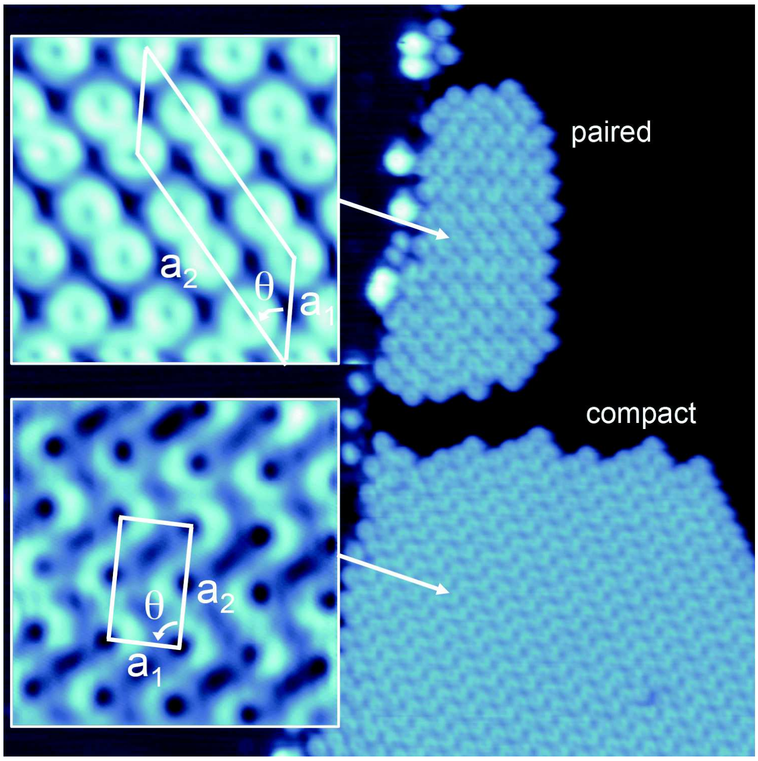

Figure 5.6: **Nickelocene adsorption on Cu(111).** Self-assembled layers (paired and compact configurations) $NiCp_2$ on Cu(111) (image size: 20×20nm^2, sample bias: 20 mV, tunneling current: 50 pA)

compact	a_1 (Å)	a_2 (Å)	θ (deg)
$NiCp_2$/Cu(100)	8.8 ± 0.4	15.1 ± 0.5	90 ± 2
$NiCp_2$/Cu(111)	8.5 ± 0.4	15.7 ± 0.4	90 ± 3
$FeCp_2$/Cu(111)	8.9 ± 0.3	15.5 ± 0.3	90 ± 3
Paired	a_1 (Å)	a_2 (Å)	θ (deg)
$NiCp_2$/Cu(100)	12.6 ± 0.3	32.3 ± 0.8	41 ± 3
$NiCp_2$/Cu(111)	12.9 ± 0.4	31.9 ± 0.4	42 ± 3

Table 5.3: **Unit cells parameters for the different networks of $NiCp_2$ and $FeCp_2$.**

5.2.1 Isolated molecules

Fig. 5.7a presents the differential conductance dI/dV versus bias V spectrum of an isolated $NiCp_2$ molecule. This spectrum was obtained by positioning the tip above the Cp ring of the molecules to ensure a maximum signal to noise ratio. The differential conductance dI/dV exhibits a gap around zero bias with symmetric steps up to 600% times higher in conductance at an energy of $|3.2 \pm 0.1|$ meV (the uncertainty reflects the tip-dependency observed). Such

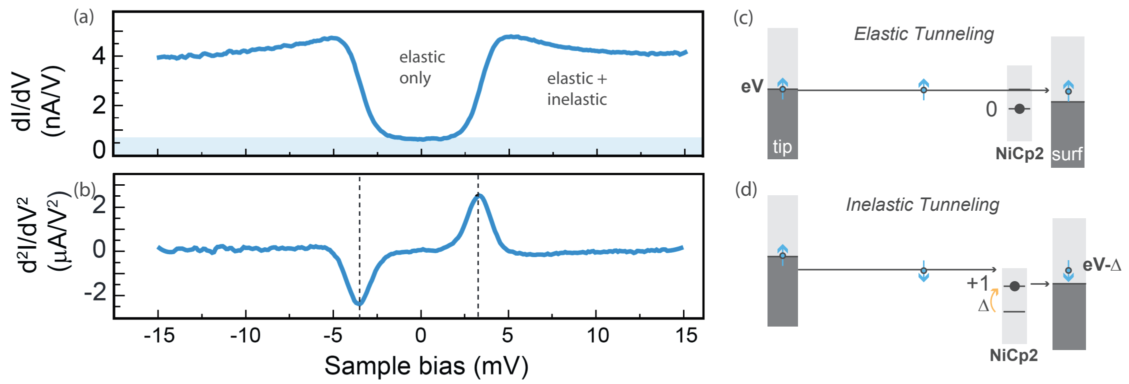

Figure 5.7: **STS of NiCp$_2$.** STS spectrum obtained at low bias above isolated nickelocene. (a) dI/dV spectrum with inelastic signal. (b) Corresponding d^2I/dV^2. (c) Sketch illustrating the elastic tunneling process and inelastic excitation of the single molecule (d). Spectra were acquiered with a lock-in amplifier (150 μV modulation) by opening feedback loop at 50 pA and -15 mV at 2.4 K.

an increase in conductance has to be compared to the weaker rises measured on Fe/Cu$_2$N or Co/Cu$_2$N (see chapter 2 and 3) which is about 30% and Mn/Cu$_2$N with a rise about 100% [176] (with magnetic field). The second derivative of the spectrum (Fig. 5.7b) is also used in order to make easier the threshold values extraction. With such a low excitation energy, vibrational excitations of nickelocene adsorbed on the surface can be *a priori* discarded in this energy range [186].

Former experimental studies on nickelocene powder and gas phase molecules showed that it exhibits a magnetic anisotropy, leading to a zero-field splitting of the ground state [187, 6]. As shown on the energy diagram of NiCp$_2$ (Fig. 5.8), the 4 degenerated states describing the filling possibilities of the antibonding states are first split by the crystal field what discriminates spin $S = 0$ and spin $S = 1$ states. Then, among the triplet $S = 1$, the magnetic anisotropy separates different spin orientations. Here, we only took into account the vertical anisotropy parameter D (the in-plane anisotropy E is assumed to be negligible compared to D for symmetry reasons [5]). We can see from the diagram that the anistropy D corresponds to the energy difference between the spin moment orientation in-plane $|S = 1, M_S = 0\rangle$ and out-of-plane $|S = 1, M_S = \pm 1\rangle$. Earlier measurements on NiCp$_2$ powder gave a value of $D = 4.2$ meV [187] and measurements on crystallites yielded $D = 3.2$ meV [6]. This energy range matches with the excitation energy observed in IETS. The excitation here is attributed to a spin-flip process between the ground state $|S = 1, M = 0\rangle$ and the doubly-degenerated $|S = 1, M = \pm 1\rangle$ state of the molecule.

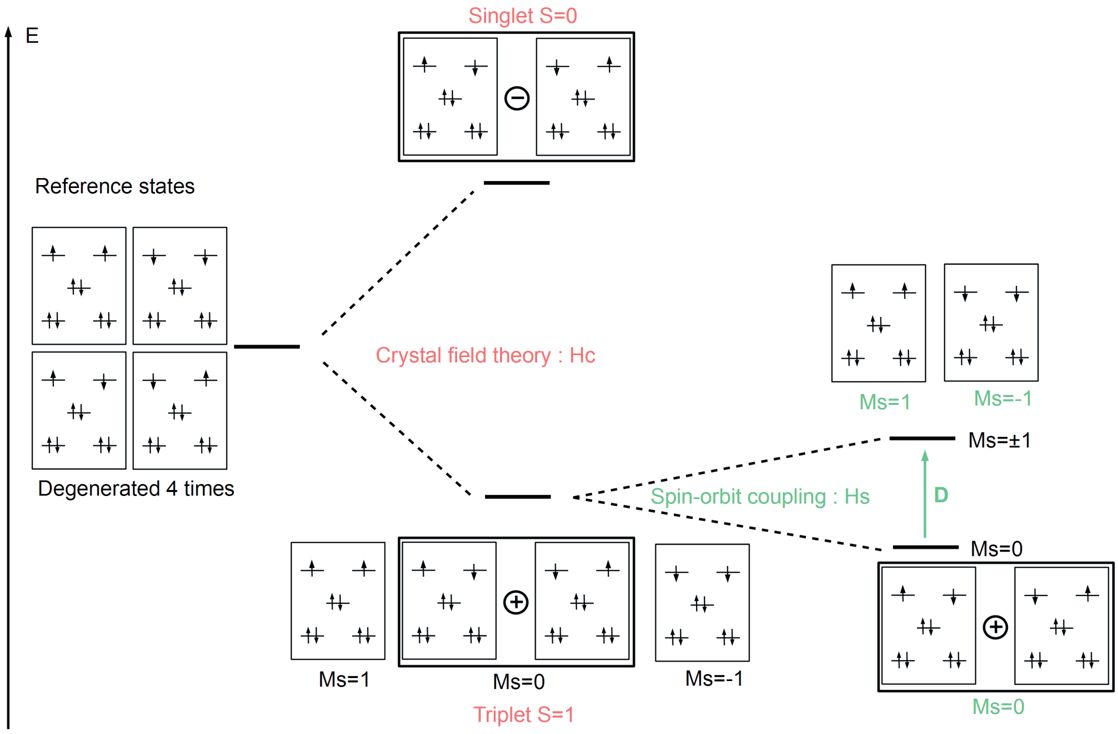

Figure 5.8: **Energy diagram of NiCp$_2$ molecules** including spin-orbirt coupling. The z direction is taken along the molecular axis. First, the crystal field induces a splitting between the singlet state $S = 0$ and the triplet $S = 1$. Then, among the triplet state, the spin-orbit coupling lifts the degeneracy between the states $|S = 1, M_S = 0\rangle$ and $|S = 1, M_S = \pm 1\rangle$, leading to a Zero Field Splitting (ZFS) of energy levels.

Figure. 5.7c-d describes the inelastic tunneling process when an electron flows from the tip to the sample. In the elastic regime, the energy of tunneling electrons is not sufficient to activate the spin-flip process and thus no event occurs during the tunneling. However, when the bias applied to the junction becomes higher than the threshold energy, it becomes possible for the electron to excite the molecule. The tunneling electron loses an amount of energy Δ to populate the $S = \pm 1$ state of the nickelocene. This phenomenon can be described with the following hamiltonian :

$$\hat{H} = D\hat{S}_z^2 - g\mu_B \mathbf{B} \cdot \hat{\mathbf{S}}. \tag{5.2}$$

This hamiltonian describes the single-particle spin behavior [5, 167] considering the axial symmetry of the molecule. The first term accounts for to the magnetic anisotropy, where D is the so-called zero-field splitting. The second term corresponds to the Zeeman energy, where $\mathbf{B}$ is the applied external magnetic field, $g = 2$ the gyromagnetic factor, μ_B the Bohr

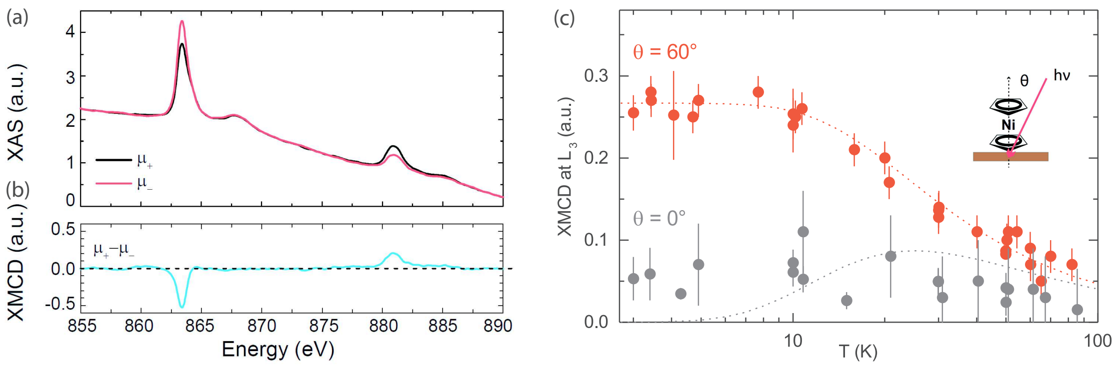

Figure 5.9: **XAS and XMCD obtainded on isolated nickelocenes deposited on Cu(100).** (a) XAS obtainded at 4.7 K under a magnetic field of 6.5 T (incidence angle $\theta = 60^\circ$) on isolated nickelocenes deposited on Cu(100). The black and red curves respectively show the right and left polarization of the magnetic field. (b) Normalized XMCD signal obtained by difference between right and left polarization. (c) Spin moments obtained by normalization of XMCD data on isolated nickelocene. The black and red dots represents the the measurement for a 0° incidence angle (normal) and a 60° incidence angle (grazing) respectively. The continuous line represents the modelled signals (see Appendix B) for a spin $S = 1$.

magneton, $\hat{\mathbf{S}}$ the spin operator vector and $\hat{S}_z$ its projection along the molecular z-axis. In a zero-field situation ($\mathbf{B} = \mathbf{0}$), such as the one we have in the STM measurements, the excitation threshold evidenced in the IETS spectra corresponds to the energy transition between the ground state $|S = 1, M = 0\rangle$ and the first excited state $|S = 1, M = \pm 1\rangle$ and hence yields directly D.

To further characterize the magnetic origin of the excitation, we performed X-ray magnetic circular dichroism (XMCD) measurements in a magnetic field of 6.5 T on a collection of individual $NiCp_2$ molecules on Cu(100). The measurements were carried out at the DEIMOS beamline, at synchrotron Soleil. The XMCD principle is briefly described in appendix A. The deposition of nickelocene molecules was performed using the same geometry (distance between evaporator and substrate, same incident angle of molecular flow) as for STM measurements.

Figure 5.9a shows X-ray adsorption spectra (XAS) recorded at the $L_{2,3}$ edges of Ni for left and right circularly polarized light. The panel below (Fig. 5.9b)presents the difference between them, the so-called XMCD spectrum. Having a clear dichroic signal is already an indication of the magnetic character of nickelocene on Cu(100). Figure 5.9c shows the evolution of the maximum signal at the Ni L_3 edge as a function of the temperature for grazing (red dots, $\theta = 60^\circ$) and normal (black dots, $\theta = 0^\circ$) incidence of the X-ray beam. At low temperature, the signal shows a clear angular dependence revealing the existence

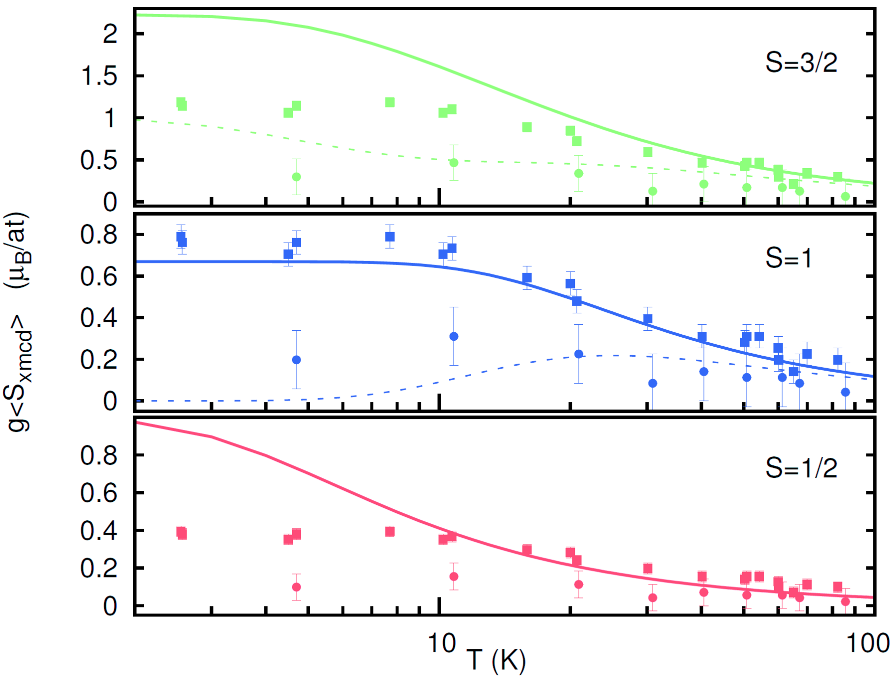

Figure 5.10: **Data points and models of XMCD measurements on Isolated nickelocene.**The sphere dots represents the measurement for a 0° incidence angle and the square dots a 60° incidence angle. The continuous line represent the modelled signals (see appendix B) with respect to the hypothetic spin values of the molecule.

of an easy magnetization direction, more specifically of an easy plane perpendicular to the molecular axis. We have included in the graph the simulated magnetization of a $S = 1$ system under an external field of 6.5 T and possessing a magnetic anisotropy of $D = 3.2$ meV. This thermodynamical model, is described in appendix B. The simulations show a very good agreement between the experimental data and the simulated behaviour for the grazing incidence. The signal is weaker for a normal incidence, as expected, but the signal to noise ration is quite high. The behavior is nevertheless compatible with the calculations for normal incidence.

For the sake of comparison, we have simulated the magnetization behavior of systems with spin $S = 1/2$, $S = 1$ and $S = 3/2$ under an external field of 6.5 T and possessing a magnetic anisotropy of $D = 3.2$ meV (Fig. 5.10). The modelled spectrum based on a spin $S = 1/2$ does not match the experiemental points, because such a model is insensitive to the orientation of the magnetic field. Then, the spin $S = 3/2$ model follows the angle dependency of the data but exhibits a non zero value at 0 K which is uncompatible with our measurements. This comparison shows that the spin $S = 1$ is the best model we can use here to fit our data.

Additionally, the XMCD measurement gave us an information about the easy orientation for the spin of nickelocene. As explained in Appendix A, the XMCD signal corresponds to a measurement of the magnetic moment of the sample projected along the beam axis. In the case of an incident angle of 60°, the XMCD signal is more intense than for a normal incindence. This means the spins of nickelocene molecules are oriented in majority perpendiculary to the normal incident beam axis, that is to say perpendicularly to the molecule axis. Thus, we can say the magnetic anisotropy leads to an easy plane (*xy* plane here) configuration, corresponding to a positive value of D according to Eq. 5.2. This positive value of D was confirmed by our model (see Appendix B) and $M = 0$ corresponds to the ground state of nickelocene, whereas $M = \pm 1$ is the excited state. This means it is possible to switch the spin in-plane orientation of molecule ground state to an out-of-plane state by applying a bias of 3.2 meV.

5.2.2 Self-assembled $NiCp_2$ molecules

We analyse the influence of the network on the magnetic inelastic signal by performing STS spectra above the $NiCp_2$ islands adsorbed on Cu(100). On both compact and paired networks, the dI/dV spectra exhibit an inelastic excitation signal located at 3.2 meV (Fig. 5.11), identical to what was observed above isolated molecules. This indicates a negligible influence of neighbour molecules on the magnetic state of the $NiCp_2$. The absence of influence of the molecular network on the magnetic properties of the molecule is consitent with measurements carried out on $NiCp_2$ powder and crystallites [187, 6] or matrix embedded samples [188].

The STS on networks adsorbed on Cu(111) also presents a spectrum with an inelastic excitation located at 3.2 meV, indicating that the crystal orientation of the substrate does not influence the magnetic anisotropy of the molecule.

5.3 Conductance

Let us now compare STM images with two different biases. In the first case, we use a bias of 20 mV (higher than the energy threshold) and we then lower it to 2 mV (below the energy threshold). The results obtained above an isolated molecule are shown in Fig. 5.12a-c. With the only contribution of the elastic current, the apparent size of $NiCp_2$ is 3.1 Å, identical to the height of $FeCp_2$ (see chap. 4). The contribution of the inelastic current changes this height to 3.7 Å. Furthermore, the inelastic contribution of the current causes the appearence of a ring shape which was barely visible on ferrocene. The STM images of compact network taken at bias below and above the excitation energy (Fig. 5.12d-f) show that, as for the

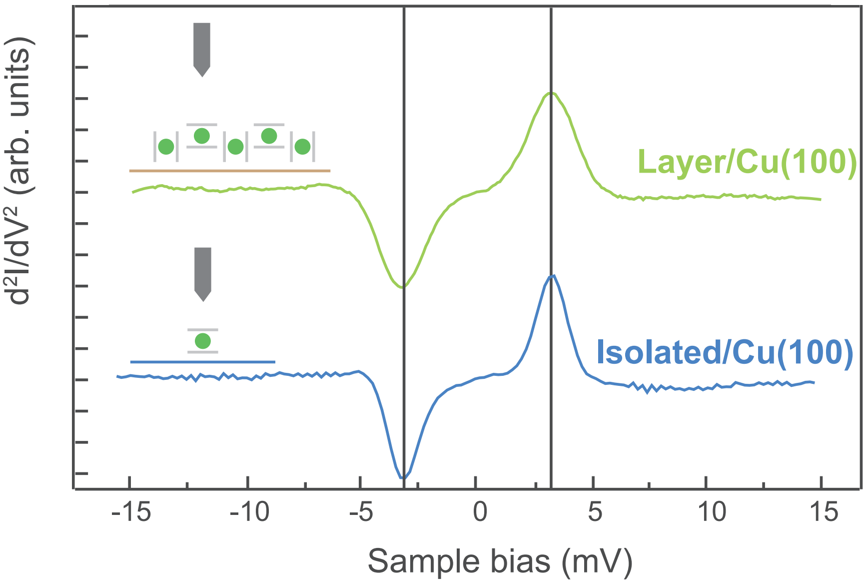

Figure 5.11: **Comparison of inelastic spectra obtained above isolated and networked NiCp$_2$**. We compare here d^2I/dV^2 spectra to obtain a more accurate position of inelastic transition. The blue curve represents the spectrum obtained above an isolated molecule and the green one represents the signal measured above the molecular network. In both cases, the energy threshold is located at 3.2 meV. Spectra acquiered with a lock-in amplifier (150 μV modulation) by opening feedback loop at 50 pA and -15 mV at 2.4 K.

isolated molecule, the inelastic tunnel current contribution also rises the apparent height by 0.7 Å. The rise in conductance is here also in the order of 600%, with small variations of this value depending on the specific STM tip employed in the measurements.

We tried to model the behaviour of the NiCp$_2$ conductance using the same method as in Chapter 3. In the case of isolated atoms deposited on Cu$_2$N [5], the amplitude of conductance increase was modelled using Eq. 5.3 :

$$\begin{aligned} I_{i\to f} &= |\langle\psi_f|\hat{S}_x|\psi_i\rangle|^2 + |\langle\psi_f|\hat{S}_y|\psi_i\rangle|^2 + |\langle\psi_f|\hat{S}_z|\psi_i\rangle|^2 \\ &= \frac{1}{2}|\langle\psi_f|\hat{S}_+|\psi_i\rangle|^2 + \frac{1}{2}|\langle\psi_f|\hat{S}_-|\psi_i\rangle|^2 + |\langle\psi_f|\hat{S}_z|\psi_i\rangle|^2 \end{aligned} \tag{5.3}$$

This model gives results in agreement with Fe and Co adatoms deposited on a Cu$_2$N surface, thus we applied it to the NiCp$_2$ molecule. Considering the spin $S = 1$ of nickelocene, we defined the initial state as $|\phi_i\rangle = |S = 1, M = 0\rangle$ and the final states are the degenerate manyfold $|\phi_f\rangle = |S = 1, M = \pm 1\rangle$. The calculation yields a ratio between elastic and inelatic

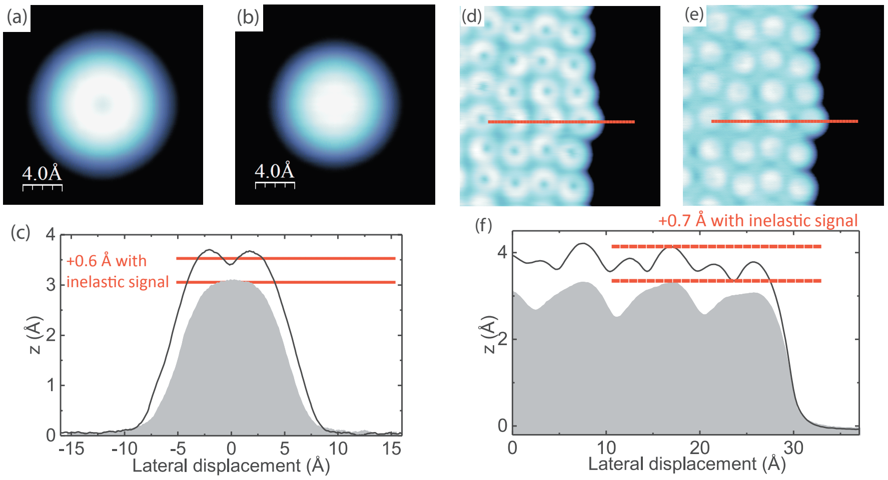

Figure 5.12: **Effect of inelastic conductance in STM pictures.** Difference between STM images taken below and above the excitation threshold. (a) Isolated nickelocene STM image taken at 20 mV. (b) Same molecule imaged at 2 mV. The current was adapted to keep the same tip/sample distance (conductance). (c) Comparison of the two line profile without and with the inelastic contribution in the tunneling current. The grey volume shows the profile obtained only with the elastic tunneling current and the dark line shows the profile with the inelastic current contribution. (d) STM image of a compact network edge taken at 20 mV. (e) Same area imaged at 2 mV. The current was adapted to keep the same tip/sample distance (conductance). (f) Comparison of the two line profile without and with the inelastic contribution in the tunneling current.

conductance $I_{i \to f} = 1$, far from the experimental ratio of 6. This illustrates the necessity of using a more sophisticated model to describe the conductance through inelastic channels.

To rationalize our experimental results, we need a quantitative estimate of the ratio between the inelastic and elastic conductances, which is not straightforward to do with common theoretical approaches [94, 130]. We therefore use here a strong coupling theory developed by Lorente and Gauyacq [91, 131] to explicitly introduce spin symmetries which lead to a simple formulation of the problem. As we show hereafter, by exploiting the multichannel T-matrix approach, we can express this ratio in terms of contributions to the square modulus of the T-matrix elements.

We start by remarking that the tunneling of an electron from the STM tip into the nickelocene molecule is equivalent to a three-step collision. First, a single electron is injected into the empty state of the molecule. Then, a transient negatively charged molecular ion is created and finally the negative ion decays by ejecting one electron into the substrate. We may assume that the magnetic anisotropy (see Eq. 5.2) is nonactive during the collision as the rotation of the adsorbate spin due to the magnetic anisotropy is slow compared to the time

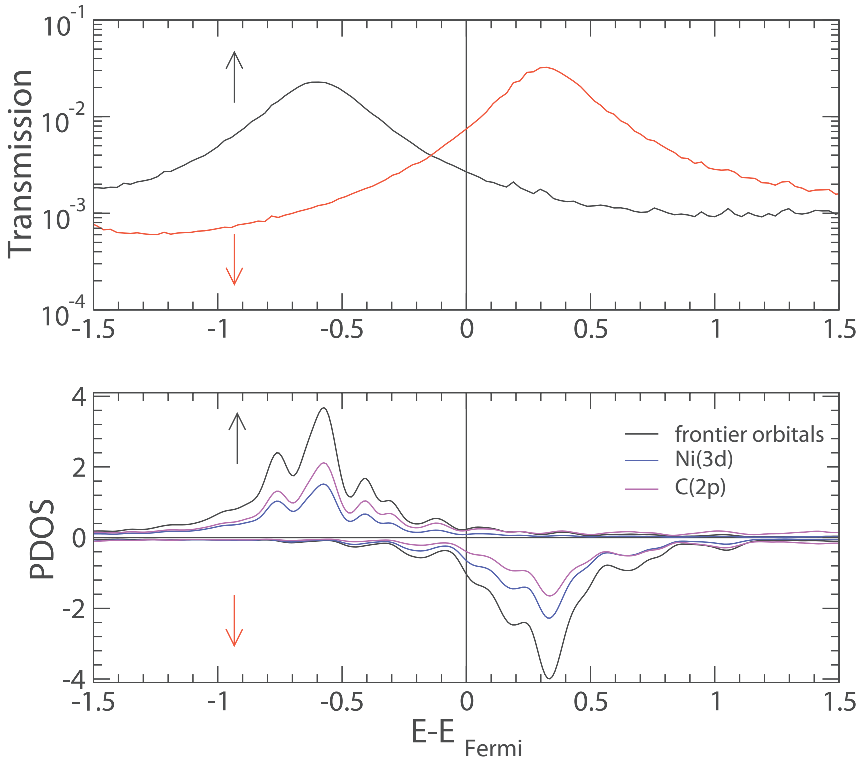

Figure 5.13: **NEGF-DFT calculation.** Upper panel: Spin-resolved electron transmission as a function of electron energy with respect to the Fermi energy, in a tunneling junction described by two semi-infinite Cu(100) surfaces, and a nickelocene molecule adsorbed on one of the surfaces. The transmission shows two clear peaks corresponding to both spins. Each of the peak corresponds to the peak in the projected density of states (PDOS) depicted in the lower panel. There, the peaks are traced back to the molecular orbitals of the nickelocene molecule originating from the d_{xz} and d_{yz} nickel orbitals.

scale of electron tunneling. Despite this so-called sudden approximation, we stress that the magnetic anisotropy is “active” at the beginning and at the end of tunneling process. Under these assumptions, the electronic current takes the form [131]:

$$I = C \sum_{m_i, m_f, i, f} |\langle \phi_i, m_i | T | \phi_f, m_f \rangle|^2 \delta(E_i - E_f), \tag{5.4}$$

where T is the scattering matrix, $|\phi_i\rangle$ and $|\phi_f\rangle$ are, respectively, the initial and final states of the electron and of the molecule, E_i and E_f the total energy of these states. For nickelocene, we have a spin $S = 1$ and an easy-plane anisotropy, hence, the initial state is $|\phi_i\rangle = |s = 1/2, \pm m = 1/2; S = 1, M = 0\rangle$, where s is the electron spin and m its projection on the quantization axis. The final states are instead degenerate $|\phi_f\rangle = |s = 1/2, \mp m = 1/2; S = 1, M = \pm 1\rangle$.

Using the sudden approximation, we split the contribution to the T-matrix in collision channels of total spin S_T where the spin of the tunneling electron couples to the spin of the molecule. There are only two possible channels, one corresponding to $S_T = 1 - 1/2 = 1/2$ and the other to $S_T = 1 + 1/2 = 3/2$, resulting in two matrix elements $T^{S_T} = T^{1/2}$ and $T^{3/2}$.

Using Eq. (5.4) and following the procedure described in [91, 131], we find that the elastic contribution to the conductance is proportional to:

$$G_e \propto \frac{2}{9}|2T^{3/2} + T^{1/2}|^2, \tag{5.5}$$

while the inelastic conductance is proportional to:

$$G_i \propto \frac{4}{9}|T^{3/2} - T^{1/2}|^2. \tag{5.6}$$

The relative change in conductance at the inelastic threshold is:

$$\frac{G_i + G_e}{G_e} = \frac{2\,|T^{3/2} - T^{1/2}|^2}{|2\,T^{3/2} + T^{1/2}|^2} + 1. \tag{5.7}$$

To evaluate the ratio of Eq. (5.7), we need to put numbers into $T^{1/2}$ and $T^{3/2}$. To do so, we recall that in the spherical approximation underlying the sudden approximation, the T-matrix can be expressed as [94, 100]:

$$T = T_0 - T_1 \vec{S} \cdot \vec{s} \tag{5.8}$$

where T_0 and T_1 can be easily written in terms of $T^{1/2}$ and $T^{3/2}$. Following [131], we have

$$\begin{aligned} T^{3/2} &= T_0 + 0.5T_1, \\ T^{1/2} &= T_0 - T_1. \end{aligned} \tag{5.9}$$

The advantage of this expression is that by using the Schrieffer-Wolf transformation [100] we can estimate $T^{1/2}$ and $T^{3/2}$ from the elastic transmission. Indeed, from the Schrieffer-Wolf transformation we have that

$$T_1 \approx -2T_0 \frac{U}{U + 2\varepsilon_d}, \tag{5.10}$$

where U is the Hubbard term entering the Anderson Hamiltonian and ε_d is the energy of the occupied impurity level (here the occupied molecular level). This result is readily obtained by assuming the Born approximation for the T-matrix and using the Schrieffer-Wolf transformation for the potential and the spin-flip terms. To evaluate the elastic transmission, we perform a non-equilibrium Green function calculation based on density functional theory (NEGF-DFT). Figure 5.13 shows the results of this calculation for a nickelocene molecule between two Cu(100) electrodes. A double-zeta basis set is used together with PBE version of the generalized gradient approximation to DFT. The TRANSIESTA code [189] is used to perform the calculation. We find that all the conductance takes place through the d_{xz}- and d_{yz}-based molecular orbitals. Due to the $S = 1$ state of the molecule, there is an electron in each of these two molecular orbitals leading to an exchange splitting U of the two resonances(Fig. 5.13), hence to a transmission at the Fermi energy that is dominated by the contribution of the minority states. We see from Fig. 5.13 that $U = 0.9$ eV and $\varepsilon_d = -0.6$ eV. Turning now back to Schrieffer-Wolf transformation, the relative change in conductance at the inelastic threshold after the Schrieffer-Wolf transformation becomes

$$\frac{G_i + G_e}{G_e} \approx \frac{2U^2}{(U + 2\varepsilon_d)^2} + 1, \tag{5.11}$$

which yields 1900%, roughly 3 times larger than the experimental value. However, it is well known that DFT grossly underestimates the energy position of the molecular orbitals. Indeed, excellent agreement with the experiment is obtained if the empty molecular orbital were placed at $U + \varepsilon_d = 0.5$ eV instead of 0.3 eV with $U = 0.8$ eV instead of 0.9 eV for the present DFT calculation.

This calculation shows that the spin inelastic effect in nickelocene is utterly efficient due to the interference effect of the two spin-channel symmetries, $S_T = 3/2$ and $S_T = 1/2$, an effect that has not been seen in previous experiments that were understood by the prevalence of one of the collisional symmetries [131].

5.4 NiCp$_2$ functionalized tip

5.4.1 Molecular tip characterization

The high robustness of metallocenes enables us to transfer them from the surface to the tip by contacting them while performing an $I(z)$ spectrum at low bias. With nickelocene, another method is possible. We obtain an easy and reproducible molecular tip by scanning a target molecule at very low negative bias (-1mV) on the tip and few tenth of pA (20 pA usually). A way to re-deposit the molecule on the surface consits in repeating this operation using a positive low bias (+1mV) on the tip. Once a NiCp$_2$ molecule is adsorbed on the tip apex, we can check the presence of the molecule by performing reversed images (Fig. 5.14). On these

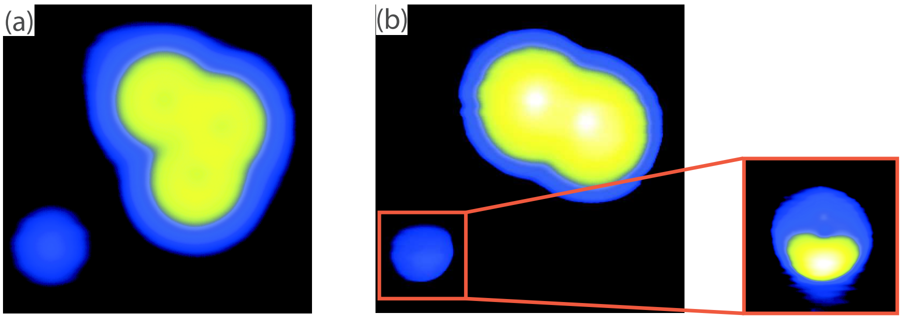

Figure 5.14: **Molecular STM tip creation.** (a) Image (-15 mV, 100 pA) of a nickelocene trimer adsorbed on Cu(100) before catching a NiCp$_2$ on the tip. (b) STM image of the same area after catching a single molecule. The inset expands the counter image of the tip on the copper adatom on the bottom left corner.

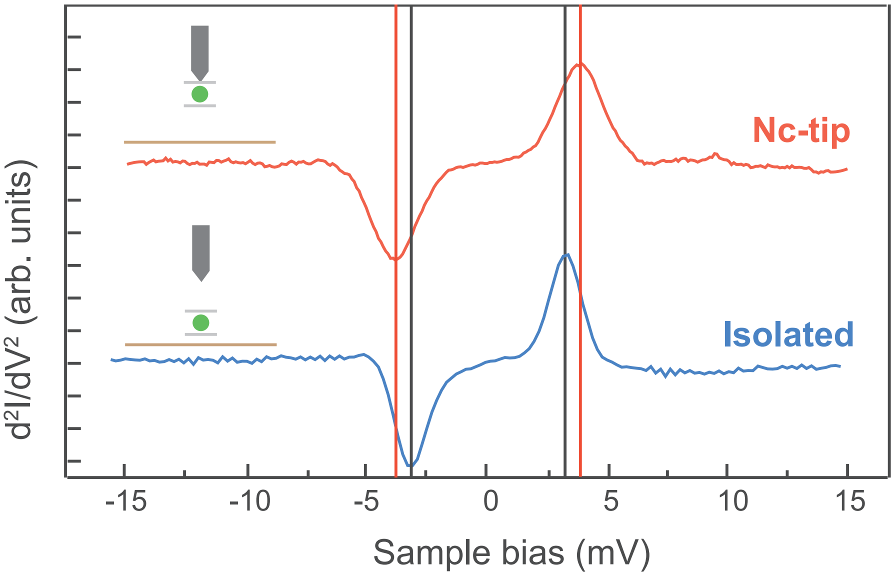

Figure 5.15: **Molecular tip IETS.** Comparison of d^2I/dV^2spectra obtained with respect to the position of the molecule between the tip and surface sample. The red curve shows the case of a nickelocene molecule is adsorbed at the apex of the STM tip and the blue curve represents the spectrum above an isolated nickelocene on copper crystal. Spectra acquiered with a lock-in amplifier (150 μV modulation) by opening feedback loop at 100 pA and -40 mV at 2.4 K.

reversed images, a single adatom on the surface exhibits a partial ring shape, showing the molecule is adsorbed at the apex of the tip and slightly tilted.

The dI/dV spectra (Fig. 5.15) obtained on bare copper with the molecular tip show a single excitation located at 3.7 ± 0.3 meV, slightly different from the 3.2 meV observed for

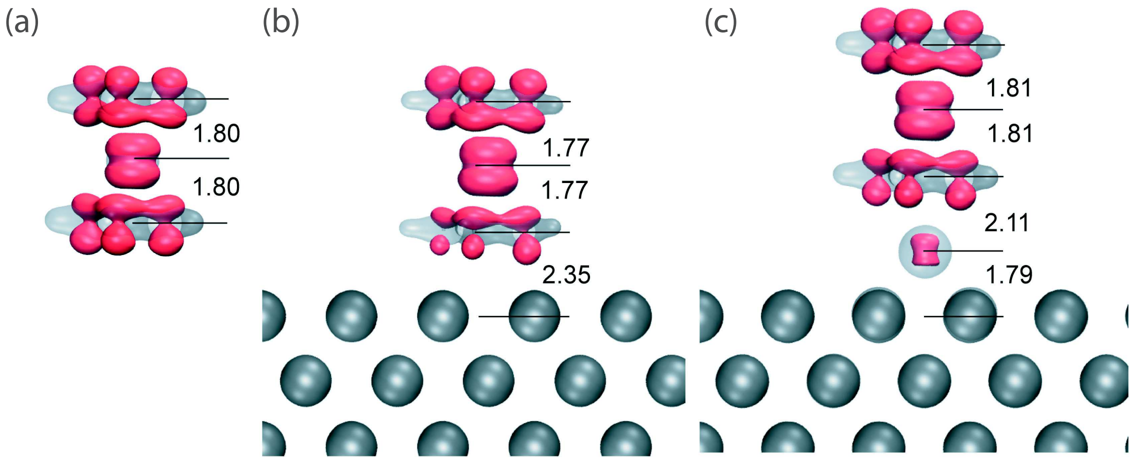

Figure 5.16: **Molecular tip characterization.** (a) Spin density (majority spin in red, negligible minority spin) and total electron density (grey transparent) of gas phase NiCp$_2$ with MAE = -1.54 meV. (b) adsorbed NiCp$_2$ on Cu(100) with MAE = -1.27 meV and (c) adsorbed Cu-NiCp$_2$ on Cu(100) with MAE = -1.49 meV (c). The isosurface of the spin (total electron) density is 0.02 (1.3) electron per Å^3. Vertical heights are given in Å and the magnetic anisotropy (MAE) resulting from a spin-orbit coupling calculation is also indicated. The numbers give the distances between the centers of the C, Ni an Cu atoms, expliciting the differences in molecule size induced by charge transfer.

a molecule adsorbed on a crystal. Here, the conductance increase can reach 900% when the inelastic tunneling path is opened. The difference in conductance increase between the molecular tip and the isolated molecule adsorbed at the sample surface corresponds to the influence of the adsorption on magnetic anisotropy. We computed the Magnetic Anisotropy Energy (MAE) for different adsorption of the molecule, modelling the tip apex by a single atom located on a hollow position of a Cu(100) surface. Calculations were performed within DFT framework by including the Spin-Orbit Coupling (SOC) in computations with MAE defined as

$$MAE = E_{\parallel}^{SOC} - E_{\perp}^{SOC} \tag{5.12}$$

where $E_{\parallel}^{SOC}$ correponds to the energy obtained including the spin-orbit interaction for a spin parallel to the metallic surface and $E_{\perp}^{SOC}$ to the case of a spin perpendicular to the sample surface. A non zero value of the MAE expresses the presence of an easy axis. Here, a positive value (*i.e.* $E_{\perp}^{SOC} < E_{\parallel}^{SOC}$) of MAE will indicate an easy axis out of plane (perpendicular to the surface) whereas a negative value reveals an easy axis parallel to the metal surface.

Figure 5.16 shows the results of the computation for spin densities and magnetic anisotropy energy with respect to adsorption possibilities. The computed MAE corresponding to the case of nickelocene in gas phase is -1.54 meV. When the molecule is adsorbed on a metal surface, the MAE is lowered to -1.27 meV. In this case, the molecule size decreases to 3.54 Å due to the depopulation of the antibonding states. The associated charge transfer is estimated to 0.1 electron from the molecule to the substrate. If we now focus on the model of the molecule adsorbed on a Cu atom of the tip, we obtain different charge transfer and MAE. The charge transfer due to the adsorption is estimated to 0.14 electron from the Cu atom to the molecule, leading to a small size increase from 3.60 Å to 3.62 Å. This reversed charge transfer compared to the molecule adsorbed on the crystal leads to the more intense MAE, opening a slightly wider gap in STS spectra (Fig. 5.15).

5.4.2 Double transition

Finally, we use the molecular tip to probe the magnetic effects at work when two different molecules are present in the STM junction. The main aspect of the STS spectrum acquiered with a molecular tip above a second $NiCp_2$ molecule (Fig. 5.17a-c) is the double inelastic signal when two molecules are facing each other in the junction. The two excitations energies are here 3.4 ± 0.2 meV and 6.9 ± 0.4 meV. The spectra can be divided into 3 different regions: the region labelled 1 below the lower excitation energy, the region labelled 2 between the two inelastic steps and the region labelled 3 above the higher excitation energy. Those three regions correspond to different excitation processes (Fig. 5.17e-g). The sketch labelled (e) corresponds to the region 1 of the spectra, when the tunneling electron do not have enough energy to excite any nickelocene in the junction. The sketch (f) presents the phenomenon occuring in region 2. Here, the electron can give up energy while tunneling to excite one of the molecules only. Now, we have no clue to identify if the excited molecule is the nickelocene adsorbed on the tip or on the sample. Finally, the last sketch corresponds to region 3, when the tunneling electron excite both molecules of the junction.

The most prominent effect associated to the double spin excitation is the drastic enhancement of the conduction step height observed at the second excitation (a factor 60 with respect the elastic signal in the spectrum of Fig. 5.17b) that we explain as follows. Considering that the excitations of the molecule on the tip and on the sample are independent processes, we can assume that the conductance measured in each region is the product of two probabilities. In particular, let us suppose that the conductance is proportional to the probability of taking one electron from one electrode (tip) into the other electrode (surface), in other words that the conductance is proportional to the T-matrix modulus squared [131].

Since the T-matrix has now spin degrees of freedom in the tip and on the sample, we denote the new matrix elements as $T_{n,m}$ where n is the number of excitations of the tip and m the number of excitations of the sample. Then, the conductance will be proportional to

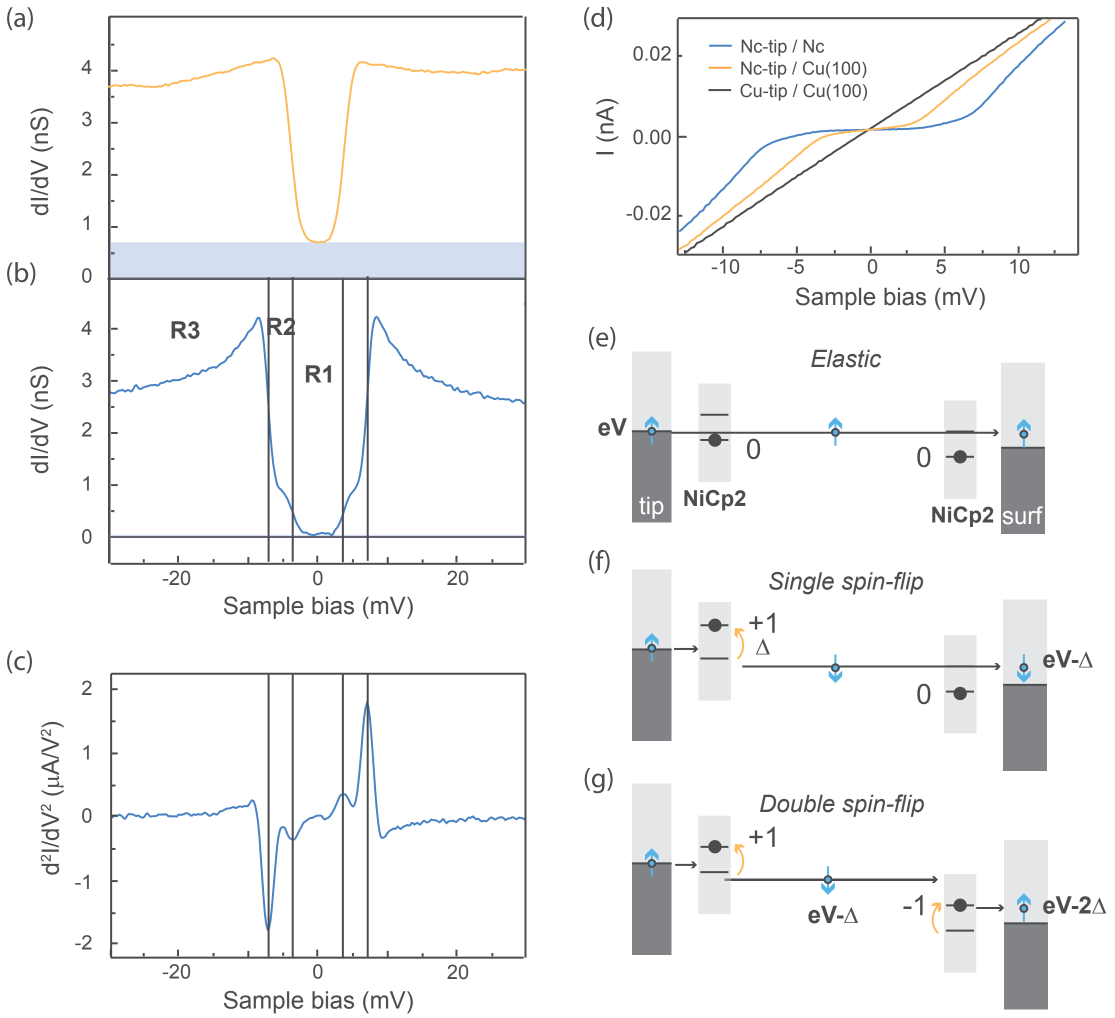

Figure 5.17: **Double spin excitation in IETS.** Double spin-flip excitation (a) dI/dV spectrum of a NiCp$_2$-terminated tip above Cu(100). Panel (b) shows the dI/dV spectrum of a NiCp$_2$ molecule measured with a NiCp$_2$-terminated tip. Three tunneling regimes are highlighted (see text) indicated by R1, R2 and R3. The feedback loop was opened at 100 pA and -40 mV. (c) d^2I/dV^2 versus V in a smaller bias range than panels (a) and (b). Panel (d) presents the $I(V)$ curve showing the opening of the inelastic channels. Panels (e) to (g) present a sketch of the different tunneling mechanisms: (e) there is only elastic tunneling of electrons; (f) the spin of only one of the molecules is excited. In this case the excitation of the molecule on the tip from $M = 0$ to $M = +1$ is shown, (g) both molecules undergo spin-flip excitations.

$\sum_{n,m} |T_{n,m}|^2$, with a sum on the excitations since the channels are supposed independent. In this case, $T_{0,0}$ corresponds to the elastic transmission of an electron from the tip to the surface or *vice versa* (region 1). $T_{1,0}$ and $T_{0,1}$ correspond to the case in which there is one inelastic event during the process, *i.e.* in the molecule on the tip, or on the surface. Finally, $T_{1,1}$ is related to the probability of an electron being transmitted inelastically between the electrodes exciting both molecules.

Hence, if the applied bias is high enough to open the first excitation channel for the molecules on the tip and on the sample (region 3), we obtain that the conductance is proportional to

$$|T_{0,0}|^2 + |T_{1,0}|^2 + |T_{0,1}|^2 + |T_{1,1}|^2. \tag{5.13}$$

The observed inelastic *versus* elastic ratios show tip dependency. Considering the maximum step height values we observed, we have for the NiCp$_2$ on the tip that

$$(|T_{1,0}|^2 + |T_{0,0}|^2)/|T_{0,0}|^2 \approx 9 \tag{5.14}$$

and for the NiCp$_2$ on the surface

$$(|T_{0,1}|^2 + |T_{0,0}|^2)/|T_{0,0}|^2 \approx 6. \tag{5.15}$$

Since the excitations of the molecule on the tip and on the sample are independent, the transmission probability of a double spin-flip excitation to occur is approximately

$$|T_{1,0}|^2 |T_{0,1}|^2/|T_{0,0}|^4 = |T_{1,1}|^2/|T_{0,0}|^2 \approx 8 \cdot 5 = 40. \tag{5.16}$$

The conductance is then in region 3,

$$(|T_{0,0}|^2 + |T_{1,0}|^2 + |T_{0,1}|^2 + |T_{1,1}|^2)/|T_{0,0}|^2 = 1 + 5 + 8 + 40, \tag{5.17}$$

this is 54 times higher than the elastic conductance alone (region 1).

Along this chapter, we investigated the adsorption of nickelocene deposited on copper. We showed by XMCD that even when adsorbed on sample surface, the NiCp$_2$ maintains its spin $S = 1$ and its magnetic anisotropy. The STS performed above such a molecule showed an inelastic tunneling process caused by the excitation of a new spin orientation in the molecule. Tunneling with a bias $|V|$ superior to the excitation energy (3.2 meV) leads to a change of the spin orientation of the molecule, from an in-plane configuration to an out of plane orientation. Such an excitation opens a new path 5 times more conductive than the elastic channel. We then transferred the molecule to the tip in order to obtain a molecular magnetic tip. The excitation property is transferred to the tip, and the difference in adsorption geometry causes an increase of 15% in MAE, enlarging the excitation energy in IETS.

We finally used the molecular tip to probe a second molecule at sample surface, creating a junction incorporating two metallocenes. We observed in the conductance spectra a double transition corresponding to the excitation of one and two molecules at a time respectively. If the excitation energy thresholds are added, the conductance is dramatically enhanced compared to the elastic tunneling regime. We expect to use such a molecular tip to enhance the detection of inelastic phenomena, such as the detection of the inelastic transitions of isolated Fe atom deposited on Cu_2N.

Chapter 6

Conclusion and Perspectives

Motivated by the theoretical results showing the spin filtering efficiency of devices based on metallocene chains, we started to experimentally study these molecules in contact with metal electrodes. According to theoretical results, the length of the chains and the nature of the metal atoms incorporated into them have a strong effect on the spin filtering effect that we are looking for. However, before engineering spintronic devices at a single molecule level, we needed to understand how metallocenes behave when deposited on (non magnetic) metal electrodes and if a chain can be built using such molecules. The molecules we started to study in particular were $FeCp_2$ (non magnetic) and $NiCp_2$ which has a spin $S = 1$.

We used a Scanning Tunneling Microscope to investigate both the adsorption geometry and the electronic properties of single metallocenes when deposited on metallic surfaces. Then, we compared the experimental results with DFT computations performed by our collaborators. We first focused on the adsorption of $FeCp_2$ and $NiCp_2$ on copper crystals, Cu(100) and Cu(111). Aside isolated molecules, we observed spontaneously formed networks and a careful investigation of STM pictures suggested that metallocenes are networking by alternating vertical and horizontal molecules. No dramatic difference in adsorption or networks configurations were visible when changing the crystal orientation, indicating a physisorption of the molecules. DFT results confirmed that the molecules are physisorbed and that the networks are based on T-shape interaction between molecules. Furthermore, the computations showed that van der Waals forces are the main contribution in molecule-molecule interaction but also in adsorption energy (molecule-surface interation). Considering also preliminary results obtained on cobaltocene molecules ($CoCp_2$, not included in my PhD thesis), we can assume that the tendency to form networks including both vertical and horizontal molecule is a general property of metallocenes. The results we obtained here show that it is possible to build and study a system based on single metallocenes at low temperature, opening the way to device engineering.

To tailor metallocene chains, we explored the spin doping of $FeCp_2$ by a single Co atom. This Co adatom appeared to be more stable when located between a vertical molecule and the sample ($FeCp_2$/Co/Cu(100) configuration) rather than staying on top of a ferrocene (Co/$FeCp_2$/Cu(100) configuration). To experimentally confirm this assumption, we artificially created the $FeCp_2$/Co/Cu(100) system using the STM tip: starting from a single Co atom adsorbed on copper crystal, we picked up a ferrrocene with the STM tip and deposited it on the Co atom. Both topographic and spectroscopic results obtained in this single molecule case were similar to what was observed in the molecular network, showing the Co atom effectively adsorbed below the layer. Computations showed that a part of the Co charge is transferred to the Fe atom of the molecule. The appearance of the Kondo effect shows that the $FeCp_2$/Co system is magnetic, DFT calculations indicating that the system has a spin $S = 1/2$.

The main difference between $FeCp_2$ and $NiCp_2$ is the spin $S = 1$ of nickelocene in the gas phase due to the two supplementary electrons of the Ni atom. Earlier results obtained on nickelocene powders and crystallites also demonstrated that a magnetic anisotropy exists in this molecule. Using XMCD, we first confirmed that the spin $S = 1$ character of the molecule, adsorbed on metallic crystal, is preserved. Then we showed that the magnetic anisotropy favoring an in-plane spin orientation survives the adsorption. The dI/dV spectra acquired above such a molecule revealed an inelastic feature corresponding to the excitation of a zero-field spin-flip process, due to the magnetic anisotropy. This means that we can control the spin orientation of the molecule by applying a low bias. When the inelastic tunneling path is opened, the conductance increases up to 600% compared to the elastic tunneling regime. Such an intense rise in conductance for single molecule was explained using a collision model between a single electron (spin $S = 1/2$) and the nickelocene (spin $S = 1$).

We could then transfer this molecule to the STM tip by low bias contact. The spectra obtained with the molecular tip on bare copper showed the same kind of inelastic excitation as for isolated molecule on crystal. We however observed an increase of the excitation energy from 3.2 meV to 3.7 meV, indicating the adsorption geometry plays a role in magnetic anisotropy. We finally used the molecular tip to probe the magnetism of a second molecule. In such a junction, several paths are possible for electrons: elastic tunneling, inelastic tunneling leading to the excitation of one molecule and inelastic tunneling leading to the excitation of two molecules.These excitations are visible in the dI/dV spectra as double steps. To excite the two molecules in the junction, the threshold energies are adding to each other, while the increase in conductance reaches 6300% of the elastic conductance. Based on this result, we expect to use a molecular tip to boost the detection of spin-flip events.

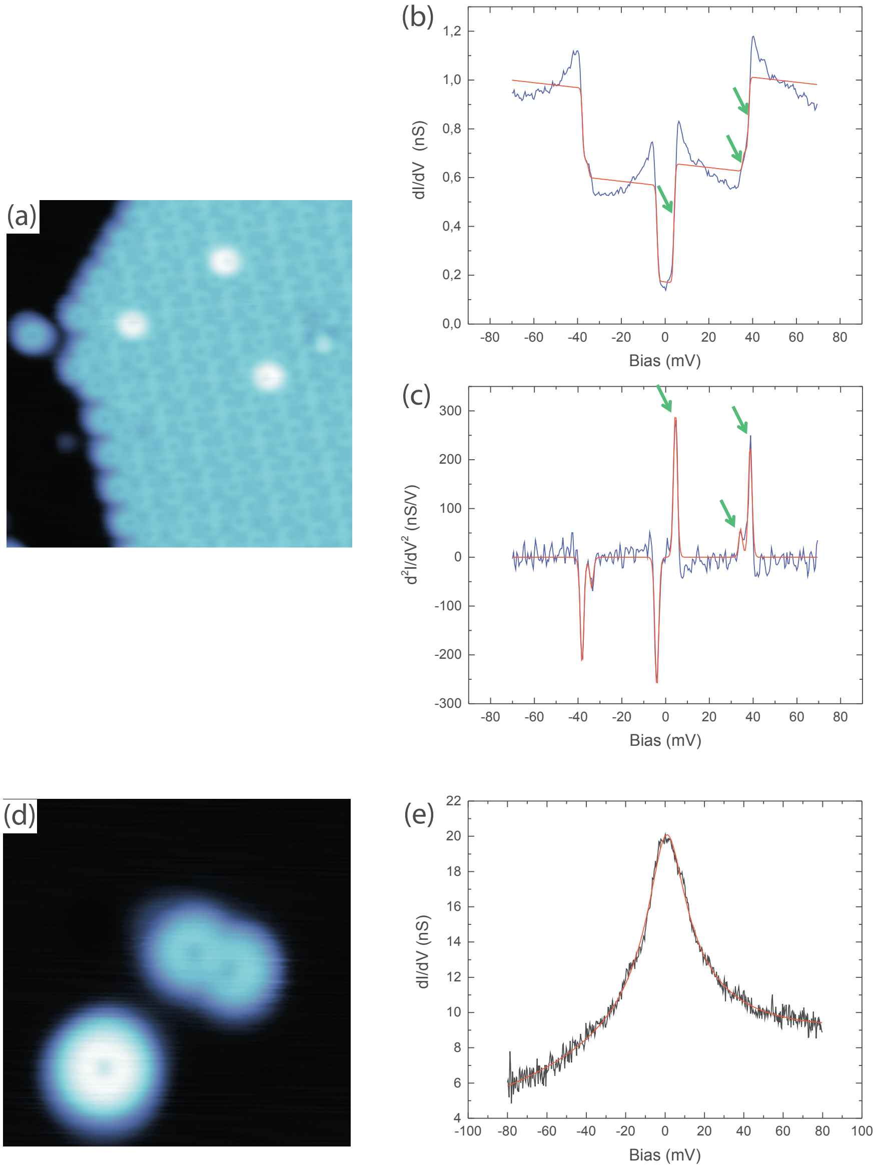

Figure 6.1: **Ni adatoms on NiCp$_2$.** (a) STM image of NiCp$_2$ layer with Ni adatoms (20 mV). The apparent height of this new molecule is 2 Å higher than the surrounding layer and the ring shape is preserved. (b) Measured (blue) dI/dV spectrum of the Ni atom adsorbed on NiCp$_2$ layer and second derivative of the current with respect to bias (c). The 3 inelastic transitions are located at 4.1 meV, 35.5 meV and 38.2 meV. The correponding fitted curves at 2.49 K are given in red. (d) STM image of isolated NiCp$_2$ and manually assembled NiCp$_2$ on Ni atom (20 mV). (e) STS spectrum obtained above NiCp$_2$/Ni system.

Future work will be devoted at doping NiCp$_2$ with magnetic atoms, for example Ni. The results of the evaporation of Ni atoms on cold NiCp$_2$ networks is given in Fig. 6.1(a-c).

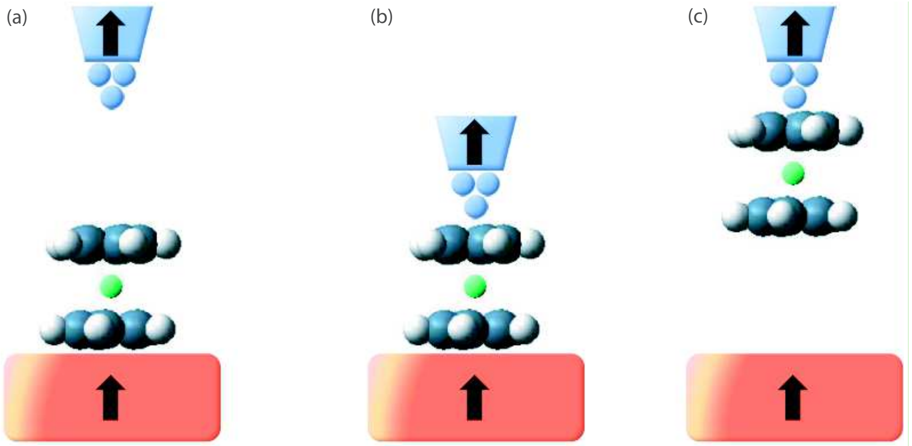

Figure 6.2: **Possible configurations to be used in spin polarized measurements.** (a) Characterization of metallocenes on magnetic substrate. (b) Contact measurements. (c) Tip functionnalisation.

The protusions caused by the adsorption of an extra Ni atoms exhibit here a ring shape, and the spectra acquired above such a new molecule present 3 inelastic features. We compared this system with a manually created $NiCp_2$ molecule adsorbed above a single Ni atom on the crystal surface, see Fig. 6.1(c-d). If the apparent height and shape of this single object are similar to the networked $NiCp_2$ + Ni system, the conductance spectrum here exhibits a Kondo resonance. An early hypothesis concerning the differences in dI/dV spectra is that neighboring $NiCp_2$ molecules in the network tend to pull up the $NiNiCp_2$, thereby reducing its coupling to the metal surface. Complementary analyses are requiered here to understand the different phenomena involved in the spectroscopy results.

Following the idea of creating single-molecule based spintronic devices, the next step will consist in studying the behaviour of metallocenes interacting with magnetic electrodes (Fig.6.2). The next thesis in the group will develop this aspect by depositing molecules on Co surfaces and investigating their properties using a magnetic tip. A detection of spin-polarized current is expected, either through SP-STM(see chapter 3), and/or IETS. In the latter case, a shift of the excitation energy of single molecule is expected because of the magnetic interaction with the Co surface. We then intend to spin dope this system in an attempt to build an ideal single-molecule spin filter.

Appendix A

XMCD principle

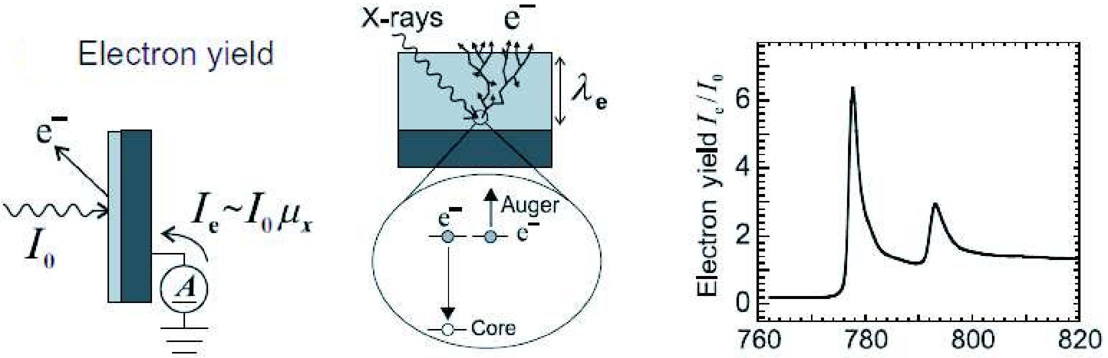

Figure A.1: **Principle of XMCD.** Method and principles of recording absorption spectra by electron yield (or total electron yield) detection. The absorbed photons create core holes that are filled by Auger electron emission. The primary Auger electrons cause a low energy cascade through inelastic scattering processes on the way to the surface. The total number of emitted electrons is directly proportional to the probability of the Auger electron creation, that is the absorption probability. The emitted electron yield is simply measured with a picoammeter that measures the electrons flowing back to the sample from ground. The electron yield spectrum I_e/I_0 shown on the right is that of Co metal. Picture adapted from [190].

To experimentally confirm the magnetism of the $NiCp_2$, we used X-ray Magnetic Circular Dichroism technique. The experiments were performend at synchrotron SOLEIL facilities, on the beamline DEIMOS. Those measurements consist in measuring the absoprtion of a circularly polarized light (x-rays) by the sample. The incident x-ray photons excite the core electrons of the metal of interest from the $2p$ orbitals to the unoccupied $3d$ orbitals. When those electrons de-excite, their energy is transferred to neighbour electrons which leave the material as Auger electrons. Those leaving electrons are flowing through the sample and

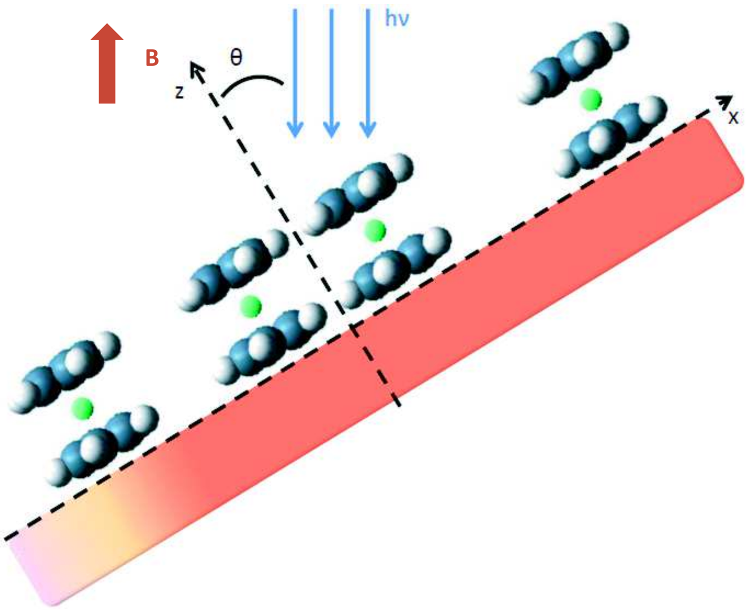

Figure A.2: **Geometry of the XMCD experiment.** The x and z directions are taken in 2 dimensions along the normal of the sample and its plane respectively. The angle θ describes the incidence angle of the x-ray light with respect to the molecule axis.

collected as an emitted current. The intensity of this collected current is directly proportionnal to the absorption of X-rays by the studied sample (Fig. A.1).

It has been shown that, for a fixed helicity ("right" or "left" polarization) of the incoming X-ray beam, spins polarized up and down with respect to the beam axis will have a different absorption rate [191, 192]. Thus, switching from a left to right polarization, we can investigate the average spin orientation of atoms on the sample, projected along the beam axis. The difference between the two adsorption spectra gives the so called XCMD signal. Using a proper method of analysis (sum rules [193]), one can then extract from this XMCD spectrum a value of the magnetic moment of the considered entity. Note that this kind of experiment has to be carried out under a magnetic field B (also oriented along the beam axis in our case), and that reversing the direction of this magnetic field would lead in an inversion of the XMCD spectrum sign.

In our case, we illuminated $NiCp_2$ molecules vertically adsorbed on a metallic crystal and defined the main axis of vertical molecule as z quantification axis (Fig. A.2). We obtained adsorption spectra with two peaks (similar to those presented for Co in the righ part of Fig.A.1) corresponding to the L_3 and L_2 edges of Ni, respectively located at 864 and 882 eV.

Appendix B

XMCD models

We present here a thermodynamic model of the behaviour of nickelocene molecule studied by XMCD. The model describes the magnetization of a spin $S = 1$ system with respect to temperature and magnetic field orientation and is compared to the experimental XMCD results (Fig. B.1). We started our model with the Hamiltonian described in chapter 5 :

$$\hat{H} = D\hat{S}_z^2 - g\mu_{\mathrm{B}}\mathbf{B} \cdot \hat{\mathbf{S}}. \tag{B.1}$$

where D represents the vertical anisotropy parameter (zero field splitting) and where the second term refers to the Zeeman splitting induced by the magnetic field B. Here, $g = 2$ is the gyromagnetic factor and μ_B is the Bohr magneton. According to the geometry of the XMCD experiment (appendix A), we projected the equation B.1 in an xz plane and obtained

$$\hat{H_S} = D\hat{S_z^2} - g\mu_B(B \cdot \hat{S}_z cos(\theta) + B \cdot \hat{S}_x sin(\theta)). \tag{B.2}$$

Using the transformation

$$\hat{S_x} = \frac{1}{2}(\hat{S_+} + \hat{S_-}), \tag{B.3}$$

it is possible to write the Hamiltoninan in the base $\{|S = 1, m_s = -1>, |S = 1, m_s = 0>, |S = 1, m_s = 1>\}$ as

$$\begin{pmatrix} D + Bcos(\theta) & \frac{\sqrt{2}}{2}Bsin(\theta) & 0 \\ \frac{\sqrt{2}}{2}Bsin(\theta) & 0 & \frac{\sqrt{2}}{2}Bsin(\theta) \\ 0 & \frac{\sqrt{2}}{2}Bsin(\theta) & D - Bcos(\theta) \end{pmatrix}. \tag{B.4}$$

XMCD measurements provide information about the average projection of the magnetisation along the beam axis $< \mu_{measured} >$, as detailled in the following expression:

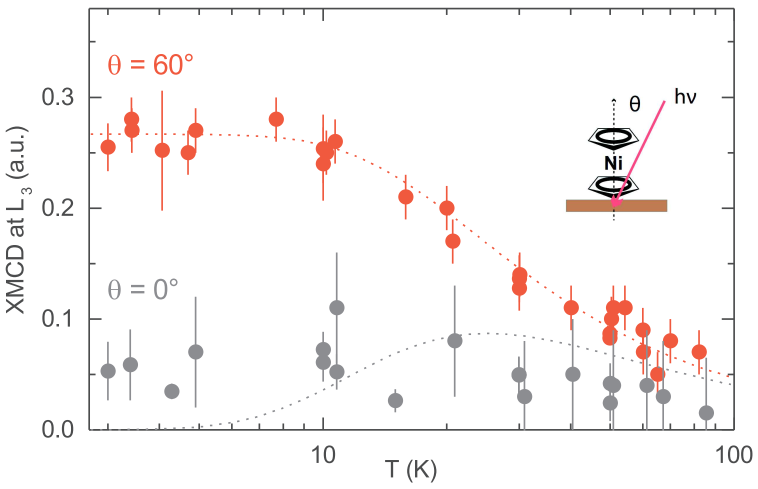

Figure B.1: **Data points of XMCD measurements on Isolated nickelocene.** The magnetic moment data (dots) are extracted from XMCD signals for each temperature. The black dots represents the the measurement for a 0° incidence angle and the red dots a 60° incidence angle.

$$< \mu_{measured} > \propto \frac{\mathbf{S} \cdot \mathbf{B}}{||\mathbf{B}||} = < \hat{S_z} > cos(\theta) + \frac{1}{2}(< \hat{S_+} + \hat{S_-} >) sin(\theta) \tag{B.5}$$

In our case, the averaging can be modelled within statistical physics. Let us introduce a 3D base {|j>} composed of eigenvectors of the hamiltonian H_S (Eq. B.2) and the corresponding eigenvalues $\{E_n\}$. The partition function associated to the thermal averaging of those energy states is

$$Z = \sum_n exp(\frac{-E_n}{k_B T}) \tag{B.6}$$

and the magnetization is given by

$$< \mu > = -\frac{\delta F}{\delta B} = k_B T \frac{\delta ln(Z)}{\delta B} \tag{B.7}$$

where F is the free energy of the system and Z the partition function expressed in Eq. B.6.

Bibliography

[1] M. Julliere, Phys. Lett. A **3**, 225 (2012).

[2] L. Wang, Z. Cai, J. Wang, J. Lu, G. Luo, L. Lai, J. Zhou, R. Qin, Z. Gao, D. Yu, G. Li, W. N. Mei, and S. Sanvito, Nano Lett. **8**, 3640 (2008).

[3] P. Wahl, L. Diekhoner, M. A. Schneider, and K. Kern, Rev. Sci. Ins. 043104 (2008).

[4] A. J. Heinrich, J. A. Gupta, C. P. Lutz, and D. M. Eigler, Science **306**, 466 (2004).

[5] C. F. Hirjibehedin, C.-Y. Lin, A. F. Otte, M. Ternes, C. P. Lutz, B. A. Jones, and A. J. Heinrich, Science **317**, 1199 (2007).

[6] P. Baltzer, A. Furrer, J. Hulliger, and A. Stebler, Inorg. Chem. **27**, 1543 (1988).

[7] N. F. Mott, Proc. Roy. Soc. A **156**, 699 (1936).

[8] R. Meservey, P. M. Tedrow, and P. Fulde, Phys. Rev. Lett. **25**, 1270 (1970).

[9] P. M. Tedrow and R. Meservey, Phys. Rev. Lett. **26**, 192 (1971).

[10] I. I. Mazin, Phys. Rev. Lett. **83**, 1427 (1999).

[11] J. S. Moodera, L. R. Kinder, T. M. Wong, and R. Meservey, Phys. Rev. Lett. **74**, 3273 (1995).

[12] M. N. Baibich, J. M. Broto, A. Fert, F. Nguyen Van Dau, F. Petroff, P. Eitenne, G. Creuzet, A. Friederich, and C. J., Phys. Rev. Lett. **61**, 2472 (1988).

[13] G. Binasch, P. Grünberg, F. Saurenbach, and W. Zinn, Phys. Rev. B **39**, 4828 (1989).

[14] I. Žutić, J. Fabian, and S. Das Sarma, Rev. Mod. Phys. **76**, 323 (2004).

[15] V. A. Dediu, L. E. Hueso, I. Bergenti, and C. Taliani, Nat Mater **8**, 707 (2009).

[16] A. R. Rocha, V. M. Garcia-suarez, S. W. Bailey, C. J. Lambert, J. Ferrer, and S. Sanvito, Nat. Mater. **4**, 335 (2005).

[17] S. Sanvito, Chem. Soc. Rev. **40**, 3336 (2011).

[18] J. R. Hauptmann, J. Paaske, and P. E. Lindelof, Nat. Phys. **4**, 373 (2008).

[19] M. Urdampilleta, S. Klyatskaya, J.-P. Cleuziou, M. Ruben, and W. Wernsdorfer, Nat. Mater. **10**, 502 (2011).

[20] S. Schmaus, A. Bagrets, Y. Nahas, T. K. Yamada, A. Bork, M. Bowen, B. E., F. Evers, and W. Wulfhekel, Nat. Nanotech. **6**, 185 (2011).

[21] C. Barraud, P. Seneor, R. Mattana, S. Fusil, K. Bouzehouane, C. Deranlot, P. Graziosi, L. Hueso, I. Bergenti, V. Dediu, F. Petroff, and A. Fert, Nat. Phys. **6**, 615 (2010).

[22] S. Sanvito, Nat. Phys. **6**, 562 (2010).

[23] A. Zhao, Q. Li, L. Chen, H. Xiang, W. Wang, S. Pan, B. Wang, X. Xiao, J. Yang, J. G. Hou, and Q. Zhu, Science **309**, 1542 (2005).

[24] L. Gao, W. Ji, Y. B. Hu, Z. H. Cheng, Z. T. Deng, Q. Liu, N. Jiang, X. Lin, W. Guo, S. X. Du, W. A. Hofer, X. C. Xie, and H.-J. Gao, Phys. Rev. Lett. **99**, 106402 (2007).

[25] J. J. Parks, A. R. Champagne, T. A. Costi, W. W. Shum, A. N. Pasupathy, E. Neuscamman, S. Flores-Torres, P. S. Cornaglia, A. A. Aligia, C. A. Balseiro, G. K.-L. Chan, H. D. Abruna, and D. C. Ralph, Science **328**, 1370 (2010).

[26] T. Komeda, H. Isshiki, J. Liu, Y.-F. Zhang, N. Lorente, K. Katoh, B. K. Breedlove, and M. Yamashita, Nat. Commun. **2**, 217 (2011).

[27] T. G. Gopakumar, F. Matino, H. Naggert, A. Bannwarth, F. Tuczek, and R. Berndt, Angew. Chem. Int. Ed. **51**, 6262 (2012).

[28] T. Miyamachi, M. Gruber, V. Davesne, M. Bowen, S. B., L. Joly, F. Scheurer, G. Rogez, T. K. Yamada, P. Ohresser, E. Beaurepaire, and W. Wulfhekel, Nat. Commun. **3**, 938 (2012).

[29] B. W. Heinrich, G. Ahmadi, V. L. Müller, L. Braun, J. I. Pascual, and K. J. Franke, Nano Lett. **13**, 4840 (2013).

[30] R. Robles, N. Lorente, H. Isshiki, J. Liu, K. Katoh, B. K. Breedlove, M. Yamashita, and T. Komeda, Nano Lett. **12**, 3609 (2012).

[31] C. Krull, R. Robles, A. Mugarza, and P. Gambardella, Nat. Mater. **12**, 337 (2013).

[32] S. Stepanow, A. L. Rizzini, C. Krull, J. Kavich, J. C. Cezar, F. Yakhou-Harris, P. M. Sheverdyaeva, P. Moras, C. Carbone, G. Ceballos, A. Mugarza, and P. Gambardella, J. Am. Chem. Soc. **136**, 5451 (2014).

[33] M. Ormaza, R. Robles, N. Bachellier, P. Abufager, N. Lorente, and L. Limot, Nano Lett. **16**, 588 (2016).

[34] L. Bogani and W. Wernsdorfer, Nat. Mater. **7**, 179 (2008).

[35] G. D. Scott and D. Natelson, ACS Nano **4**, 3560 (2010).

[36] N. Atodiresei, J. Brede, P. Lazić, V. Caciuc, G. Hoffmann, R. Wiesendanger, and S. Blügel, Phys. Rev. Lett. **105**, 066601 (2010).

[37] M. Bode, M. Heide, K. von Bergmann, P. Ferriani, S. Heinze, G. Bihlmayer, A. Kubetzka, O. Pietzsch, S. Blugel, and R. Wiesendanger, Nature **447**, 190 (2007).

[38] Y. Yayon, V. W. Brar, L. Senapati, S. C. Erwin, and M. F. Crommie, Phys. Rev. Lett. **99**, 067202 (2007).

[39] D. Serrate, P. Ferriani, Y. Yoshida, S.-W. Hla, M. Menzel, K. von Bergmann, S. Heinze, A. Kubetzka, and R. Wiesendanger, Nat. Nanotech. **5**, 350 (2010).

[40] A. A. Khajetoorians, J. Wiebe, B. Chilian, and R. Wiesendanger, Science **332**, 1062 (2011).

[41] C. Iacovita, M. V. Rastei, B. W. Heinrich, T. Brumme, J. Kortus, L. Limot, and J. P. Bucher, Phys. Rev. Lett. **101**, 116602 (2008).

[42] J. Brede, N. Antodiresei, S. Kuck, P. Lazié, V. Caciuc, Y. Morikawa, G. Hoffmann, B. S., and R. Wiesendanger, Phys. Rev. Lett **105**, 047204 (2010).

[43] H. Wende, M. Bernien, J. Luo, C. Sorg, N. Ponpandian, J. Kurde, J. Miguel, M. Piantek, X. Xu, P. Eckhold, W. Kuch, K. Baberschke, P. M. Panchmatia, B. Sanyal, P. M. Oppeneer, and O. Eriksson, Nat. Mater. **6**, 516 (2007).

[44] M. Gruber, F. Ibrahim, S. Boukari, H. Isshiki, L. Joly, M. Peter, M. Studniarek, V. Da Costa, H. Jabbar, V. Davesne, U. Halisdemir, J. Chen, J. Arabski, E. Otero, F. Choueikani, K. Chen, P. Ohresser, W. Wulfhekel, F. Scheurer, W. Weber, M. Alouani, E. Beaurepaire, and M. Bowen, Nat. Mater. **14**, 981 (2015).

[45] M. Gruber, F. Ibrahim, S. Boukari, L. Joly, V. Da Costa, M. Studniarek, M. Peter, H. Isshiki, H. Jabbar, V. Davesne, J. Arabski, E. Otero, F. Choueikani, K. Chen, P. Ohresser, W. Wulfhekel, F. Scheurer, E. Beaurepaire, M. Alouani, W. Weber, and M. Bowen, Nano Lett. **15**, 7921 (2015).

[46] T. A. Albright, J. K. Burdett, and M.-H. Whangbo, *Orbital Interactions in Chemistry, 2nd Edition* (Wiley Online Library, Hoboken, 2013).

[47] P. Pritchard, S. Simpson, E. Zurek, and J. Autschbach, J. Chem. Educ **91**, 1058 (2014).

[48] L. Zhou, S.-W. Yang, M.-F. Ng, M. B. Sullivan, V. B. C., and L. Shen, J. Am. Chem. Soc. **130**, 4023 (2008).

[49] R. Liu, S.-H. Ke, H. U. Baranger, and W. Yang, Nano Lett. **5**, 1959 (2005).

[50] Z. Yi, X. Shen, L. Sun, Z. Shen, S. Hou, and S. Sanvito, ACS Nano **4**, 2274 (2010).

[51] P. Abufager, R. Robles, and N. Lorente, J. Phys. Chem. C **119**, 12119 (2015).

[52] V. V. Maslyuk, A. Bagrets, V. Meded, A. Arnold, F. Evers, M. Brandbyge, T. Bredow, and I. Mertig, Phys. Rev. Lett. **97**, 097201 (2006).

[53] M. Koleini, M. Paulsson, and M. Brandbyge, Phys. Rev. Lett. **98**, 197202 (2007).

[54] C. Morari, H. Allmaier, F. Beiuşeanu, T. Jurcuţ, and L. Chioncel, Phys. Rev. B **85**, 085413 (2012).

[55] X. Shen, Z. Yi, Z. Shen, X. Zhao, J. Wu, S. Hou, and S. Sanvito, Nanotechnology **20**, 385401 (2009).

[56] J.-F. Yang, L. Zhou, Q. Han, and X.-F. Wang, J. Phys. Chem. C **116**, 19996 (2012).

[57] G. Binning, H. Roher, C. Gerber, and E. Weibel, Appl. Phys. Lett. 178 (1982).

[58] G. Binning, H. Roher, C. Gerber, and E. Weibel, Phys..Rev. Lett. 57 (1982).

[59] G. Binning, H. Roher, C. Gerber, and E. Weibel, Phys.Rev. Lett. 120 (1983).

[60] J. A. Applebaum and W. F. Brinkman, Phys. Rev. 464 (1969).

[61] J. Tersoff and D. R. Hamann, Phys. Rev. Lett. **50**, 1998 (1983).

[62] J. Tersoff and D. R. Hamann, Phys. Rev. B **31**, 805 (1985).

[63] R. J. Hamers, *Scanning Tunneling Microscopy ans Spectroscopy. Theory, Techniques and Applications* (VHC, New York, ADDRESS, 1993).

[64] R. Weisendanger, *Scanning Probe Microscopy. Methods and Applications* (Cambridge University Press, Cambridge, UK, ADDRESS, 1994).

[65] V. A. Ukraintsev, Phys. Rev.B 11176 (1996).

[66] C. J. Chen, *Introdution to Scanning Tunneleing Microscopy* (Oxford science publications, ADDRESS, 1993).

[67] R. Landauer, IBM J. Res. Dev. 223 (1957).

[68] M. Büttiker, IBM J. Res. Dev. 63 (1988).

[69] R. Landauer, Philos. Mag. 863 (1970).

[70] R. Landauer, Phys. Lett. A 91 (1981).

[71] M. Buttiker, Y. Imry, L. R., and S. Pinhas, Phys. Rev. B 6207 (1985).

[72] L. Limot, E. Pehlke, J. Kröger, and R. Berndt, Phys. Rev. Lett. **94**, 036805 (2005).

[73] R. B. J. Kroger, H. Jensen, New J. Phys. 153 (2007).

[74] C. Iacovita, *Spin dependent tunneling into single cobalt-phtolocyanine molecules* (PhD thesis, Université de Strasbourg, ADDRESS, 2009).

[75] D. Choi, *Kondo effect and detection of a spin polarized current i a quantum point contact* (PhD thesis, Université de Strasbourg, ADDRESS, 2012).

[76] Y.-H. Zhang, P. Wahl, and K. Kern, Nano lett. **9**, 3838 (2011).

[77] K. W. Kolasinski, *Surface Science: Foundations of Catalysis and Nanoscience* (Oxford science publications, ADDRESS, 1993).

[78] B. W. Heinrich, M. V. Rastei, D.-J. Choi, T. Frederiksen, and L. Limot, Phys. Rev. Lett. **107**, 246801 (2011).

[79] H. B. F. D. Natterer, F. Patthey, Phys. Rev. Lett. 175303 (2013).

[80] J. Kroger, L. Limot, H. Jensen, R. Berndt, S. Crampin, and E. Pehlke, Progress in surface Science 26 (2005).

[81] J. Klein, A. Leger, M. Belin, M. Defourneau, and M. J. L. Sangster, Phys. Rev. B 2336 (1973).

[82] J. Lambe and R. C. Jaklevic, Physical Review **165**, 821 (1968).

[83] J. C. Oberg, M. R. Calvo, F. Delgado, M. Moro-Lagares, D. Serrate, D. Jacob, J. Fernández-Rossier, and C. Hirjibehedin, Nat. Nanotech. 64 (2013).

[84] W. Salaneck, Y. Sawada, E. Burstein, and M. Nelson, Phys. Rev. Lett. **20**, 1097 (1968).

[85] P. Hansma, *Tunneling Spectroscopy* (Plenum, New York, 1982).

[86] G. Binnig, N. Garcia, and H. Rohrer, Phys. Rev. B **32**, 1336 (1985).

[87] B. N. J. Persson and A. Baratoff, Phys. Rev. Lett. **59**, 339 (1987).

[88] B. C. Stipe, M. A. Rezaei, and W. Ho, Science **279**, 1907 (1998).

[89] B. C. Stipe, M. A. Rezaei, and W. Ho, Science **280**, 1732 (1998).

[90] B. C. Stipe, M. A. Rezaei, and W. Ho, Phys. Rev. Lett. **81**, 1263 (1998).

[91] N. Lorente and J.-P. Gauyacq, Phys. Rev. Lett. **103**, 176601 (2009).

[92] J.-P. Gauyacq, F. D. Novaes, and N. Lorente, Phys. Rev. B **81**, 165423 (2010).

[93] M. Paulsson, T. Frederiksen, H. Ueba, N. Lorente, and M. Brandbyge, Phys. Rev. Lett. **100**, 226604 (2008).

[94] M. Persson, Phys. Rev. Lett. **103**, 050801 (2009).

[95] J. Fernández-Rossier, Phys. Rev. Lett. **102**, 256802 (2009).

[96] F. Donati, S. Rusponi, S. Stepanow, C. Wäckerlin, A. Singha, L. Persichetti, R. Baltic, K. Diller, F. Patthey, E. Fernandes, J. Dreiser, Ž. Šljivančanin, K. Kummer, C. Nistor, P. Gambardella, and H. Brune, Science **352**, 318 (2016).

[97] N. Tsukahara, K.-I. Noto, M. Ohara, S. Shiraki, N. Takagi, Y. Takata, J. Miyawaki, M. Taguchi, A. Chainani, S. Shin, and M. Kawai, Phys. Rev. Lett. **102**, 167203 (2009).

[98] C. F. Hirjibehedin, C. P. Lutz, and A. J. Heinrich, Science **312**, 1021 (2006).

[99] J. C. Oberg, M. R. Calvo, F. Delgado, M. Moro-Lagares, D. Serrate, D. Jacob, J. Fernández-Rossier, and C. F. Hirjibehedin, Nat. Nanotech. **9**, 64 (2014).

[100] K. Yosida, *Theory of Magnetism* (Springer-Verlag Berlin Heidelberg, Heidelberger Platz 3, 14197 Berlin, 1996).

[101] X. Chen, Y.-S. Fu, S.-H. Ji, T. Zhang, P. Cheng, X.-C. Ma, X.-L. Zou, W.-H. Duan, J.-F. Jia, and Q.-K. Xue, Phys. Rev. Lett. **101**, 197208 (2015).

[102] A. A. Khajetoorians, B. Chilian, J. Wiebe, S. Schuwalow, F. Lechermann, and R. Wiesendanger, Nature **467**, 1084 (2010).

[103] B. Bryant, R. Toskovic, A. Ferron, J. L. Lado, A. Spinelli, J. Fernández-Rossier, and A. F. Otte, Nano Lett. **15**, 6542 (2015).

[104] J. P. Gauyacq and N. Lorente, Phys. Rev. B **83**, 035418 (2011).

[105] F. D. Novaes, N. Lorente, and J.-P. Gauyacq, Phys. Rev. B **82**, 155401 (2010).

[106] F. Delgado, J. J. Palacios, and J. Fernández-Rossier, Phys. Rev. Lett. **104**, 026601 (2010).

[107] S. Loth, K. v. Bergmann, M. Ternes, A. F. Otte, C. P. Lutz, and A. J. Heinrich, Nat. Phys. **6**, 340 (2010).

[108] S. Loth, M. Etzkorn, C. P. Lutz, D. M. Eigler, and A. J. Heinrich, Science **329**, 1628 (2010).

[109] B. W. Heinrich, L. Braun, J. I. Pascual, and K. J. Franke, Nat. Phys. **9**, 765 (2013).

[110] A. A. Khajetoorians, S. Lounis, B. Chilian, A. T. Costa, L. Zhou, D. L. Mills, J. Wiebe, and R. Wiesendanger, Phys. Rev. Lett. **106**, 037205 (2011).

[111] P. W. Anderson, Phys. Rev. **124(1)**, 41 (1961).

[112] W. J. de Haas and J. van den Berg, Physica III **6**, 440 (1936).

[113] J. Kondo, Progr. Theor. Exp. Phys. **32**, 37 (1964).

[114] A. A. Abrikosov, Physics **5**, 2 (1965).

[115] J. R. Schrieffer and P. A. Wolff, Phys. Rev. **149**, 491 (1966).

[116] D. Goldhaber-Gordon, H. Shtrikman, D. Mahalu, D. Abusch-Magder, U. Meirav, and M. A. Kastner, Nature **391**, 156 (1998).

[117] S. M. Cronenwett, T. H. Oosterkamp, and L. P. Kouwenhoven, Science **281**, 540 (1998).

[118] J. Li, W.-D. Schneider, R. Berndt, and B. Delley, Phys. Rev. Lett. **80**, 2893 (1998).

[119] V. Madhavan, W. Chen, T. Jamneala, M. F. Crommie, and N. S. Wingreen, Science **280**, 567 (1998).

[120] P. Wahl, L. Diekhöner, M. A. Schneider, L. Vitali, G. Wittich, and K. Kern, Phys. Rev. Lett. **93**, 176603 (2004).

[121] D.-J. Choi, M. V. Rastei, P. Simon, and L. Limot, Phys. Rev. Lett. **108**, 266803 (2012).

[122] D.-J. Choi, S. Guissart, M. Ormaza, N. Bachellier, O. Bengone, P. Simon, and L. Limot, Nano Lett. **16**, 6298 (2016).

[123] P. P. Baruselli, R. Requist, A. Smogunov, M. Fabrizio, and E. Tosatti, Phys. Rev. B **92**, 045119 (2015).

[124] N. Knorr, M. Schneider, L. Diekhöner, P. Wahl, and K. Kern, Phys. Rev. Lett. **88**, 096804 (2002).

[125] A. Gumbsch, G. Barcaro, M. G. Ramsey, S. Surnev, A. Fortunelli, and F. P. Netzer, Phys. Rev. B **81**, 165420 (2010).

[126] M. Plihal and J. W. Gadzuk, Phys. Rev. B **63**, 085404 (2001).

[127] A. C. Seridonio, F. M. Souza, and I. A. Shelykh, J. Phys.: Condens. Matter **21**, 095003 (2009).

[128] H. Pruser, M. Wenderoth, P. E. Dargel, A. Weismann, R. Peters, T. Pruschke, and R. G. Ulbrich, Nat. Phys. **7**, 203 (2011).

[129] H. Frota, Phys. Rev. B **45**, 1096 (1992).

[130] M. Ternes, New J. Phys. **17**, 063016 (2015).

[131] J.-P. Gauyacq, N. Lorente, and F. D. Novaes, Prog. Surf. Sci. **87**, 63 (2012).

[132] A. Hurley, N. Baadji, and S. Sanvito, Phys. Rev. B **84**, 115435 (2011).

[133] R. Korytár, N. Lorente, and J.-P. Gauyacq, Phys. Rev. B **85**, 125434 (2012).

[134] A. Lodi Rizzini, C. Krull, T. Balashov, J. J. Kavich, A. Mugarza, P. S. Miedema, P. K. Thakur, V. Sessi, S. Klyatskaya, M. Ruben, S. Stepanow, and P. Gambardella, Phys. Rev. Lett. **107**, 177205 (2011).

[135] D. Welipitiya, A. Green, J. P. Woods, P. A. Dowben, B. W. Robertson, D. Byun, and J. Zhang, J. Appl. Phys. **79**, 8730 (1996).

[136] C. Waldfried, D. Welipitiya, C. W. Hutchings, H. S. V. de Silva, G. A. Gallup, P. A. Dowben, W. W. Pai, J. Zhang, J. F. Wendelken, and N. M. Boag, J. Phys. Chem. B **101**, 9782 (1997).

[137] C. M. Woodbridge, D. L. Pugmire, R. C. Johnson, N. M. Boag, and M. A. Langell, J. Phys. Chem. B **104**, 3085 (2000).

[138] P. Durston and R. Palmer, Surf. Sci. **400**, 277 (1998).

[139] K. Svensson, T. Bedson, and R. Palmer, Surf. Sci. **451**, 250 (2000).

[140] P. Dowben, C. Waldfried, T. Komesu, D. Welipitiya, T. McAvoy, and E. Vescovo, Chem. Phys. Lett. **283**, 44 (1998).

[141] K.-F. Braun, V. Iancu, N. Pertaya, K.-H. Rieder, and S.-W. Hla, Phys. Rev. Lett. **96**, 246102 (2006).

[142] R. C. Quardokus, N. A. Wasio, R. P. Forrest, C. S. Lent, S. A. Corcelli, J. A. Christie, K. W. Henderson, and S. A. Kandel, Phys. Chem. Chem. Phys. **15**, 6973 (2013).

[143] N. A. Wasio, R. C. Quardokus, R. P. Forrest, C. S. Lent, S. A. Corcelli, J. A. Christie, K. W. Henderson, and S. A. Kandel, Nature **507**, 86 (2014).

[144] J. Berger, K. Kosmider, O. Stetsovych, M. Vondracek, P. Hapala, E. J. Spadafora, M. Svec, and P. Jelinek, J. Phys. Chem. C **120**, 21955 (2016).

[145] B. W. Heinrich, L. Limot, M. V. Rastei, C. Iacovita, J. P. Bucher, D. M. Djimbi, C. Massobrio, and M. Boero, Phys. Rev. Lett. **107**, 216801 (2011).

[146] M. Gruber, V. Davesne, M. Bowen, S. Boukari, E. Beaurepaire, W. Wulfhekel, and T. Miyamachi, Phys. Rev. B. **89**, 195415 (2014).

[147] D. Zhong, K. Wedeking, T. Blömker, G. Erker, H. Fuchs, and L. Chi, ACS Nano **4**, 1997 (2010).

[148] N. Néel, L. Limot, J. Kröger, and R. Berndt, Phys. Rev. B **77**, 125431 (2008).

[149] G. Kresse and J. Furthmüller, Comput. Mater. Sci. **6**, 15 (1996).

[150] G. Kresse and D. Joubert, Phys. Rev. B **59**, 1758 (1999).

[151] J. P. Perdew, K. Burke, and M. Ernzerhof, Phys. Rev. Lett. **77**, 3865 (1996).

[152] S. Grimme, J. Comput. Chem. **27**, 1787 (2006).

[153] A. Haaland, J. E. Nilsson, T. Olson, and T. Norin, Acta Chem. Scand. **22**, 2653 (1968).

[154] N. Mohammadi, A. Ganesan, C. T. Chantler, and F. Wang, J. Organomet. Chem. **713**, 51 (2012).

[155] S. Coriani, A. Haaland, T. Helgaker, and P. Jørgensen, ChemPhysChem **7**, 245 (2006).

[156] J. D. Dunitz, L. E. Orgel, and A. Rich, Acta Crystallogr. **9**, 373 (1956).

[157] D. M. Eigler and E. K. Schweizer, Nature **344**, 524 (1990).

[158] G. Schull, T. Frederiksen, M. Brandbyge, and R. Berndt, Phys. Rev. Lett. **103**, 206803 (2009).

[159] C. Chiutu, A. M. Sweetman, A. J. Lakin, A. Stannard, S. Jarvis, L. Kantorovich, J. L. Dunn, and P. Moriarty, Phys. Rev. Lett. **108**, 268302 (2012).

[160] M. Ormaza, P. Abufager, N. Bachellier, R. Robles, M. Verot, T. Le Bahers, M.-L. Bocquet, N. Lorente, and L. Limot, J. Phys. Chem. Lett. **6**, 395 (2015).

[161] J. A. Stroscio and R. J. Celotta, Science **306**, 242 (2004).

[162] P. Abufager, R. Robles, and N. Lorente, J. Phys. Chem. C **119**, 12119 (2015).

[163] V. Madhavan, W. Chen, T. Jamneala, M. F. Crommie, and N. S. Wingreen, Phys. Rev. B **64**, 165412 (2001).

[164] F. Olsson, M. Persson, A. Borisov, J.-P. Gauyacq, J. Lagoute, and S. Folsch, Phys. Rev. Lett. **93**, (2004).

[165] V. Iancu, K.-F. Braun, K. Schouteden, and C. Van Haesendonck, Phys. Rev. Lett. **113**, 106102 (2014).

[166] M.-L. Bocquet, H. Lesnard, S. Monturet, and N. Lorente, in *Computational Methods in Catalysis and Materials Science*, edited by R. A. van Santen and P. Sautet (Wiley-VCH, Weinheim, Germany, 2009), pp. 199–219.

[167] D. Gatteschi, R. Sessoli, and J. Villain, *Molecular Nanomagnets* (OUP Oxford, ADDRESS, 2006).

[168] M. N. Leuenberger and D. Loss, Nature **410**, 789 (2001).

[169] P. Gambardella, S. Rusponi, M. Veronese, S. S. Dhesi, C. Grazioli, A. Dallmeyer, I. Cabria, R. Zeller, P. H. Dederichs, K. Kern, C. Carbone, and H. Brune, Science **300**, 1130 (2003).

[170] A. S. Zyazin, J. W. G. van den Berg, E. A. Osorio, H. S. J. van der Zant, N. P. Konstantinidis, M. Leijnse, M. R. Wegewijs, F. May, W. Hofstetter, C. Danieli, and A. Cornia, Nano Lett. **10**, 3307 (2010).

[171] S. Thiele, F. Balestro, R. Ballou, S. Klyatskaya, M. Ruben, and W. Wernsdorfer, Science **344**, 1135 (2014).

[172] I. G. Rau, S. Baumann, S. Rusponi, F. Donati, S. Stepanow, L. Gragnaniello, J. Dreiser, C. Piamonteze, F. Nolting, S. Gangopadhyay, O. R. Albertini, R. M. Macfarlane, C. P. Lutz, B. A. Jones, P. Gambardella, A. J. Heinrich, and H. Brune, Science **344**, 988 (2014).

[173] A. A. Khajetoorians, M. Valentyuk, M. Steinbrecher, T. Schlenk, A. Shick, J. Kolorenc, A. I. Lichtenstein, T. O. Wehling, R. Wiesendanger, and J. Wiebe, Nat. Nanotech. **10**, 958 (2015).

[174] P. Jacobson, T. Herden, M. Muenks, G. Laskin, O. Brovko, V. Stepanyuk, M. Ternes, and K. Kern, Nat. Commun. **6**, 8536 (2015).

[175] S. Loth, K. von Bergmann, M. Ternes, A. F. Otte, C. P. Lutz, and A. J. Heinrich, Nat. Phys. **6**, 340 (2010).

[176] S. Loth, M. Etzkorn, C. P. Lutz, D. M. Eigler, and A. J. Heinrich, Science **329**, 1628 (2010).

[177] S. Yan, D.-J. Choi, J. A. Burgess, and S. R.-P. ans S. Loth, Nat. Nanotech. **10**, 40 (2015).

[178] L. Gross, F. Mohn, N. Moll, P. Liljeroth, and G. Meyer, Science **325**, 1110 (2009).

[179] C. Weiss, C. Wagner, C. Kleimann, M. Rohlfing, F. S. Tautz, and R. Temirov, Phys. Rev. Lett. **105**, 086103 (2010).

[180] G. Schull, Y. J. Dappe, C. González, H. Bulou, and R. Berndt, Nano Lett. **11**, 3142 (2011).

[181] C.-L. Chiang, C. Xu, Z. Han, and W. Ho, Science **344**, 885 (2014).

[182] J. Guo, J.-T. Lü, Y. Feng, J. Chen, J. Peng, Z. Lin, X. Meng, Z. Wang, X.-Z. Li, E.-G. Wang, and Y. Jiang, Science **352**, 321 (2016).

[183] D. Welipitiya, C. Borca, C. Waldfried, C. Hutchings, L. Sage, C. Woodbridge, and P. Dowben, Surf. Sci. **393**, 34 (1997).

[184] D. Welipitiya, C. Waldfried, C. N. Borca, P. A. Dowben, N. M. Boag, H. Jiang, I. Gobulukoglu, and B. W. Robertson, Surf. Sci. **418**, 466 (1998).

[185] C. N. Borca, D. Welipitiya, P. A. Dowben, , and N. M. Boag, J. Phys. Chem. B **104**, 1047 (2000).

[186] D. Pugmire, C. Woodbridge, N. Boag, and M. Langell, Surf. Sci. **472**, 155 (2001).

[187] R. Prins, J. van Voorst, and C. Schinkel, Chem. Phys. Lett. **1**, 54 (1967).

[188] S. Li, Y. M. Hamrick, R. J. V. Zee, and W. W. Jr., J. Am. Chem. Soc. **114**, 4433 (1992).

[189] M. Brandbyge, J.-L. Mozos, P. Ordejón, J. Taylor, and K. Stokbro, Phys. Rev. B **65**, 165401 (2002).

[190] J. Stöhr and H. C. Siegmann, *Magnetism From Fundamentals to Nanoscale Dynamics* (Springer-Verlag, ADDRESS, 2006).

[191] E. J. L. and E. A. Stern, Phys. Rev. B **12**, 5016 (1975).

[192] G. Schütz, W. W. Wagner, W, P. Kienle, R. Zeller, R. Frahm, and G. Materlik, Phys. Rev. Lett. **58**, 737 (1987).

[193] C. T. Chen, Y. U. Idzerda, H.-J. Lin, N. V. Smith, G. Meigs, E. Chaban, G. H. Ho, E. Pellegrin, and F. Sette, Phys. Rev. Lett. **75**, 152 (1995).

List of publications

1 . "Assembly of Ferrocene Molecules on Metal Surfaces Revisited", M. ORMAZA, P. ABUFAGER, N. BACHELLIER, R. ROBLES, M. VEROT, T. LE BAHERS, M.-L. BOCQUET, N. LORENTE, L. LIMOT. *J. Phys. Chem. Lett.*, 6: 395-400 (2015).

2. "On-Surface Engineering of a Magnetic Organometallic Nanowire", M. ORMAZA, R. ROBLES, N. BACHELLIER, P. ABUFAGER, N. LORENTE, L. LIMOT. *Nano Lett.*, 16(1): 588-593 (2016).

3. "Unveiling nickelocene bonding to a noble metal surface", N. BACHELLIER, M. ORMAZA, M. N. FARAGGI, B. VERLHAC, M. VEROT, T. LE BAHERS, M.-L. BOCQUET, L. LIMOT. *Phys. Rev. B*, 93(19): 195403 (2016).

4. "Kondo Resonance of a Co Atom Exchange Coupled to a Ferromagnetic Tip" D.-J. CHOI, S. GUISSART, M. ORMAZA, N. BACHELLIER, O. BENGONE, P. SIMON, L. LIMOT. *Nano Lett.*, 16: 6298-6302 (2016).

5. "Single-molecule enhanced spin-flip detection", M. ORMAZA, N. BACHELLIER, M. N. FARAGGI, B. VERLHAC, P. ABUFAGER, P. OHRESSER, L. JOLY, M. ROMEO, F. SCHEURER, M.-L. BOCQUET, N. LORENTE, L. LIMOT. *submitted to Nano Lett.* (2017).

List of presentations

1. Poster "Customizing metallocene layers on Cu(111)", N. BACHELLIER, M. ORMAZA, P. ABUFAGER, R. ROBLES, M. VEROT, T. LE BAHERS, M.-L. BOCQUET N. LORENTE, L. LIMOT. *SPINMOL2014*, Ascona, Switzerland, October 2014. **Best poster award**.

2. Oral presentation "Metallocene adsorption and customization on copper", N. BACHELLIER, M. ORMAZA, P. ABUFAGER, R. ROBLES, M. VEROT, T. LE BAHERS, M.-L. BOCQUET N. LORENTE, L. LIMOT. *Deutsche Physikalische Gesellschaft*, Berlin, Germany, March 2015.

3. Oral presentation "Spin detection in functionalized ferrocene", N. BACHELLIER, M. ORMAZA, P. ABUFAGER, R. ROBLES, M. VEROT, T. LE BAHERS, M.-L. BOCQUET N. LORENTE, L. LIMOT. *European Conference On Surface Science*, Barcelona, Spain, September 2015.

4. Poster. " On-Surface Engineering of a Magnetic Organometallic Nanowire", B. VERLHAC, N. BACHELLIER, M. ORMAZA, P. ABUFAGER, R. ROBLES, M. VEROT, T. LE BAHERS, M.-L. BOCQUET N. LORENTE, L. LIMOT. European Conference On Surface Science, Grenoble, France, September 2016.

5. Oral presentation "Portability of a molecular spin", N. BACHELLIER, M. ORMAZA, M. N.FARAGGI, B. VERLHAC, P. ABUFAGER, P. OHRESSER, L. JOLY, M. ROMEO, F. SCHEURER, M.-L. BOCQUET, N. LORENTE, L. LIMOT. European Conference On Surface Science, Grenoble, France, September 2016. **SFV “Michel Cantarel” student grant award**.

Nicolas Bachellier

On surface spin detection and doping of metallocenes

Résumé

Le sujet principal de cette thèse est l'étude de métallocènes déposés sur une surface de cuivre. Leurs adsorptions et propriétés électroniques sont expérimentalement étudiées par microscopie à effet tunnel (STM) et spectroscopie par effet tunnel (STS). Nos résultats ont été validés par des calculs se basant sur la théorie de la fonctionnelle de la densité (DFT).

Plus précisément, nous avons étudié la façon dont le ferrocène $FeC_{10}H_{10}$ et le nickelocène $NiC_{10}H_{10}$ s'adsorbent sur le cuivre. Nous avons découvert que ces métallocènes forment spontanément des réseaux alternant molécules horizontales et verticales. Nous avons ensuite modifié la structure du ferrocène par l'ajout d'un atome de cobalt et caractérisé les propriétés magnétiques de la nouvelle molécule ainsi créée, notamment l'apparition d'un effet Kondo témoignant de l'apparition de propriétés magnétiques au sein de la molécule.

L'étude spectroscopique du nickelocène a révélé une excitation de la molécule à basse énergie. Cette excitation se traduit par une réorientation du moment de spin de la molécule, passant d'une orientation perpendiculaire à l'axe principal de la molécule à une orientation parallèle à cet axe. Nous avons finalement transféré un nickelocène sur la pointe STM et utilisé cette pointe moléculaire pour sonder les états d'une seconde molécule. Nous avons alors obtenu une double excitation de spin dans notre jonction tunnel, avec une augmentation significative de la conductance due aux excitations.

Mots clés : STM, STS, IETS, magnétisme, électronique moléculaire, excitation de spin, molécules uniques, métallocène.

Résumé en anglais

The main subject of this PhD thesis is the study of metallocenes deposited on copper surfaces. Their adsorptions and electronic properties are experimentally studied by scanning tunnelling microscopy (STM) and scanning tunnelling spectroscopy (STS). Our results were confirmed by density functional theory (DFT) computations.

More precisely, we studied how ferrocene $FeC_{10}H_{10}$ and nickelocene $NiC_{10}H_{10}$ are adsorbed on copper. We found that these metallocenes spontaneously create networks alternating horizontal and vertical molecules. We added a cobalt atom to the ferrocene in order to modify its structure and we characterized the magnetic properties of the new molecule we created, in particular the appearance of a Kondo effect showing that magnetic properties appeared in the molecule.

The spectroscopic study of nickelocene revealed an excitation of the molecule at low bias. This excitation consist in a change in the spin orientation of the molecule, going from an orientation perpendicular to the main molecule axis to an orientation parallel to this axis. We finally transferred a nickelocene to the STM tip and used this molecular tip to probe the states of a second molecule. We consequently obtained a double spin excitation in our tunnel junction, with a significant increase of the conductance due to excitations.

Key words: STM, STS, IETS, magnetism, molecular electronics, spin excitation, single molecules, metallocene.